Universidade de São Paulo
Instituto de Física

Estados ligados de Majorana em junções de nanofios

Lucas Baldo Mesa Casa

Orientador: Prof. Dr. Luis Gregório Dias da Silva

Dissertação de mestrado apresentada ao Instituto de Física da Universidade de São Paulo, como requisito parcial para a obtenção do título de Mestre(a) em Ciências.

Banca Examinadora:
Prof(a). Dr(a). Luis Gregório Dias da Silva - Orientador (IFUSP)
Prof(a). Dr(a). Eric de Castro e Andrade (IFSC USP)
Prof(a). Dr(a). Edson Vernek (UFU)

São Paulo
2021

FICHA CATALOGRÁFICA
Preparada pelo Serviço de Biblioteca e Informação
do Instituto de Física da Universidade de São Paulo

Casa, Lucas Baldo Mesa

Estados ligados de Majorana em junções de nanofios / Majorana bound states in nanowire junctions São Paulo, 2021.

Dissertação (Mestrado) – Universidade de São Paulo, Instituto de Física, Depto. de Física dos Materiais e Mecânica

Orientador: Prof. Dr. Luis Gregório Dias da Silva

Área de Concentração: Física

Unitermos: 1. Supercondutividade; 2. Computação quântica; 3. Física da matéria condensada; 4. Majorana; 5. Nanofios

USP/IF/SBI-030/2021

University of São Paulo
Physics Institute

Majorana bound states in nanowire junctions

Lucas Baldo Mesa Casa

Supervisor: Prof. Dr. Luis Gregório Dias da Silva

Dissertation submitted to the Physics Institute of the University of São Paulo in partial fulfillment of the requirements for the degree of Master of Science.

Examining Committee:
Prof. Dr. Luis Gregório Dias da Silva - Supervisor (IFUSP)
Prof. Dr. Eric de Castro e Andrade (IFSC USP)
Prof. Dr. Edson Vernek (UFU)

São Paulo
2021

Acknowledgements

This work would not have been possible without the support from my family and friends. A special thanks to Julia for correcting my grammar.

I'd like to thank Prof. Luis Gregório Dias for not only taking me as his student during these two years, but also for introducing me to this exciting and lively field of topological materials. I extend this thanks to Bruna, João, Marcos, Raphael and Vinícius, for all the helpful discussions and conversations.

I'd also like to thank Prof. Annica Black-Schaffer for welcoming me into her research group during my exchange program to Uppsala University, as well as Jorge Cayao and Oladunjoye Awoga, for mentoring me during that period. This work would not have been possible without their help.

This study was financed in part by the Coordenação de Aperfeiçoamento de Pessoal de Nível Superior - Brasil (CAPES) - Finance Code 001, through a PROEX scholarship at the Master level.

Abstract

The possible realization of Majorana quasiparticles in condensed matter systems has motivated much research over the last decade, as it might pave the ground for topological quantum computing devices. In this work we review important concepts and results in the area, such as non-Abelian anyons, the Kitaev model and braiding. We then turn to a proposed implementation of Majorana fermions by reproducing literature results showing the emergence of p-wave superconductivity in nanowires with Rashba spin-orbit coupling and s-wave superconductivity in external magnetic fields. We study the spectrum for both infinite and finite nanowires and its evolution with respect to the field strength. We show that a topological phase transition is achieved and the emergence of Majorana Bound States (MBSs) in the topological phase. We investigate the distribution of these states across the nanowire and their non-locality.

We then reproduce results of NS and SNS junctions with Rashba nanowires, showing the leaking of the edge states into the normal regions. We also study the effects of the superconducting phase difference across the SNS junction, in particular how MBSs emerge at the interfaces only for a phase difference of π. We then calculate the Josephson current across the junction for different regimes and find a signature for the presence of MBSs. Finally, we propose a quantitative measurement for this signature through the derivative of the supercurrent for a phase difference of π.

Keywords— Majorana bound states, Topological superconductivity, Rashba spin-orbit coupling, nanowires, hybrid junctions

Resumo

A possível realização de quasipartículas de Majorana em sistemas de matéria condensada foi um tópico de intensa pesquisa na ultima década, já que estas quasipartículas podem abrir caminho para computação quântica topológica. Neste trabalho nós revisamos conceitos e resultados importantes da área, como anyons não-Abelianos, o modelo de Kitaev e *braiding*. Em seguida, nós focamos em uma proposta de implementação de férmions de Majorana e reproduzimos resultados da literatura mostrando a emergência de supercondutividade do tipo *p-wave* em nanofios com acoplamento spin-órbita do tipo Rashba e supercondutividade *s-wave* em campos magnéticos externos. Nós estudamos o espectro para nanofios tanto infinitos quanto finitos e a sua evolução com respeito à força do campo. Nós mostramos que uma transição de fase topológica é atingida e a emergência de Estados Ligados de Majorana (ELM) na fase topológica. Nós investigamos a distribuição desses estados ao longo do nanofio e a sua não-localidade.

Nós então reproduzimos resultados para junções NS e SNS em nanofios com acoplamento Rashba, mostrando o vazamento dos estados de borda para dentro das regiões normais. Nós também estudamos os efeitos da diferença de fase supercondutora através da junção SNS, em particular como ELMs emergem nas interfaces somente para uma diferença de fase de π. Nós então calculamos a corrente Josephson através da junção em diferentes regimes e encontramos uma assinatura para a presença dos ELMs. Por último, propomos uma medição quantitativa dessa assinatura através da derivada da supercorrente para uma diferença de fase de π.

Palavras-chave— estados ligados de Majorana, supercondutividade topológica, acoplamento spin-órbita do tipo Rashba, nanofios, junções híbridas

Contents

Chapter 1

Introduction

The last two decades have seen a significant rise in interest in exotic particles called Majorana fermions. Discovered in 1937, they are particular solutions to the Dirac equation which have the peculiarity of being their own anti-particles. For a long time considered only in the realm of particle physics, they have lately drawn attention in condensed matter physics, where they have been proposed to appear as zero energy states in unconventional superconductors. With a landmark paper, Kitaev, in 2001, constructed a simple model of a topological superconductor which could host these quasi-particle excitations at its edges. The idea sparked great interest as it was later argued that these states could be used for topologically protected quantum computation [1].

At the core of these ideas, a topological superconductor is one that undergoes phase transition without a symmetry breaking. The concept of topology, which in Mathematics refers to surface properties of non-local nature and that are preserved under smooth deformations, was appropriated in condensed matter physics to classify the order ruling these unconventional phases of materials. In this context, two systems are said to be topologically equivalent if their Hamiltonians can be continuously deformed into one another without any level crossings. This is specially useful in materials with a significant stability under smooth parameter change or adiabatic evolution. Materials are then given a topological classification and the non topologically trivial ones usually also present states located at its boundaries, called edge states. The above mentioned Kitaev model describes a one dimensional topological superconductor and its corresponding edge states are bound Majorana quasi-particles".

Besides the robustness due to the topological properties, these excitations have yet another peculiar property: the anionic non-abelian statistics. The anionic term means that its statistics differ from the Fermionic and Bosonic ones, and non-abelian means that consecutive exchanges involving a set of these particles can lead to different results when done in different orders. This property allows for encoding and manipulation of information and has motivated the proposals of topologically protected quantum computation using these quasi-particles.

In turn, this motivated a race for the implementation and detection of these exotic particles, which has become quite intense in this past decade after a landmark discovery of realistic materials that could host them [2, 3]. Serious efforts from many groups have led to the experimental finding of important theoretical predictions, such as the zero-bias peaks. But together with these findings, obstacles appeared along the way, as it has been proven to be difficult to differentiate between possible Majorana bound states and other trivial zero-energy excitations.

In this work we will study one of the main platforms being considered, the Rashba nanowire, as well as hybrid structures with these nanowires that were later proposed to expand the possibilities of signature detection. We will also discuss in more detail the properties of these bound Majorana states at the beginning.

1.1 Overview

Much of this work is built on top of an earlier version [4]. This final document is divided into three parts.

- We begin by introducing the reader to several key-concepts in the study of Majorana states in condensed matter. This is done in Chapter 2. We start by introducing the concept of Anyons. We then discuss how Majorana states can be obtained from the Dirac equation and how these states can be realized in the Kitaev model. We also show how this model presents a topological phase transition associated with the appearance of these exotic states. Finally, we combine the ideas from this chapter to show the anyonic and non-Abelian nature of Majorana Bound States.

- In Chapter 3, we make use of the concepts that have been introduced earlier to describe and study a more realistic proposal of platforms for Majorana Bound States, the Rashba nanowire. We begin by describing this system in the absence of superconductivity and study its bulk properties. We then make use of the Bogoliubov-de Gennes formalism to consider a superconducting system and see how the properties change. We show that in this new system a phase transition can happen. We then move to a tight-binding approach and show that this phase transition in also present in a finite system. We see that, in the topological regime, a zero energy state emerges satisfying the properties of a Majorana quasi-particle and we identify it as a Majorana Bound State.

- Finally, in Chapter 4 we study how hybrid structures with these nanowires behave. We first analyze the case of a junction with one normal region and one superconducting region (NS). Next we study a junction of a normal region in between two separate superconducting regions (SNS). In this system we also study the Josephson current that arises between the two superconductors and relate its profile to the presence or absence of topological states in the nanowire.

Chapter 2

Basic Concepts

Before appreciating the emergence of Majorana states in nanowires with Rashba spin-orbit coupling, it is instructive to first understand what are these elusive particles, which properties they possess and how these properties can be harnessed in topological quantum computation. We thus begin this chapter by studying *anyons*, the class of particles these Majorana states belong to due to their non-standard statistics. Next, we study in detail how Majorana states can be obtained from the Dirac equation of ordinary fermions. With these proper introductions to the subject we will then present the Kitaev model, a one dimensional system that presents some very interesting and relatively simple topological behaviour. We will verify a topological phase transition as well as the emergence of edge states, which, as we will see, shows a Majorana-like character. Finally, we will go a level of abstraction higher and show how moving these edge states around can make visible their non-abelian statistics.

2.1 Anyons

Arguably, one of the greatest discoveries of the 20th century has been that all known particles that compose the universe can be divided into two groups: that of bosons [5, 6, 7] and that of fermions [8, 9]. This classification is a consequence of the indistinguishability of similar particles and the symmetries they obey through the exchange between themselves. Moreover, the class a particle belongs to critically affects the behaviour of the system it forms. This is manifest not only in quantum statistics, where each class of particles has its associated distribution, but can also be traced as a root of many other intrinsically quantum phenomena, such as the Pauli exclusion principle and the Bose-Einstein condensation [1]. As fundamental and ubiquitous as it is, this classification was later found out not to be the full picture, at least when the assumptions are revised.

This dualistic view implicitly assumes our usual 3+1-dimensional space-time. In order to see this, we can first imagine two identical particles and notice how, in this space-time, interchanging them adiabatically (which means continuously and adiabatically exchanging all their quantum numbers) twice is equivalent to adiabatically moving one particle around another [1]: it is just a matter of going to the reference frame of one of the particles. This later movement is topologically equivalent to not moving any of the particles at all, that is, the trajectory of the orbiting particle can be continuously deformed into a single point without crossing another particle's world line. Because of this, the unitary transformation that represents this process should be equivalent to the identity operator. In turn, this constrains the representation of a single interchange to square to unity. Also, if we want the two mathematical states (the one before and the one after the exchange) to represent the same physical state, the single interchange must be represented as a phase. Therefore, the only possible one-dimensional representations for this transformation are the phases of ± 1: in three dimensions there can be only bosons and fermions.

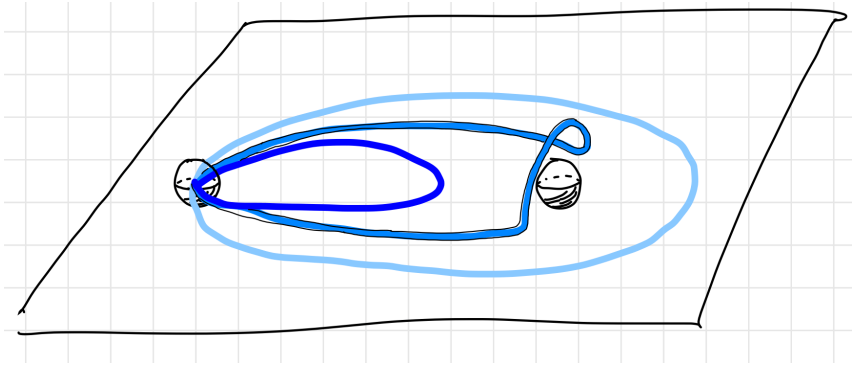

Figure 2.1: The trajectory of a particle around another is continuously deformable to the identity in three dimensions, but not in two Figure from Ref. [10].

If we instead consider lower-dimensional spaces, however, significant differences appear, as was first studied by Leinaas and Myrheim, in 1977, and by Wilczek, in 1982 [11, 12]. In 1+1-dimensional space-time there is no way to exchange two particles without crossing their world-lines, so the above view on statistics becomes meaningless on its own [1]. In 2+1 dimensions, on the other hand, we find that this exchange is still possible, but two exchanges are no longer continuously deformable into the identity without the crossing of world-lines [13, 14]. Because the representation of two interchanges is not equivalent to unity anymore, we find that one interchange alone is no longer limited to acting only as a sign, but is represented by a general phase

$$\psi(\mathbf{r_1}, \mathbf{r_2}) \to e^{i\theta}\psi(\mathbf{r_1}, \mathbf{r_2}), \tag{2.1}$$

where θ is a real number sometimes referred to as the *statistical angle*. This transformation reduces to the particular cases of bosons and fermions when $\theta = 0, \pi$ respectively, such that those classes still exist in two dimensions. Outside these special cases, however, we have particles that fit into neither group and so constitute new classes, which have been conveniently named *anyons* [15] and their associated statistical angle called *anyonic phase*.

Moreover, the set of closed trajectories for the two particle system can be classified by the number of windings a particle does around another. This winding number can, in principle, physically differentiate between the initial and final states after a double interchange of particles, so the two states need not represent the same physical state. When this happens, the transformation can no longer be represented by only a phase, but acts as a more general unitary operator on a manifold of states [16],

$$\psi_a(\mathbf{r_1}, \mathbf{r_2}) \to \sum_b U_{ab}\psi_b(\mathbf{r_1}, \mathbf{r_2}), \tag{2.2}$$

where each ψ_a represents a state with a specific winding number and U_{ab} are the matrix elements of a unitary matrix.

Given a set of N particles with such property, the operators representing the interchange of different pairs of particles need not to commute. This means that the order in which the particles are interchanged matters, and for this reason they have been named *non-Abelian anyons*. A short pedagogical introduction on the subject can be found in Ref. [17], where a physical mechanism involving the Aharonov-Bohm effect is used to exemplify the existence of such exotic particles in two-dimensional systems.

One important point must be made here. Although the mathematical existence of anyons, Abelian or not, can follow from the above arguments, it is not obvious if these ideas could ever model physical systems in the real world, which is 3+1-dimensional. A glimpse of hope appears, however, when we realize that nowadays we have the technology to build condensed

matter systems with micrometric or even nanometric thickness in specific directions, effectively freezing the spatial degrees of freedom along those axes for the electrons and quasi-particles inside them. With the spatial distribution along one axis frozen, the particles behave as if lying in a lower-dimensional space, hence allowing the above argument to work and anyons to emerge [16].

One of the first such platforms that were proposed to host anyons is the fractional quantum Hall effect (FQHE)[18], where 2-dimensional system of electrons in a magnetic field show plateaus of Hall conductance at fractional values of the conductance quanta. These fractional plateaus turned out to be very difficult to explain and the FQHE is still today an important and active research topic. Among the possible explanations developed, one was that some of the exotic states present in the system were anyons [19, 20]. This, however, has been far from the only practical systems in which experimentalists have been looking for anyons. Other examples range from optical systems, which recently yielded braiding statistics characteristic of non-Abelian anyons [21], to topological superconductors, which are believed to host even more exotic particles called Majorana Bound States [22, 23].

These Majorana particles are not only expected to behave as non-Abelian anyons, but also carry special properties due to the fact that they constitute what are called Majorana fermions. The main difference they present from ordinary (Dirac) fermions is that they are their own anti-particles. As such, they appear as zero-energy excitations inside the gap of those topological superconductors. These Majorana Bound States are the main star of this work and we now shift our focus to understand where this Majorana character they present comes from.

2.2 Majorana fermions

Derived in 1928, the Dirac equation describes how fermions, such as electrons, behave in 3D space [24]. It can be written as

$$\begin{aligned} i\hbar\frac{\partial}{\partial t}\mathbf{\Psi} &= \hat{H}_{Dirac}\mathbf{\Psi} \\ &= (c\boldsymbol{\alpha}\hat{\mathbf{p}} + \beta mc^2)\mathbf{\Psi}, \end{aligned} \tag{2.3}$$

where $\hat{H}_{Dirac}$ is the Dirac Hamiltonian and $\boldsymbol{\alpha}_i$ and β are 4×4 complex matrices that satisfy the relativistic energy equation

$$c^2\mathbf{p}^2 + m^2c^4 = (c\boldsymbol{\alpha}\mathbf{p} + \beta mc^2)^2. \tag{2.4}$$

Such matrices are not unique and each choice entails a spinor representation. The so-called Dirac representation is tied to the choice $\beta = \sigma_3 \otimes \mathbb{1}$, $\boldsymbol{\alpha} = \sigma_1 \otimes \boldsymbol{\sigma}$. From these, another set of matrices called the gamma matrices can be constructed:

$$\gamma = (\beta; \beta\boldsymbol{\alpha}). \tag{2.5}$$

We can then rewrite the Dirac Equation in real space as [23]

$$(i\hbar\gamma^\mu\partial_\mu - mc)\Psi = 0. \tag{2.6}$$

At this point we stress that the primitive matrices $\boldsymbol{\alpha}$ and β are both complex, at least in principle, and so are the gamma matrices. Likewise, the solutions to the Dirac Equation, that is, the 4-component spinors $\mathbf{\Psi}$, are complex fields, as it should be for charged particles [23]. The differential equation, then, intertwines the real and imaginary parts of the spinors such that we cannot split the equation into two independent ones. It was only in 1937 that it was discovered that a real set of gamma matrices that obeyed Eq. (2.4) actually existed, meaning that a separation of the real and imaginary parts of the equation was actually possible. The

person to do this was the Italian physicist Ettore Majorana [25] and the gamma matrices found by him were

$$\begin{aligned}\tilde{\gamma}^0 &= \sigma_2 \otimes \sigma_1 \\ \tilde{\gamma}^1 &= i\sigma_1 \otimes \mathbb{1} \\ \tilde{\gamma}^2 &= i\sigma_3 \otimes \mathbb{1} \\ \tilde{\gamma}^3 &= i\sigma_2 \otimes \sigma_2. \end{aligned} \tag{2.7}$$

Notice how they are all purely imaginary, so that the operators that act on the spinor fields in Eq. (2.6) are real. With this new set of matrices, Majorana proposed a novel particular solution to the Dirac Equation, where the spinor fields themselves are real, obeying the so-called reality condition [23]

$$\tilde{\boldsymbol{\Psi}} = \tilde{\boldsymbol{\Psi}}^*. \tag{2.8}$$

Particles that obey such solution came to be known as Majorana fermions, as opposed to the more general Dirac fermions. In order to understand what this condition means, we can go to another representation, say, the Dirac one, and see how the equation changes. Let U be the unitary transformation that leads from the Majorana representation to the Dirac one, that is, one such that

$$\gamma^\mu = U\tilde{\gamma}^\mu U^{-1}. \tag{2.9}$$

We see that $\tilde{\boldsymbol{\Psi}}$ transforms as $\tilde{\boldsymbol{\Psi}} \to U\tilde{\boldsymbol{\Psi}} = \boldsymbol{\Psi}$, while $\tilde{\boldsymbol{\Psi}}^*$ transforms as $\tilde{\boldsymbol{\Psi}}^* \to (U\tilde{\boldsymbol{\Psi}})^* = U^*\tilde{\boldsymbol{\Psi}}^* = \boldsymbol{\Psi}^*$. Thus, after multiplying both sides by U^{-1}, Eq. (2.8) gives way to

$$\begin{aligned}\boldsymbol{\Psi} &= U^{-1}U^*\boldsymbol{\Psi}^* \\ &= \mathcal{C}\boldsymbol{\Psi}^*, \end{aligned} \tag{2.10}$$

Here we just defined the operator $\mathcal{C}$, whose interpretation will become clear in a moment. The above equation is often referred to as the pseudo-reality condition since it is a more general version of the reality condition of Eq. (2.8). We now modify the Dirac equation in order to introduce a minimal coupling to the electromagnetic field,

$$[\gamma^\mu(i\hbar\partial_\mu + eA_\mu) - mc]\boldsymbol{\Psi} = 0. \tag{2.11}$$

From this we find that conjugation followed by the action of this new operator on the left yields

$$\begin{aligned} 0 &= [-\mathcal{C}\gamma^{\mu *}\mathcal{C}^{-1}(i\hbar\partial_\mu - eA_\mu) - mc]\mathcal{C}\boldsymbol{\Psi}^* \\ &= [-U^{-1}(U^*\gamma^{\mu *}U^T)U(i\hbar\partial_\mu - eA_\mu) - mc]\boldsymbol{\Psi}_c^* \\ &= [-U^{-1}\tilde{\gamma}^{\mu *}U(i\hbar\partial_\mu - eA_\mu) - mc]\boldsymbol{\Psi}_c^* \\ &= [U^{-1}\tilde{\gamma}^{\mu}U(i\hbar\partial_\mu - eA_\mu) - mc]\boldsymbol{\Psi}_c^* \\ &= [\gamma^{\mu}(i\hbar\partial_\mu - eA_\mu) - mc]\boldsymbol{\Psi}_c^*, \end{aligned} \tag{2.12}$$

where we defined the new spinor $\boldsymbol{\Psi}_c$ and made use of the fact that in the Majorana representation the gamma matrices are purely imaginary, so $\tilde{\gamma}^{\mu *} = \tilde{\gamma}^\mu$. What we have obtained is thus that the $\mathcal{C}$ operator generates a new equation of the Dirac kind, but with an opposite charge. Together with the complex conjugation operation, this operator can be identified with the charge conjugation symmetry. Indeed, Eq. (2.10) constrains a fermion to be its charge-conjugate counterpart, which in this context can be interpreted as its antiparticle [23]. Majorana fermions, thus, are fermions which are their own anti-particle.

One direct consequence of this is that they must be neutral, that is, chargeless particles. In the Majorana representation, as we have seen, this manifests itself through a purely real wavefunction. This, together with the ideas of basis change we just saw, suggests that a Dirac fermion can be thought of as a superposition of two (or more) different Majorana states with a phase between them. If we move to a second quantization formalism, this can be simply expressed by

$$\hat{c} = \frac{\hat{\gamma}_a + i\hat{\gamma}_b}{2}, \tag{2.13}$$

where $\hat{c}$ is the annihilation operator for a (non-relativistic) Dirac fermion, while $\hat{\gamma}_i$ represent different modes of Majorana fermions. With little rework the above expression leads back to our result on the Majorana particles being neutral: they can be expressed as a superposition of creation and annihilation operators of ordinary fermions,

$$\hat{\gamma}_a = \hat{c} + \hat{c}^\dagger, \tag{2.14}$$

such that the expected value for the number operator is zero. Similarly, one finds that $\hat{\gamma}_b = i(\hat{c}^\dagger - \hat{c})$, so that $[\hat{\gamma}_a, \hat{\gamma}_b] = 0$. However, it is straightforward to see that $\hat{\gamma}_a$ does not conserve charge, since it does not commute with the number operator: $[\hat{\gamma}_a, \hat{c}^\dagger\hat{c}] = \hat{c}^\dagger - \hat{c}$. One also finds that defining a Majorana number operator such as $\hat{n}_\gamma = \hat{\gamma}_i^\dagger\hat{\gamma}_i$ is useless, as this is just unity. This does not mean that there is no notion of counting associated with Majorana particles. Although we cannot count the number of Majorana particles, we can still count their parity. For that we have to take into account that there are two different types of Majorana operators. This motivates the definition of a parity operator as

$$\begin{aligned} \mathcal{P} &= i\hat{\gamma}_a\hat{\gamma}_b \\ &= 2\hat{c}^\dagger\hat{c} - 1, \end{aligned} \tag{2.15}$$

with eigenvalues ± 1. One can check that this operator counts whether there is an even or odd number of Majorana fermions in a given state. Since one also finds that $\hat{\gamma}_i^2 = \mathbb{1}$, that is how far one can go. Creating none or two Majoranas are equivalent processes.

Majorana's solution was initially put forward in the context of Particle Physics. However, in the recent decades, it has been proposed that it could appear in condensed matter systems, where such solutions are called Majorana Bound States, since these are usually confined to discontinuities or impurities in the system. In the context of condensed matter, Eq. (2.14) is usually interpreted as a superposition of an electron and a hole in a given material, while the reality condition for Majorana Bound States is written as

$$\hat{\gamma} = \hat{\gamma}^\dagger. \tag{2.16}$$

Notice how the operators associated with Majorana fermions are thus Hermitian, blurring the distinction between creation and annihilation operators. As an important remark, this condition is not in general satisfied by the whole time-dependant field. Described in terms of *stationary* solutions, the contributions from each energy eigenstate would evolve differently on each side of the above equation. The only way around this is if the Majorana fermions themselves are stationary solutions with zero energy. This way, both sides of the equation evolve trivially without picking up any phase and the Majorana condition can be satisfied for all times.

This is a crucial point. Even though any fermionic mode can be described in the Majorana representation, and perhaps even initialized in a state satisfying the Majorana condition, the particle and anti-particle contributions evolve differently with time, breaking the condition soon after it is satisfied. It is only for this specific zero energy case that we could, in principle, observe these Majorana fermions for discrete amounts of time. For this reason, realizations of Majorana fermions in condensed matter physics are also often referred to as Majorana Zero Modes.

Having all of this in mind, we are now ready to understand a landmark proposed implementation of Majorana states in condensed matter, the Kitaev toy model.

2.3 The Kitaev Model

In the turning of the century, A. Kitaev showed that the Majorana condition can be satisfied by many-body states, named Majorana Bound States (MBSs), in special types of superconductors [26]. As we will see, these states appear after a quantum phase transition of a topological character. At this transition the superconducting gap closes, dividing the parameter space into a trivial region and a topological one. We will also see how the spectrum of the latter nests MBSs below the superconducting gap. All these phenomena are described a relatively simple model put forward by Kitaev.

The Kitaev model describes a 1-dimensional lattice with a superconducting coupling of a special kind, named *p-wave* superconductivity. As proposed by Kitaev, the system presents only terms for an on-site energy and a hopping between next neighbors, as usual of tight-binding models, besides a non-charge-conserving coupling between two creation (or annihilation) operators of neighboring sites. The system's Hamiltonian reads

$$\hat{H}_{\text{Kitaev}} = -\mu \sum_{j=1}^{N} (\hat{c}_j^\dagger \hat{c}_j - \frac{1}{2}) + \sum_{j=1}^{N-1} \left[-t(\hat{c}_j^\dagger \hat{c}_{j+1} + \hat{c}_{j+1}^\dagger \hat{c}_j) + \Delta(\hat{c}_j \hat{c}_{j+1} + \hat{c}_{j+1}^\dagger \hat{c}_j^\dagger) \right], \tag{2.17}$$

where μ, t and Δ are all constants and $\hat{c}_j^\dagger$ creates a fermion at the j-th site. This Hamiltonian has two interesting peculiarities. First, notice how the spin index is suppressed. This is because the fermions this model describes (electrons in a 1D chain) are assumed to be spin-less. In practical terms, this can mean that the chain is spin-polarized (by applying a strong magnetic field, for example) such that the electron spins are all aligned and there is a great energy barrier separating the two different spin projections. This way, the spin degree of freedom can be disregarded in the low-energy regime.

The second peculiarity this model shows is that the superconducting term pairs electrons from different sites, in a manner similar to the hopping term. The specific way it does this (by pairing electrons in neighboring sites) is called a *p-wave* pairing because it obeys the same symmetries as the p-orbitals in a hydrogen atom.

In order to study this system it is convenient to make a Bogoliubov transformation. Inspired by the Majorana fermions we just discussed, let us combine same-site creation and annihilation operators in order to define

$$\begin{aligned} \hat{\gamma}_j^A &= \hat{c}_j + \hat{c}_j^\dagger \\ \hat{\gamma}_j^B &= -i(\hat{c}_j - \hat{c}_j^\dagger). \end{aligned} \tag{2.18}$$

This way, the anti-commutation relations for these new operators are given by

$$\{\hat{\gamma}_j^C, \hat{\gamma}_{j'}^{C'}\} = 2\delta_{jj'}\delta_{CC'}, \quad C, C' = A, B. \tag{2.19}$$

Moreover, these operators also obey the properties $(\hat{\gamma}_j^C)^2 = 1$ and $(\hat{\gamma}_j^C)^\dagger = \hat{\gamma}_j^C$. This last property should ring a bell by now: it is the Majorana condition! But before looking deeper into this, let us first write the Hamiltonian using these new operators. By defining $\omega_\pm = t \pm |\Delta|$, we get

$$\hat{H} = -\frac{i\mu}{2} \sum_{j=1}^{N} \hat{\gamma}_j^A \hat{\gamma}_j^B + \frac{i}{2} \sum_{j=1}^{N-1} \left[\omega_+ \hat{\gamma}_j^B \hat{\gamma}_{j+1}^A + \omega_- \hat{\gamma}_j^A \hat{\gamma}_{j+1}^B \right]. \tag{2.20}$$

The picture that we have now is that for every site we have two kinds of quasi-particles, $\hat{\gamma}_j^A$ and $\hat{\gamma}_j^B$, and that only quasi-particles of different kinds are coupled together. Moreover, we see that three different types of couplings arise. The first term is just the chemical potential term and it couples quasi-particles on the same site, as depicted in Fig. 2.2(a). The second

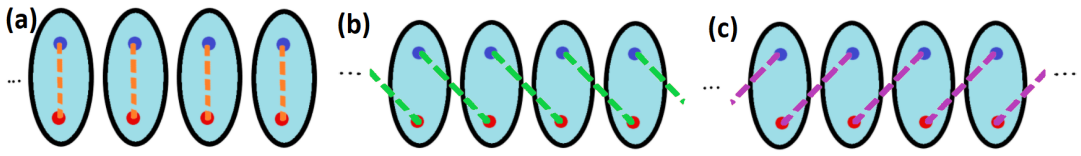

Figure 2.2: Representation of the three types of couplings present in the Kitaev model. The red dot represents Majorana operators of the type A, while the type B is represented by the dark blue dots. The cyan ellipses represent a fermionic site and the dashed line shows the coupling being represented.

term, shown in Fig. 2.2(b), couples quasi-particles of the type B to their A counterparts on its adjacent site to the right. Similarly, the last term describes couplings of A particles with their B neighbors to the right, as shown in Fig. 2.2(c). It is now instructive to study particular cases of this Hamiltonian.

Setting the chemical potential to a finite value while keeping $\omega_\pm$ equal to zero results in a rather trivial and boring example. The only coupling left is between same-site Majoranas, which is just the usual on-site energies of charged fermions on a background potential.

If we instead set the chemical potential μ to zero and consider a hopping amplitude t equal to the order parameter Δ (so that $\omega_+ = 2t$ and $\omega_- = 0$), we get that only the second term from Eq. (2.20) remains finite,

$$\hat{H} = \frac{i\omega_+}{2} \sum_{j=1}^{N-1} \hat{\gamma}_j^B \hat{\gamma}_{j+1}^A. \tag{2.21}$$

We then notice that, interestingly, the operators $\hat{\gamma}_1^A$ and $\hat{\gamma}_N^B$ do not appear in the Hamiltonian. Using the anti-commutation relations we can also check that $[\hat{H}, \hat{\gamma}_1^A] = [\hat{H}, \hat{\gamma}_N^B] = 0$. This necessarily means that given the many-body groundstate of this model, $|\Phi_0\rangle$, the states $\hat{\gamma}_1^A|\Phi_0\rangle$ and $\hat{\gamma}_N^B|\Phi_0\rangle$ are also eigenstates with the same energy, so that the groundstate of the system is degenerate.

The $\hat{\gamma}_j^C$ operators do not have a well defined charge associated to them because they are combinations of creations and annihilation operators. We can, however, define a fermionic operator

$$\hat{f} = \frac{1}{2}(\hat{\gamma}_1^A + i\hat{\gamma}_N^B) \tag{2.22}$$

that has the same expected value for the charge as an electron and still commutes with the Hamiltonian. This new operator can thus be regarded as a zero-energy fermionic excitation and it has the interesting property of being non-local, since it is located at both ends of the chain and is denominated a Majorana Bound State.

Although the zero-energy property of this state stems from the vanishing of certain parameters in the Hamiltonian, the existence of a non-local state located at both ends of the nanowire requires only that those parameters are kept within a finite range [26]. What then happens is that the wavefunction of this fermionic state decays exponentially into the bulk of the chain. Because of this, the tails of the peaks from both ends overlap in the middle of the chain and this gives the state a finite energy. As a consequence, this energy split decreases exponentially with the length of the chain [26], with its approximate value given by

$$E \approx \frac{2\tilde{\mu}\tilde{\Delta}}{\sqrt{\tilde{\mu} - (\tilde{\Delta}/2)^2}} e^{-\tilde{\Delta}L/2} |\sin(\sqrt{\tilde{\mu} - (\tilde{\Delta}/2)^2}L)| + \mathcal{O}(e^{-3\tilde{\Delta}L/2}). \tag{2.23}$$

A sketch of the proof for this expression is given in Appendix A.3. This result is achieved from the *Ansatz* that the wavefunctions for the edge states can be approximately described by evanescent waves, that is, plane waves with complex momenta. Also, it follows from this that the wavefunction not only decays exponentially, but it does so in an oscillating manner as well. We can conclude from this that for long enough chains the edge states can be regarded approximately as Majorana Zero Modes. As we have seen in the previous subsection, this means that the Majorana condition can be satisfied for a finite amount of time, the duration of it being increased as we consider longer chains. Long chains, on their turn, call for the study of the system through another lens, which will also enable us to see a phenomenon we have already mentioned: the topological phase transition of the Kitaev model.

2.3.1 Bulk properties and the topological phase transition

So far, we have considered only finite sized systems, where we can study the edge states. If we consider, on the other hand, a periodic chain or an infinite system, we can define a wavenumber for all single-particle excitations on the groundstate. The Kitaev Hamiltonian in this case can be written as [23]

$$\hat{H}_{\text{Bulk}} = \sum_k \xi_k(\hat{c}^\dagger\hat{c} - \frac{1}{2}) - \sum_k t\cos(ka) + \Delta\sum_k(\hat{c}_k^\dagger\hat{c}_{-k}^\dagger e^{ika} + \hat{c}_{-k}\hat{c}_k e^{-ika}), \tag{2.24}$$

where $\xi_k = -(\mu + 2t\cos(ka))$, a is the inter-site distance and k is the wavenumber. We can subsequently diagonalize this as a function of the wavenumber k, but in order to do so it is convenient to use the Bogoliubov-De Gennes (BdG) formalism. It consists of rewriting the Hamiltonian as a matrix H_{BdG}, which here is 2×2, sandwiched between two spinors, as

$$\hat{H}_{\text{Bulk}} = \frac{1}{2}\sum_k \begin{pmatrix}\hat{c}_k^\dagger, & \hat{c}_{-k}\end{pmatrix} H_{\text{BdG}} \begin{pmatrix}\hat{c}_k \\ \hat{c}_{-k}^\dagger\end{pmatrix}. \tag{2.25}$$

The matrix H_{BdG} is called the Bogoliubov-De Gennes Hamiltonian and the task of diagonalizing our initial Hamiltonian reduces to diagonalizing this simpler one. A more detailed description of the formalism is given in Appendix B.1. For the Kitaev model, the BdG Hamiltonian is given by [23]

$$H_{\text{BdG}} = \xi_k\sigma_z - 2\Delta\sin(ka)\sigma_y. \tag{2.26}$$

Through direct diagonalization, we finally find an expression for the energy eigenvalues,

$$E_{k,\pm} = \pm\sqrt{(\mu + 2t\cos(ka))^2 + 4\Delta^2\sin^2(ka)}. \tag{2.27}$$

Notice that for a finite order parameter Δ the energy goes to zero if and only if one of the two pair of conditions below are satisfied:

$$\mu = -2t \quad \text{and} \quad k = 0 \tag{2.28a}$$

or

$$\mu = 2t \quad \text{and} \quad k = \pm\pi/a. \tag{2.28b}$$

When the energy does go to zero, the upper and lower bands touch at the corresponding value of k. This is called a gap closing, since the gap between the two bands has indeed closed, and it signals a phase transition has happened in the superconducting system. In this particular system, it signals a topological phase transition. This means that when the chemical potential is in the intermediate region defined by $|\mu| < 2t$ the ground-state of the chain has one topology or configuration, while it changes to another one when the system leaves this parameter range. The

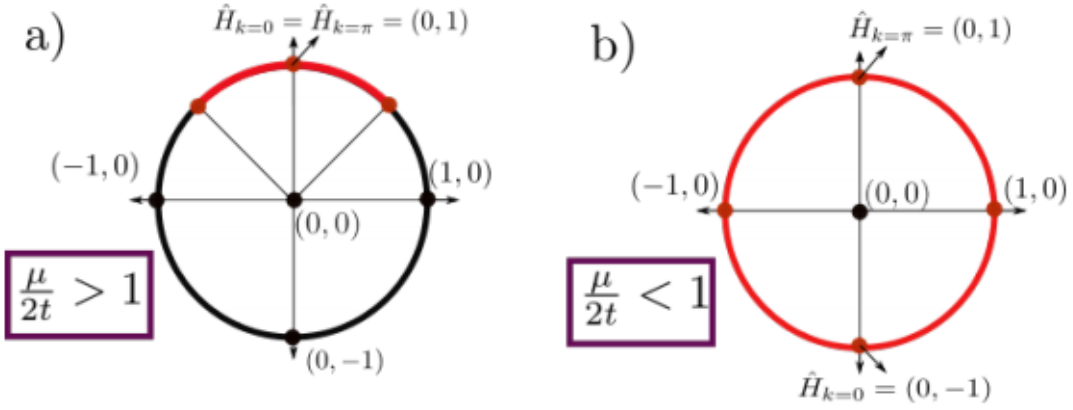

Figure 2.3: Trajectory of the Hamiltonians along the Bloch circle. Two distinct classes of paths can be seen. a) Trivial: trajectories can be deformed into a point. b) Non-trivial: Trajectories cannot be deformed into a point without closing the gap. Figure from Ref. [27]

two particular examples we saw for the finite chain case are instances of two different topological phases.

One way to better understand this phase transition is to picture the BdG Hamiltonian of Eq. (2.26) through a representation in a Bloch circle. This is done by associating each Pauli matrix with an axis in a Cartesian plane, using the coefficient of each matrix as a position along the corresponding axis and tracing out the trajectory followed by the Hamiltonian as the wavenumber covers the first Brillouin Zone. In addition, we normalize the parametrization, such that the trajectory is constrained inside a circle. It is easy to see, then, that the trajectory endpoints are the in the same postion. We also see, as depicted in Fig. 2.3, that there are essentially two classes of trajectories. When in the $|\mu| > 2t$ regime, the trajectory oscillates around the staring point as a pendulum, so that it passes through the $\big(1, \quad 0\big)$ point three times in total. More importantly, the trajectory for this class of Hamiltonians can be contracted to a single point without closing the gap, that is, without passing through the point $\big(0, \quad 0\big)$ where $H_{\text{BdG}} = 0$. Because of this, this parameter region is often referred to as the trivial one, and the phase it represents is called the trivial phase.

On the other hand, when we look to the $|\mu| < 2t$ parameter range, we find a very peculiar result. Exactly at the transition point the gap closes, as we just saw, so that the trajectory must be traversing the origin point of the Cartesian plane. At this point the parametrization cannot be normalized, but as soon as we traverse it we find that the trajectory now orbits around the origin completely. This means it can no longer be deformed into a point without closing the gap. We have entered a distinct class of Hamiltonians. In opposition to the trivial one, this parameter region is called the topological region and its phase the topological phase. As a final point to this discussion, let us connect these ideas with what we have seen for finite systems.

It turns out that, because of a so-called bulk-edge correspondence [28, 29], a topological change in the bulk of the system is manifest also by a change in the behaviour of localized edge states in the system. Because of this, the appearance of the Majorana Bound States we saw in the finite chain should be tied to one of the topological phases we just discussed. The phase where the Majoranas appear is then called the topological phase, while the other is named the trivial phase. Also, because in the particular, simplified case where we saw the emergence of the Majorana Bound State the system was inside the $|\mu| < 2t$ region (since we had $\mu = 0$), we can conclude that this is the topological phase of the system.

Now that we have a practical example of how Majorana fermions can appear, we can get a glimpse of how they can present the promised property of anyonic and non-Abelian statistics.

Let us take a look at one of the simplest ways this can be done.

2.4 MBSs as non-Abelian anyons

Arguably, one of the main interesting prospects of implementing Majorana fermions is the possibility of observing and making use of its non-Abelian statistics. As we have discussed on Sec.2.1, 1-dimensional systems such as the Kitaev model are rather boring in this respect, since statistics aren't well defined when you can't exchange two particles around (at least not without they crossing each other). What we've failed to consider so far, though, is an intermediate case between 1 and 2 dimensions, when several 1-dimensional wires are connected together. In this scenario, particle exchange becomes possible through a simple, but clever manipulation of the particle positions. A pedagogical explanation on the subject is found in Ref. [30].

This process goes as follows. First an intersection between an endpoint of a wire and a middle region of another wire is found, which we call a *T-junction*. Then two particles are selected to be exchanged and moved through the wires such that each is placed on a different side of the T-junction. Afterwards, one of the particles is moved to the empty ending of the junction, opening way for the other particle to take its place. Finally, the particle that had entered the empty ending takes the other particle's place.

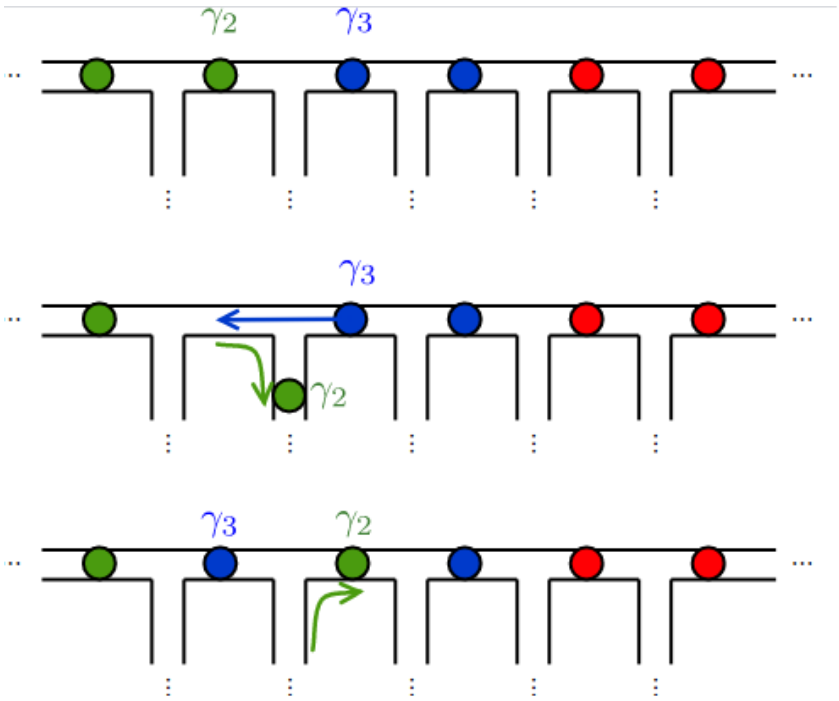

Figure 2.4: Two Majorana fermions exchange places in a network of 1-dimensional wires. Extracted from Ref. [30].

We need to point out that this of course requires a way to move the particles around. The practical way this can be done (if it even can) depends on the specific system the particles were implemented in. In the case of the Kitaev toy model this is possible by controllable, spatially varying parameters, such as the chemical potential. We haven't seen it yet, but the idea that the Majorana fermions appear only at the ends of the chain is not necessarily true for non-uniform parameters. What happens in this case is that different parts of the material can be in different phases and the MBSs appear at the borders between these different regions. When the parameters along the chain change adiabatically, the borders between the different topological phases can move, carrying the MBSs with them.

Another subtlety regarding this whole process is what the microscopic situation in the T-junction is. In the case such a junction has two terminals in the topological regime, with the remaining terminal in the trivial one, there emerges a domain wall right at the junction. Since domain walls are where the MBSs are located in these systems, one could naively expect that a lone MBS would arise. This would contradict the principle that MBSs always come in pairs, and so it cannot happen. What does happen at this point is that a *pair* of MBSs are created and hybridize, generating an ordinary fermion with finite energy. Further discussions on this subject can be found in Refs. [31, 32].

With these objections out of the way, we can attempt a heuristic analysis of the exchange process described above. This adiabatic transformation can be represented as a unitary matrix acting on the Hilbert space of the groundstate manifold of the system. The states of this manifold are characterized, as we have seen, by the presence of approximately zero-energy excitations, which can be counted using a parity operator. For concreteness, let's examine the case of three pairs of Majorana fermions, naming them from left to right along the chain as $\gamma_1, ..., \gamma_6$ and choosing γ_n and γ_m to take part on the exchange. We can then define the relevant parity operators as

$$\begin{aligned} \mathcal{P}_{12} &= i\gamma_1\gamma_2, \\ \mathcal{P}_{34} &= i\gamma_3\gamma_4, \\ \mathcal{P}_{56} &= i\gamma_5\gamma_6. \end{aligned} \tag{2.29}$$

In general, studying the adiabatic evolution of such a system would require knowing $\hat{H}(t)$ and working from there. However, in this case we can bypass this part and still find an expression for U_{nm}. Following the arguments of Ref. [30], we first note that the adiabatic exchange preserves the fermion parity of the system (since it does not create or destroy electrons), so that $[U_{nm}, P_{\text{tot}}] = 0$. Secondly, we make the reasonable assumption that U_{nm} should not depend on any Majorana fermions which do not take part on the exchange. This means U_{nm} can only depend on γ_n and γ_m and, since it must preserve fermion parity, the only way it can do it is through the product $\gamma_n\gamma_m$ or, equivalently, $\gamma_m\gamma_n$. The parity operators are already unitary, but they are not the most general unitary operators that can be constructed with this product. A more general expression is given by

$$\begin{aligned} U_{nm} &= \exp(\beta\gamma_n\gamma_m) \\ &= \cos(\beta) + \gamma_n\gamma_m \sin(\beta). \end{aligned} \tag{2.30}$$

By requiring that the two Majoranas must exchange places after the transformation,

$$U_{nm}\gamma_n U_{nm}^\dagger = \gamma_m, \tag{2.31}$$

$$U_{nm}\gamma_m U_{nm}^\dagger = \gamma_n, \tag{2.32}$$

one finds the constraint $\beta = \pm\pi/4$, which ultimately leads to

$$U_{nm} = \frac{1}{\sqrt{2}}(1 \pm \gamma_n\gamma_m). \tag{2.33}$$

The ambiguity on the sign is due to the possibility of exchanging the particles in a clockwise or counter-clockwise fashion. Already from this point one can see that the whole process cannot be represented by a single complex phase. If we now study how two subsequent exchanges are represented, we arrive at our desired result. Consider two exchanges with only one Majorana in common, U_{nm} and $U_{nm'}$, with $m \neq m'$. Let us consider they both to happen in the same direction of rotation so that both Us are defined with a positive sign. There are two ways these

exchanges can happen back to back. We can let $U_{nm'}$ happen first,

$$\begin{aligned} U_{nm}U_{nm'} &= \frac{1}{2}(1+\gamma_n\gamma_m)(1+\gamma_n\gamma_{m'}) \\ &= \frac{1}{2}(1+\gamma_n\gamma_m+\gamma_n\gamma_{m'}+\gamma_n\gamma_m\gamma_n\gamma_{m'}) \\ &= \frac{1}{2}(1+\gamma_n\gamma_m+\gamma_n\gamma_{m'}-\gamma_m\gamma_{m'}), \end{aligned} \tag{2.34}$$

or the other way around,

$$U_{nm'}U_{nm} = \frac{1}{2}(1+\gamma_n\gamma_{m'}+\gamma_n\gamma_m-\gamma_{m'}\gamma_m). \tag{2.35}$$

It is easy to see that these two orders are not equivalent. On the contrary, we have that

$$\begin{aligned} [U_{nm}, U_{nm'}] &= U_{nm}U_{nm'} - U_{nm'}U_{nm} \\ &= -\gamma_m\gamma_{m'}. \end{aligned} \tag{2.36}$$

We see then that these Majorana fermions must have a non-Abelian statistics and that this could, at least in principle, be verified using a network of 1-dimensional topological wires. This is the core property that attracted interest towards Majorana fermions and which led to several proposals on its use in topological quantum computation. This concludes the introductory and motivational part of this work.

We have seen how the Kitaev chain presents a topological phase transition and how its topological phase hosts Majorana Bound States localized at both ends of the chain. From this we could get a glimpse of the non-Abelian statistics of these bound states. As illustrating as this toy model is, it is still a theoretical tool. Implementing a similar system experimentally has been a challenging task in the last two decades. This is because the *p-wave* superconductivity required for it is extremely rare in nature. Fortunately, it has been shown that this kind of pairing can be artificially creating using simpler, more common ingredients. We will see how in the next chapter.

Chapter 3

Majoranas in nanowires with Rashba spin-orbit coupling

Put forward in 2001, the Kitaev model we have studied in the last chapter is an idealization. No *p-wave* superconductor has ever been found in nature. For years this had kept the idea of a topological superconductor hosting Majorana fermions just a dream. It was only a decade after that it was brought into the realm of the possible through a pair of publications by Oreg *et al.*[2] and Lutchyn *et al.*[3], when it was discovered that this unconventional type superconductivity could be artificially created in a material by combining different relatively common ingredients. One of these is the Rashba spin-orbit coupling, hence the platforms for this proposal becoming known as *Rashba nanowires*. Another property the nanowire should present is a relatively strong coupling to a Zeeman field. This coupling plays an important role, as the transition of the nanowire into a topological phase could be accomplished by driving up the external field. Lastly, the nanowire should also present ordinary s-wave superconductivity, and together these requirements led to a race towards finding the best material for the job [33].

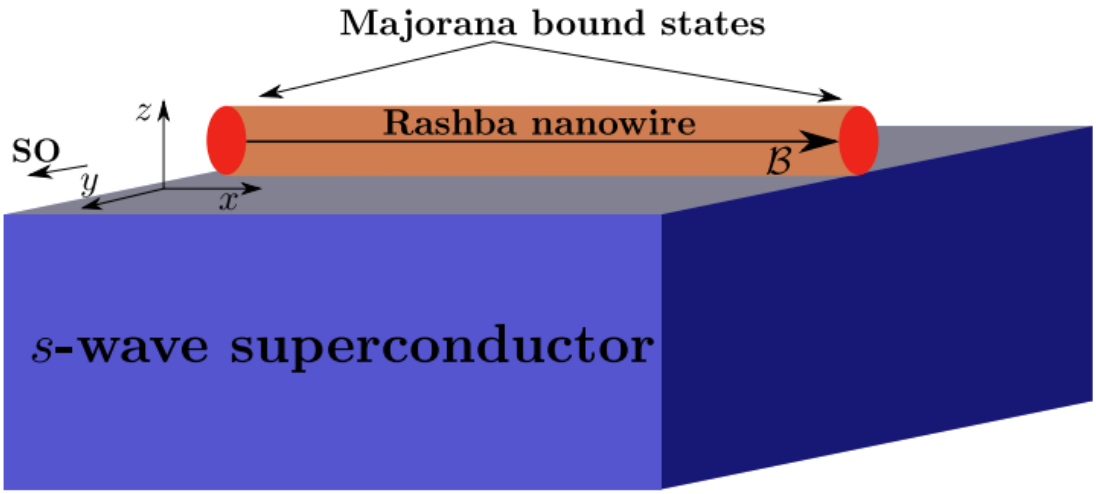

Figure 3.1: The basic setup for implementing Majorana fermions in Rashba nanowires. We see that the nanowire itself, which is not intrinsically superconducting, is placed on top of an ordinary superconductor, transferring superconductivity through the proximity effect. The spin-orbit axis of the nanowire and the axis of the Zeeman field (along the wire) are also indicated in the picture. Figure from Ref. [34].

As the requirement list is extensive, some compromises had to be made. The nanowires usually considered as platforms for Majorana fermions are not intrinsically superconducting. Instead, they are considered to acquire superconductivity by a proximity effect after being put next to an ordinary superconductor, such as an Al coating. We depict such a scenario in Fig. 3.1, where the Rashba nanowire is deposited on top of the superconductor. In this figure we can also see the Rashba coupling axis and the presence of the external Zeeman field along the nanowire. Other experimental variations include a partial or even a full shell surrounding the nanowire made of the superconducting material [35].

In the next sections we will ignore the details of this proximity effect and assume the superconducting pairing in the Hamiltonian of the nanowire itself. As we will see, this leads to a relatively simple model that can be treated analytically. First, however, we must introduce in mathematical detail the other ingredients and understand how they affect the system.

3.1 Rashba nanowires

A material with Rashba spin-orbit coupling in the presence of an external magnetic field is described by the Hamiltonian

$$\begin{aligned} H &= H_{\text{Kin}} + H_{\text{Rashba}} + H_{\text{Ext}} \\ &= (\frac{p^2}{2m^*} - \mu) + \frac{\alpha_R}{\hbar}(\boldsymbol{\sigma} \times \mathbf{p}) \cdot \hat{\boldsymbol{\alpha}}_R + B(\boldsymbol{\sigma} \cdot \hat{\mathbf{B}}). \end{aligned} \tag{3.1}$$

Here H_{Kin} is the Kinetic term, H_{Rashba} is the spin-orbit coupling of the Rashba type and H_{Ext} is the coupling to the external field, also called the Zeeman term, with p, μ and m^* being the momentum, the chemical potential and the effective mass of the electron. Also here, $\hat{\boldsymbol{\alpha}}_R$ and α_R are the spin-orbit coupling direction and strength, $\hat{\mathbf{B}}$ and B are the external field coupling direction and strength, and $\boldsymbol{\sigma}$ is a vector of Pauli matrices acting on the space of spin, all respectively. It is important to clarify that B is not the magnetic field magnitude $\mathcal{B}$, but is related to it by $B = g\mu_B\mathcal{B}/2$, where g is the material's g-factor and μ_B is Bohr's magneton.

We intend to discuss, however, nanowires made out of such materials. In these systems the dimensions of the device along all except one direction are sufficiently small for all movement along them to be suppressed. Such systems with the properties of the above Hamiltonian have been produced for a long time now [36] and they commonly consist of epitaxially grown InAs or InSb. For these 1D systems, the Hamiltonian can be simplified to be

$$H_{\text{NW}} = (\frac{p_x^2}{2m^*} - \mu) - \frac{\alpha_R}{\hbar}\sigma_y p_x + B\sigma_x, \tag{3.2}$$

where we have set the external field to be along the nanowire axis, $\hat{x}$ and the Rashba axis to be perpendicular to that, along the $\hat{z}$ direction. Placing the Rashba axis on any other direction not perpendicular to the nanowire would only amount to a re-scaling of the coupling strength, since the momentum along radial and azimuthal directions is being neglected. The consequences of an external field not fully perpendicular to the Rashba axis, on the other hand, is explored in the Appendix of Ref. [34].

If we now consider an eigenvalue equation with the Hamiltonian of Eq. (3.2), we arrive at a set of ordinary second order differential equations, whose solutions must be linear combinations of plane waves. We can further separate the spatial and spin degrees of freedom by making the *Ansatz* $\Phi_k(x) = \phi_k e^{ikx}$, such that eigenvalue problem simplifies to

$$\epsilon\phi_k = \left[\left(\frac{\hbar^2 k^2}{2m^*} - \mu\right) - \alpha_R k\sigma_y + B\sigma_x\right]\phi_k. \tag{3.3}$$

We can then diagonalize the matrix on the right hand side of the equation to find the dispersion relation for this system,

$$\epsilon_{\pm}(k) = \frac{\hbar^2 k^2}{2m^*} - \mu \pm \sqrt{B^2 + \alpha_R^2 k^2}, \tag{3.4}$$

as well as the spin part of the eigenstates,

$$\phi_{k,\pm} = \frac{1}{\sqrt{2}} \begin{pmatrix} \pm\gamma_k \\ 1 \end{pmatrix}, \tag{3.5}$$

where $\gamma_k = \frac{i\alpha_R k + B}{\sqrt{B^2+\alpha_R^2 k^2}}$ is a complex phase.

The dispersion above is shown as a function of the wavenumber k in Fig. 3.2. What we see is that we have two bands which are split by the term in the square root. When the Rashba and external field couplings are turned off, both bands become degenerate and parabolic, as in Fig. 3.2(a), and the separation between the bottom of the bands and the zero energy line is merely the chemical potential. The effect of turning on the field is of splitting the bands in energy without affecting their shape or position with respect to the wavenumber axis, which can be seen in Fig. 3.2(b). This happens because the external field is the only term that couples to spin, since we have not considered the spin-orbit coupling yet. This means that the spin projection along the field axis is a good quantum number and the electrons can be either parallel or anti-parallel to it. By then choosing an appropriate basis and taking a look at the eigenstates one can identify each band to a spin projection. In this panel we choose the $x-axis$, such that the band in red represents electrons with spin parallel to the field, while the blue one represents electrons anti-parallel to the field. This can also be seen in the expression for the eigenstates of Eq. 3.5, where the limit of no Rashba coupling leads to real states of symmetric and anti-symmetric nature.

If we turn the field off again and make the Rashba coupling finite, what we get are the bands of Fig. 3.2(c), where the parabolas are split in the wavenumber axis instead of energy. To understand why this is so, we can turn again towards the spin projection. Since we still have that only one term couples to spin, the spin projection is still a good quantum number. This time, however, the appropriate spin basis that diagonalizes the Hamiltonian is along the Rashba axis ($y-axis$) instead of the field one, as is done in the plot, with red and blue still representing parallel and anti-parallel spins. This can be seen through the eigenstates as they become eigenstates of σ_y for this case. We see, also, that the two bands have their corresponding minima at $\pm k_{\mathrm{SO}} = \pm m\alpha_R/\hbar^2$. What this all means is that the spin has been tied to the momentum, such that electrons going in one direction minimize their energy with a certain spin projection and vice-versa. The energy at the bottom of the bands is now given not only by the chemical potential, but is also affected by the above described effect, such that its value is $E(k_{\mathrm{SO}}) = -(\mu + E_{\mathrm{SO}})$, where $E_{\mathrm{SO}} = m^*\alpha_R^2/2\hbar^2$. Lastly, we can see that the two bands cross only at $k = 0$, where the energy equals the chemical potential.

Next, we can analyze what happens when both terms are present. As we can see from Fig. 3.2(d), the crossing at $k = 0$ we just mentioned becomes an anti-crossing as the two bands hybridize. This happens because we now have two different Pauli matrices entering the Hamiltonian with different dependencies on the wavenumber. In more detail, since the Rashba coupling is linear in momentum while the Zeeman coupling is momentum independent, there is no longer one single spin basis which diagonalizes the energy for all wavenumber values. Instead, for each value of k one can find an appropriate spin basis. As a visualization aid, we color each point in the plot according to the projection of the eigenstate on a σ_x basis, such that red and blue show that on those points that basis works adequately, while shades of purple show regions where the energy eigenstates are superpositions of the σ_x spin eigenstates. From Eq. (3.5) we see this happening as γ_k takes any value of a complex phase, varying the state between σ_x and

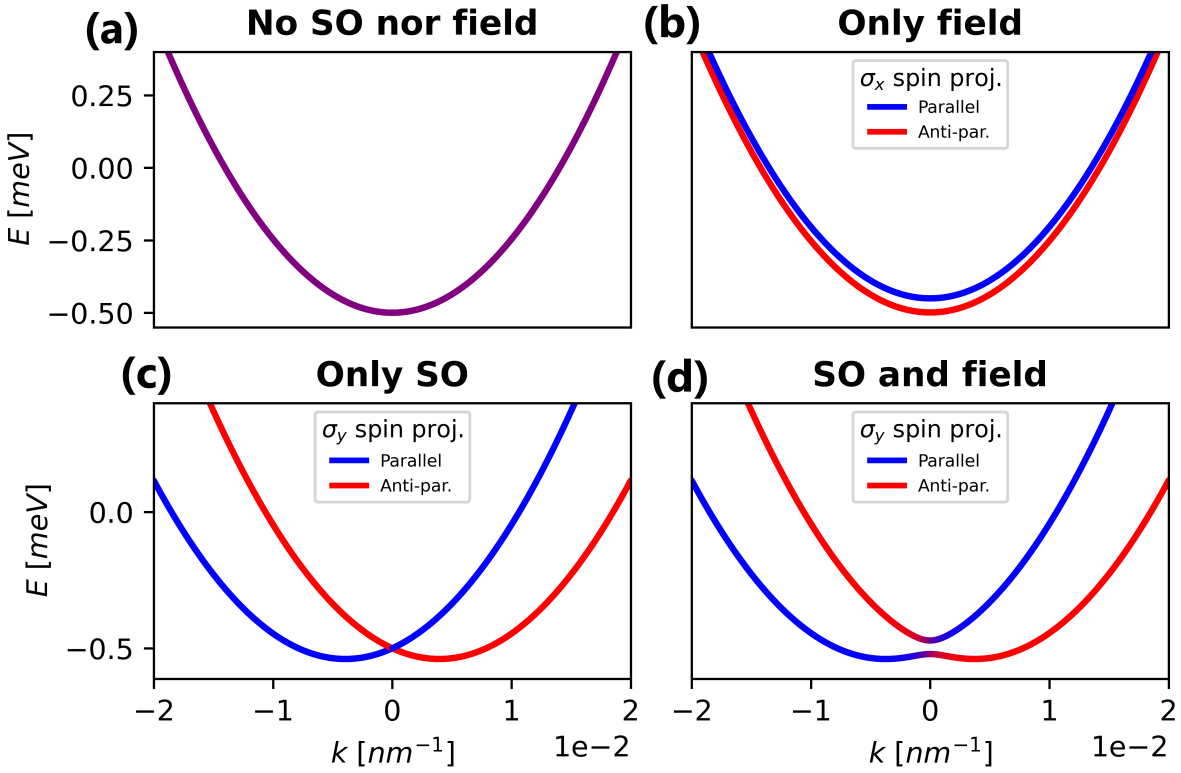

Figure 3.2: The dispersion relation for a Rashba nanowires in external fields. Panel (a) represents the case of no spin-orbit coupling and no external field. In (b) and (c) we then present a finite field and spin-orbit coupling, respectively. We observe that while the field splits the parabolas vertically, the spin-orbit coupling does so horizontally. In both these cases we can still assign a spin to each band, which we represent by different colors. Note that the axis on which we project the spin differs on each case and is specified on each panel. Finally, in panel (d) we combine the two ingredients and observe that the two bands hybridize, tying spin and momentum together. The parameters used were $\mu = 0.5meV$, $B = 0.025$ and $\alpha = 20nm.meV$.

σ_y eigenstates. As another consequence of the hybridization, we see that the lower band has two minima, while the upper one has only one.

Another important feature present in this case is the energy separation between the two bands. As in the Zeeman-only case, they do not touch each other and by tuning the parameters one can increase the gap between them. A feasible way to do so, in this case, is to control the ratio between chemical potential and the Zeeman energy. We see that when the later is smaller, as shown in Fig. 3.3(a), the upper band dips below zero energy, meaning that it will have occupied states even at zero temperature. What we have, then, is that we can find electrons with all four possible combinations of movement direction and spin projection at the Fermi energy. This is because there are four Fermi points in this regime, two in the upper band and two in the lower band. As we increase the Zeeman energy, we find that the dip eventually recedes, as shown in Fig. 3.3(b). This happens when $B > \mu$ and it leaves the upper band completely empty, so that there are only two Fermi points in the system. The system then acquires a fixed relationship between spin and momentum at the Fermi level, which is dictated by the lower band. This phenomenon is sometimes called spin-momentum locking and the physical state it is related to is named a *helical state*. An important note must be made here that the axis on which the spin is projected in order to observe this locking is not the direction of movement, usually associated with helicity, but the spin axis of the Rashba coupling, associated with σ_y. It is, in a sense, an

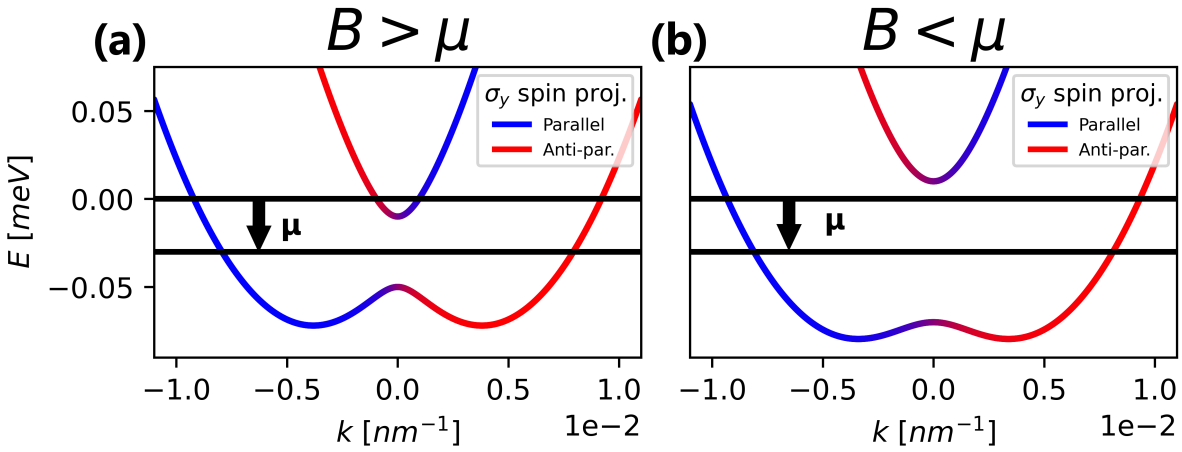

Figure 3.3: The competition between the chemical potential and an external field on the spectrum of a Rashba nanowire. We see on panel (a) that when the chemical potential is smaller than the Zeeman energy the upper band crosses the Fermi energy and thus is partially occupied. When the Zeeman energy becomes dominant, as shown in panel (b), the upper band never crosses the Fermi energy and is not occupied. The colors represent the Spin projection along the $y-axis$. This is referred to as a *Helical* regime [2], in the sense that the spin-projection is locked to momentum. The parameters used were $\mu = 0.03meV$ and $\alpha = 20nm.meV$, with $B = 0.0006meV$ for (a) and $B = 0.0012meV$ for (b).

abuse of notation to call these states helical.

As an interesting consequence of this regime transition, the system now occupies only one band. For this reason, it is sometimes said to be *spin polarized*. The helicity and spin-polarization are essential properties for both the topological nanowires and the more complex hybrid systems we will construct starting from the Rashba nanowire. Because of these properties shown by the non-superconducting Rashba nanowire, its eigenstates as described in Eq. (3.5) form what will refer to as the *Helical basis*. As an abuse of language, this is used even when outside of the Helical regime. As we will see, the helical basis is extremely useful when studying these systems. Now that we have gathered some understanding of how these properties arise, let us add the next ingredient into the mix, conventional s-wave superconductivity.

3.2 Superconducting Rashba nanowires: bulk properties

The ingredients required to build a topological superconductor out of nanowires with Rashba spin-orbit coupling are many. This not only complicates the theoretical study of this system, but makes the task of finding suitable materials for practical implementation an extremely difficult challenge. This is because the different materials we can make nanowires out of have many properties fixed. The strength of the spin-orbit coupling α_R and the Zeeman coupling g, for example, are material-dependent and finding a material that has high values for both quantities is quite hard. If we then were to restrict ourselves to intrinsically superconducting materials, we would be bound to fail.

Fortunately, intrinsic superconductivity is not the only way for a material to present Cooper pairing in its effective Hamiltonian. It has been known for a very long time [37, 38] that placing a superconductor close to an ordinary conductor allows for the tunneling of Cooper pairs from the former into the later. This is called proximity-induced superconductivity and many proposed

implementations of the Kitaev model make use of it [2, 3]. In our case, the proximity effect would allow one to generate superconductivity in a Rashba nanowire by placing it on top of an ordinary superconductor, as depicted in Fig. 3.1. For a more in-depth discussion on the proximity-effect in Rashba nanowires we direct the reader to Refs. [39, 40, 41]. Although, as discussed in these references, non-intrinsic superconductivity would be weaker and could generate side effects, we shall in this work neglect this fact and insert the usual pairing "by hand" on the Hamiltonian for the sole reason of making the problem more tractable mathematically.

So we can treat this problem, it is also convenient to introduce the so-called *Bogoliubov-De Gennes* formalism. It consists in doubling the degrees of freedom of the ordinary second-quantized spinor, such that both creation and annihilation operators are present. This allows for combinations of alike operators in the Hamiltonian, as is required by superconductivity. The spinors $\hat{\Psi}^\dagger$ then sandwich a 4×4 Hermitian matrix, denominated the BdG Hamiltonian, which satisfies particle-hole symmetry. This procedure is explained in more detail in Sec. B.1 and leads to the final Hamiltonian of the system having the form

$$\mathcal{H} = \frac{1}{2} \sum_k \hat{\Psi}^\dagger(k) H_{\text{BdG}}(k) \hat{\Psi}(k), \tag{3.6}$$

where the coefficient $1/2$ accounts for the double counting caused by doubling the degrees of freedom. In order to apply this to our case, we must first find how the different terms of the non-superconducting Rashba nanowire are expressed as BdG Hamiltonians. We begin by choosing a spinor basis, such as

$$\hat{\Psi}^\dagger(k) = \left(\hat{c}^\dagger_{k\uparrow}, \quad \hat{c}^\dagger_{k\downarrow}, \quad \hat{c}_{-k\uparrow}, \quad \hat{c}_{-k\downarrow} \right), \tag{3.7}$$

and then rewriting the Hamiltonian H_{NW} from Eq. (3.2) as a function of the wavenumber of such spinors,

$$H_{\text{NW}}\ (k) = \frac{\hbar^2 k^2}{2m^*} - \mu - \alpha_R k \sigma_y + B\sigma_x. \tag{3.8}$$

From the above matrix we can construct the second-quantized Hamiltonian for the system and subsequently rearrange part of the operators in order to make evident the particle-hole symmetry of the system. Following the procedures described in the appendix, we can then write down the corresponding BdG matrix, which must be

$$H^{(0)}_{\text{BdG}}(k) = \begin{pmatrix} H_{\text{NW}}(k) & 0 \\ 0 & -H^*_{\text{NW}}(-k) \end{pmatrix}. \tag{3.9}$$

Another way to derive such a result would be by first finding out the particle-hole symmetry operator associated with the spinor basis of Eq. (3.7). It is easy to see that the spin degree of freedom must be left untouched, while the particle-hole sector is swapped through σ_x, the creation and annihilation operators interchanged through complex conjugation and the momenta through a change of sign. The symmetry must then be accomplished through the operator $P = (\tau_x \otimes \sigma_0)\mathcal{S}_k\mathcal{K}$, where τ acts on particle-hole space, σ acts on spin, $\mathcal{S}_k$ changes sign of k and $\mathcal{K}$ acts as complex conjugation. As a sanity check, it is easy to see that applying this symmetry on the BdG Hamiltonian above leads to

$$P H_{\text{BdG}} P^{-1} = -H_{\text{BdG}}. \tag{3.10}$$

This means that our expression for the particle-hole symmetry is indeed connecting energy eigenstates with opposite eigenvalues, as it should. Now we proceed to open up the expression to find a more explicit form for the BdG Hamiltonian.

With some simple calculation one finds that the spin-orbit term get a sign from both complex conjugation and the swapping of the wavenumber sign, such that they cancel each other. The

kinetic and Zeeman terms, on the other hand, are left untouched by these operations. The explicit minus sign of the hole block in Eq. (3.9) then makes the whole Hamiltonian behave as τ_z in particle-hole space, such that $H^{(0)}_{\mathrm{BdG}}(k) = \tau_z \otimes H_{\mathrm{NW}}(k)$

Finally, we can add s-wave superconductivity to our system. Conventional s-wave pairing is described by operators of the type

$$\hat{H}_{\text{s-wave}}(k) = \Delta(\hat{c}^\dagger_{k\uparrow}\hat{c}^\dagger_{-k\downarrow} + \hat{c}_{-k\downarrow}\hat{c}_{k\uparrow}). \tag{3.11}$$

In the spinor basis we are currently using, the BdG Hamiltonian that represents this pairing $H^{(\text{s-wave})}_{\mathrm{BdG}} = \Delta\tau_y \otimes \sigma_y$. By combining this to the BdG Hamiltonian of the non-superconducting Rashba nanowire, we find the full BdG Hamiltonian of the system.

$$H_{\mathrm{BdG}}(k) = \left(\frac{\hbar^2 k^2}{2m^*} - \mu\right)(\tau_z \otimes \sigma_0) - \alpha_R k(\tau_z \otimes \sigma_y) + B(\tau_z \otimes \sigma_x) + \Delta(\tau_y \otimes \sigma_y). \tag{3.12}$$

From this, one can obtain the energy spectrum of the system by diagonalizing the above matrix. By defining the free electron energy $\xi_k = \hbar^2 k^2/2m^* - \mu$ for shorthand notation, we find that the energy eigenvalues are given by

$$E_{\pm,\pm}(k) = \pm\left[\xi_k^2 + \alpha_R^2 k^2 + B^2 + \Delta^2 \pm 2\sqrt{B^2\Delta^2 + (B^2 + \alpha_R^2 k^2)\xi_k^2}\right]^{1/2}. \tag{3.13}$$

As a first comment on the spectrum, we point out that we see four non-degenerate bands on the general case, as should be expected due to the doubling of degrees of freedom required by the BdG formalism. We also would like to point out how the spectrum is symmetric around zero. This is a consequence of the particle-hole symmetry we enforced on the system, and the states with opposite energies are connected to each other through this symmetry. We also salient that the expression above is a bit more complicated than the dispersion we found for the non-superconducting case, but we can begin to understand it by again looking at limiting cases.

Firstly, we notice how when all ingredients but the kinetic term are turned off the dispersion becomes parabolic, as one would expect. If we plot it, as we do in Fig. 3.4(a), we find that the two upper bands are degenerate between themselves (as are the bottom ones), and that for positive values of the chemical potential the two groups of bands cross. From the crossing we see that the lower bands are not fully occupied and the upper ones are not completely empty even at zero temperature. The degeneracy, on its turn is due to the lack of terms that affect the spin degree of freedom. This is the same we saw in the non-superconducting case, and we can follow the same steps we did there to find more similarities.

By turning on the spin-orbit coupling, which we do in Fig. 3.4(b), we observe again the sideways shift on the parabolic bands. This time, though, the particle-hole symmetry imposes several band crossings that were not there in the other case, as pointed out in the plot. A similar thing would happen if we instead considered a finite Zeeman coupling, but with the split being vertical instead of horizontal. Also, because the energy minimum of some bands decreases in both cases, it is possible that a finite value of the couplings causes the particle and hole bands to cross even if the chemical potential was not high enough to cause the crossing. Moving on, we can then consider what happens if both the spin-orbit and the Zeeman terms are finite. As we can see in Fig. 3.4(c), the new crossings between particle and hole bands are still present, but the hybridization between bands of the same type make them anti-cross, just as in the non-superconducting case. In terms of the expression in Eq. (3.13), we see that the presence of any or both these ingredients causes the square root term to be non-vanishing, hence breaking the spin degeneracy.

Finally, some drastic changes happen when we consider a finite order parameter Δ. So far, we saw how a positive chemical potential (or a negative one with sufficiently strong other

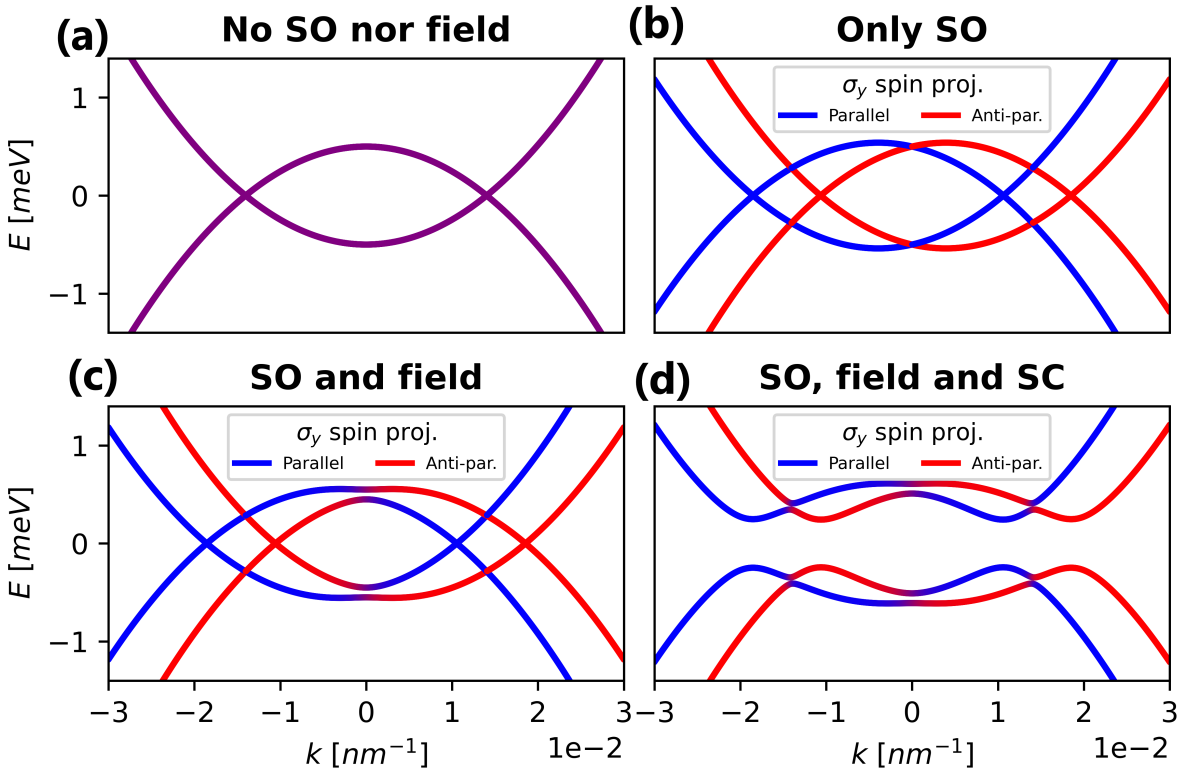

Figure 3.4: The dispersion relation for nanowires in the BdG formalism. In panel (a) we see mirroring parabolas representing the electron and hole bands. In panel (b) we see that the spin-orbit effect shifts the bands of electrons and holes of equal to the same side and many different band crossings appear. In panel (c) we can see that an external field hybridizes some of those crossings, but not all. Finally, in panel (d) we can see how the presence of superconductivity hybridizes the remaining crossings, so that we now have four non-intersecting bands and a gap opens around the Fermi energy. The parameters used were $\mu = 0.5meV$, $B = 0.05Bc$, $\alpha = 20nm.meV$ and $\Delta = 0.25meV$.

couplings) leads to a gapless spectrum, which in a particle-hole symmetric system requires the presence of band crossings at zero energy. Superconductivity puts that to an end by hybridizing particle and hole bans together. Mathematically, this happens because we are coupling together operators of the same type (creation or annihilation ones). The consequences of this can easily be seen in Fig. 3.4(d), where there is an energy interval around zero in which no possible states exist. This is a common result for superconductors and the size of the energy gap is usually tied to the formation of Cooper pairs.

Having these basic properties of the system in mind, we can start turning ourselves towards a deeper analysis and remember what was our goal with this system. As was mentioned above, the superconducting Rashba nanowire is expected to develop a different quantum phase, of a topological nature, under certain circumstances. It is in this phase we expect to find MBSs, but we must first discover how to get to this phase by finding the correct range of parameters. We must now find signs of phase transition happening as we tune the different couplings. With this objective, it is relevant to notice how the superconducting gap discussed above still exists when the other terms are neglected.

3.3 Superconducting Rashba nanowires: phase transition

A gap closing is, in other words, the zeroing of the energy eigenvalues for a set of parameters and wavenumber. Since the dispersion relation of this system is symmetric by a sign inversion of the wavenumber, if we want for the gap to close at only one point at a time, we must consider the wavenumber to be zero. Inserting this constraint into Eq. (3.4) and simplifying a bit we find that

$$E_{\pm}(0) = |B \pm \sqrt{\Delta^2 + \mu^2}|. \tag{3.14}$$

It is clear now that there are two points at which the gap closes at zero momentum. They both correspond to a Zeeman energy magnitude of

$$B_c = \sqrt{\Delta^2 + \mu^2}, \tag{3.15}$$

with each case representing a field in opposite direction. Because it is precisely at this Zeeman energy that the gap closes, this field value is called the *critical field* and it marks a transition in the behaviour of the system, as we will see. We can now see how this gap closing happens as we drive the field from zero up to a value higher than the critical one.

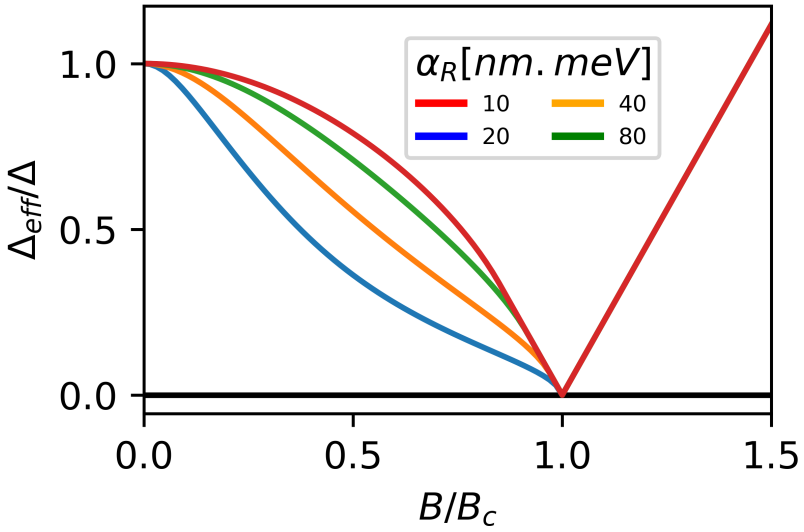

Figure 3.5: The effective gap in the dispersion relation of a superconducting Rashba nanowire as a function of the Zeeman energy. We see that this gap monotonically decreases to zero as the field approaches the critical value. At this critical point the gap is said to have closed and it signals a phase transition. As the field increases again, the gap reopens and increases linearly. The different curves represent different values of the spin-orbit coupling and we observe that they all behave the same for fields higher than the critical one.

This is depicted in Fig. 3.5, where we plot the energy of the lowest of the upper bands as a function of the field. We see that the energy does indeed go to zero at the critical field, while it is finite everywhere else. This phenomenon is an evidence that a phase transition in happening in the system. In order to discuss this further, let us take a look at these ideas from a different perspective by rewriting the BdG Hamiltonian in a different basis.

As we have seen in Chapter 3, the helical basis constitutes a more natural way of describing this system. In order to get back to it, we define a new spinor basis,

$$\hat{\Phi}^{\dagger}(k) = \left(\hat{\phi}^{\dagger}_{k+}, \quad \hat{\phi}^{\dagger}_{k-}, \quad \hat{\phi}_{-k+}, \quad \hat{\phi}_{-k-}\right), \tag{3.16}$$

where $\hat{\phi}^\dagger_{k\pm}$ ($\hat{\phi}_{k\pm}$) creates (annihilates) an electron at the $\phi_\pm(k)$ state described by the Helical basis of Eq. (3.5). Because those states are related to the ordinary operators $\hat{c}^\dagger_{k\sigma}$ ($\hat{c}_{k\sigma}$) through a unitary transformation, the newly defined spinor is also related to the spinor of Eq. (3.7) through a unitary transformation. In this new basis, the BdG Hamiltonian of the superconducting Rashba nanowire becomes

$$H^{(\text{Helical})}_{\text{BdG}} = \begin{pmatrix} \epsilon_+(k) & 0 & \Delta_{++}(k) & \Delta_{+-}(k) \\ 0 & \epsilon_-(k) & -\Delta_{+-}(k) & \Delta_{--}(k) \\ \Delta^\dagger_{++}(k) & -\Delta^\dagger_{+-}(k) & -\epsilon_+(-k) & 0 \\ \Delta^\dagger_{+-}(k) & \Delta^\dagger_{--}(k) & 0 & -\epsilon_-(-k) \end{pmatrix}, \tag{3.17}$$

where $\epsilon_\pm(k)$ are the energies of the non-superconducting case found in Eq. (3.4). We have also just defined the quantities

$$\Delta_{--,++}(k) = \frac{\pm i\alpha_R k\Delta}{\sqrt{B^2 + (\alpha_R k)^2}} \quad \text{and} \quad \Delta_{+-}(k) = \frac{B\Delta}{\sqrt{B^2 + (\alpha_R k)^2}}. \tag{3.18}$$

By doing this, we diagonalize the particle and hole blocks of the Hamiltonian straight away, leaving only the superconducting terms outside the main diagonal. These, however, become more complex, as we see appear two different types of couplings.

One of them, Δ_{+-}, couples particles and holes of opposite momenta from different bands. This is analogous to the s-wave pairing we saw in the first basis, with the detail that now the bands being paired together are not of free electrons of opposite spins, but of helical states with different helicity. For this reason, it's called an *inter-band* pairing. Its strength is proportional to the order parameter Δ that controlled the s-wave pairing, but is also scaled by the Zeeman and spin-orbit terms. The Zeeman dependence is rather weak for large fields and the spin-orbit coupling suppresses superconductivity in the opposite regime. With the exception of these details, not much new behaviour is found in this term.

The Δ_{--} and Δ_{++} pairings, on the other hand, show some very unique physics. One can see from the BdG matrix that these terms are coupling together electrons and holes of the same band. This is dubbed *intra-band* superconductivity and is drastically different from usual superconductivity. Moreover, these pairings are not only proportional to the order parameter, but are also approximately linear in the wavenumber for large enough fields. Since its general form is odd in k, it possesses the same symmetries as of p atomic orbitals. For this reason, this kind of coupling is termed p-wave superconductivity. As one can recall, this is the same type of paring that appears in the Hamiltonian of the Kitaev toy model. Not only that, but it is a crucial factor for the emergence of the topological phase and the Majorana states in that system.

Although we do not show here, the Kitaev model can be derived from our Rashba system through perturbation theory for high fields in the small momentum regime. Outside this scope, however, We have many extra terms in our Rashba Hamiltonian that obscure and shuffle the spectrum. Part of it grants our system a different and perhaps even more rich behaviour, and cannot be thrown out. Another part, as will see, is not essential and can be made negligible by tuning the system parameters correctly.

In order to see this we must take a look at how the bands evolve as we tune the field. The reason we still insist in using this parameter as control is that it is more easily controllable in experiments and we have already found a simple expression of the critical point associated with it, B_c. In Fig. 3.6 we plot the dispersion relation for fixed parameters and increasing values of the field. In Fig. 3.6(a) we see how the superconducting system behaves in the absence of a field, with a superconducting gap present. We again see the horizontal separation of the bands due to spin-orbit coupling, such that each band can be tied to a spin projection. If we increase the field to a finite but small value, as we do in Fig. 3.6(b) we find that the band crossings hybridize due to spin not being a good quantum number anymore. All this has been seen and discussed already, but a new phenomena appears when we tune the field up to the critical value, B_c.

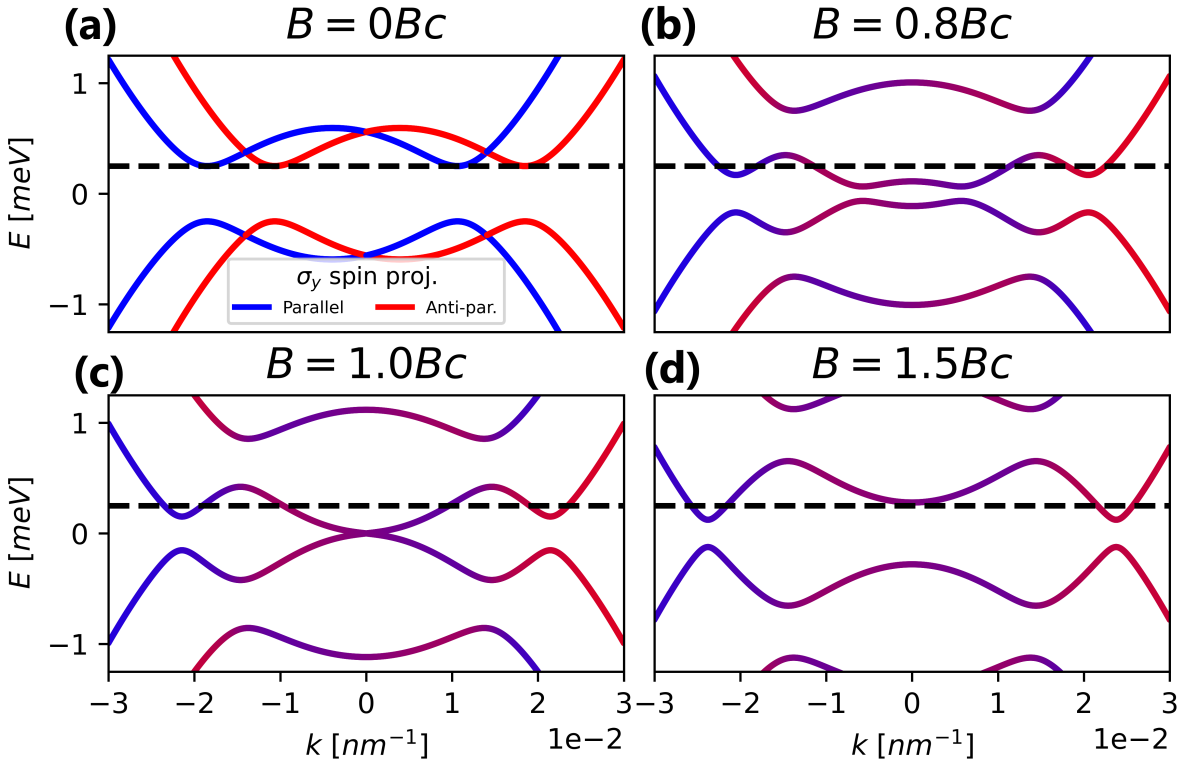

Figure 3.6: The dispersion relation of a superconducting Rashba nanowire at different field magnitudes. (a): at zero field we observe two bands with well-defined spin, which we represent with different colors. We mark with a black dashed line the superconducting gap, which coincides in value with the order parameter Δ. (b): as the field increases to the helical regime the two bands hybridize, locking spin to momentum, as can be seen by the bands becoming multicolored. We also note that the gap decreases. (c): at the critical field the gap closes at zero momentum, signaling a phase transition. (d): as the field increases further the gap reopens and the system enters in a topological regime. Parameters used: $\mu = 0.5meV$, $\alpha = 20nm.meV$ and $\Delta = 0.25meV$.

As we can see in Fig. 3.6(c), at this point the lower band of the positive spectrum has dipped in energy in the low momentum region up to the point of touching its hole counterpart exactly at $k = 0$. The band touching guarantees there are states at every energy value, even the ones close to zero. This is the gap closing we have been looking for and its signaling that a transition in happening in the system. By further increasing the field we see that the bands separate, opening the gap one more time. This is depicted in Fig. 3.6(c) and the system is then in a topologically different phase.

The aspects of the phase transition we have discussed so far are all pertaining to the bulk of the system. From the bulk-edge correspondence, however, we expect that a change in the topology of the bulk will result in the appearance of edge states [28]. In order to see those states we must turn ourselves to finite systems, which we do in the next sections.

3.4 The *tight-binding* formalism

As we have seen, the bulk of Rashba nanowires shows evidence of a topological phase transition and the development of a topological phase. We will now demonstrate that in a finite sized system, this topological phase is characterized by the presence of MBSs, which are exponentially

localized on the edges of the nanowire [26].

By using a finite nanowire, the translational symmetry is broken, rendering k-space ineffective as a tool. Therefore we move on to the *tight-binding* approach. We shall not derive this formalism here, but rather just translate the expressions we had for the continuum case into the tight-binding language. In practice, this consists of discretizing real space so that the Hamiltonian can ultimately be written as a finite-dimensional matrix. Then, only a set of discrete positions x_i become allowed and, because of this, the derivatives are now performed through the method of finite differences. They are given by

$$\frac{\partial}{\partial x}\hat{c}(x) \to \frac{\delta}{\delta x_i}\hat{c}_i \equiv \frac{\hat{c}_{i+1} - \hat{c}_{i-1}}{2a}, \tag{3.19a}$$

$$\frac{\partial^2}{\partial x^2}\hat{c}(x) \to \frac{\delta^2}{\delta x_i^2}\hat{c}_i \equiv \frac{\hat{c}_{i+1} - 2\hat{c}_i + \hat{c}_{i-1}}{a^2}, \tag{3.19b}$$

where we just introduced the notation $\hat{c}_i = \hat{c}(x_i)$ and a is the discretization step, the distance in real space between two fermionic sites i and $i+1$.

From the definitions above we can find out how to represent the different terms in the Hamiltonian. Starting with the kinetic term, one finds that it becomes

$$\hat{H}_{\text{Kin}} = \sum_{i,\sigma}\left[(2t-\mu)\hat{c}^\dagger_{i,\sigma}\hat{c}_{i,\sigma} - t\,(\hat{c}^\dagger_{i,\sigma}\hat{c}_{i+1,\sigma} + \hat{c}^\dagger_{i,\sigma}\hat{c}_{i-1,\sigma})\right], \tag{3.20}$$

where we just defined the quantity $t = \hbar^2/2m^*a^2$. The spin-orbit term, on its turn, becomes

$$\hat{H}_{\text{SO}} = \sum_i t_{\text{SO}}\left[\hat{c}^\dagger_{i,\uparrow}(\hat{c}_{i+1,\downarrow} - \hat{c}_{i-1,\downarrow}) - \hat{c}^\dagger_{i,\downarrow}(\hat{c}_{i+1,\uparrow} - \hat{c}_{i-1,\uparrow})\right], \tag{3.21}$$

where $t_{\text{SO}} = \alpha_R/2a$, while the Zeeman term is found to be

$$\hat{H}_{\text{Z}} = \sum_i B\left(\hat{c}^\dagger_{i,\uparrow}\hat{c}_{i,\downarrow} + \hat{c}^\dagger_{i,\downarrow}\hat{c}_{i,\uparrow}\right), \tag{3.22}$$

where B is again the Zeeman energy. Finally, for an order parameter of Δ, we find that the s-wave pairing in the tight-binding description is given by

$$\hat{H}_{\text{SC}} = \frac{1}{2}\sum_i\left[\Delta\left(\hat{c}^\dagger_{i,\uparrow}\hat{c}^\dagger_{i,\downarrow} - \hat{c}^\dagger_{i,\downarrow}\hat{c}^\dagger_{i,\uparrow}\right) + h.c.\right]. \tag{3.23}$$

Having these expressions, the next natural step would be to construct the corresponding BdG Hamiltonian. It is important to notice, however, that our basis for the BdG matrix can no longer be parametrized by the wavenumber, since that is not a good quantum number anymore. This means we can no longer parametrize the BdG Hamiltonians with respect to k as well. Instead, we must construct one big matrix that takes all fermionic sites into account and diagonalize it all at once. From a practical perspective, this matrix will have dimensions $4N \times 4N$, where the factors of 4 take the spin and particle-hole degrees of freedom into account. Likewise, the corresponding basis should have dimension $4N$ and we can construct it as

$$\hat{\Psi}^\dagger = \left(\hat{c}^\dagger_{1,\uparrow},\ \hat{c}^\dagger_{1,\downarrow},\ \hat{c}^\dagger_{2,\uparrow},\ ...,\ \hat{c}^\dagger_{N,\downarrow},\ \hat{c}_{1,\uparrow},\ \hat{c}_{1,\downarrow},\ \hat{c}_{2,\uparrow},\ ...,\ \hat{c}_{N,\downarrow}\right). \tag{3.24}$$

If we now define the building block matrices

$$h = \begin{pmatrix} 2t-\mu & B \\ B & 2t-\mu \end{pmatrix}, \quad v = \begin{pmatrix} -t & t_{\text{SO}} \\ -t_{\text{SO}} & -t \end{pmatrix}, \quad \delta = \begin{pmatrix} 0 & \Delta \\ -\Delta & 0 \end{pmatrix}, \tag{3.25}$$

the final form of the BdG Hamiltonian will be

$$H_{BdG} = \begin{pmatrix} h & v & 0 & .. & \delta & 0 & 0 & .. \\ v^\dagger & h & v & .. & 0 & \delta & 0 & .. \\ 0 & v^\dagger & h & .. & 0 & 0 & \delta & .. \\ : & : & : & : & : & : & : & : \\ \delta^\dagger & 0 & 0 & .. & -h^* & -v^* & 0 & .. \\ 0 & \delta^\dagger & 0 & .. & -v^T & -h^* & -v^* & .. \\ 0 & 0 & \delta^\dagger & .. & 0 & -v^T & -h^* & .. \\ : & : & : & : & : & : & : & : \end{pmatrix}. \tag{3.26}$$

It is fitting at this point to add a side note. For the matrix above we have chosen open boundary conditions, which correspond to a finite wire with its ends isolated from any leads or from each other. If we had instead chosen periodic boundary conditions we could emulate an infinite wire or at least a wire with both its ends connected. The only modification necessary for this would be to insert the elements v and $v^\dagger$ at the end points of the anti-diagonal of the first diagonal block and $-v^*$ and $-v^T$ for the second diagonal block. By inserting these elements alongside a phase e^{ikL} one could recover wavenumber as a parameter and find the same results we discussed for the bulk system. As that has been already done, we shall not dwell on this subject any longer. Instead, we shall turn to what is left, that is, to implement the open-boundary matrix above numerically, so we can finally find the spectrum of a finite superconducting Rashba nanowire, where the MBSs should be present.

3.5 Superconducting Rashba nanowires: edge properties

Having introduced the tools to study discrete systems, we now implement the discussed model numerically and diagonalize the matrices with respect to parameters of interest. This yields us the spectrum of these systems, where we expect to find the MBSs as low-energy states emerging in the topological phase. The low energy spectrum yielded by this method is not only useful to understand the emergence of MBSs, but allows for transport based studies, as done in Ref. [42]. As with the study of the bulk, we shall use the Zeeman field to tune our system into the different topological phases. In Fig. 3.7 we plot the energy levels as a function of the Zeeman field in units of the critical field B_c. A new parameter we have control of, in comparison to the bulk analysis, is the length of the system we are considering. This can be tuned by changing either the lattice distance a or the number of sites we consider in the space discretization.

In Fig. 3.7(a) we show the spectrum of a relatively short nanowire, 2000nm long. The first thing we should point out is that we observe a hard gap for low field values, characterized by a significant energy separation between the least energetic positive state and the most energetic negative state. This gap remains open for a considerable range of parameters, but its size decreases as the field increases. When the field eventually reaches its critical value B_c we find that the gap closes, which we mark with a green stripe on the plot. This was expected, as we saw the same thing happening for the bulk of this system and this observation can be interpreted as the magnetic field killing the Cooper pairs, a phenomenon that is well consolidated in literature [43]. As we increase the field further, we see that the gap reopens. As we discussed, the closing and reopening of the gap is a sign that a phase transition is underway, but this time it is accompanied by another interesting piece of evidence: the emergence of a pair of low-energy states, which we point out with a red arrow. After emerging, these states oscillate in energy with the field, crossing themselves a few times and they represent precursors of MBSs in our system.

We can start to see this by looking at how they behave with respect to system length. In Fig. 3.7(b) we make the same kind of plot for a longer nanowire, 8000nm long. We see many

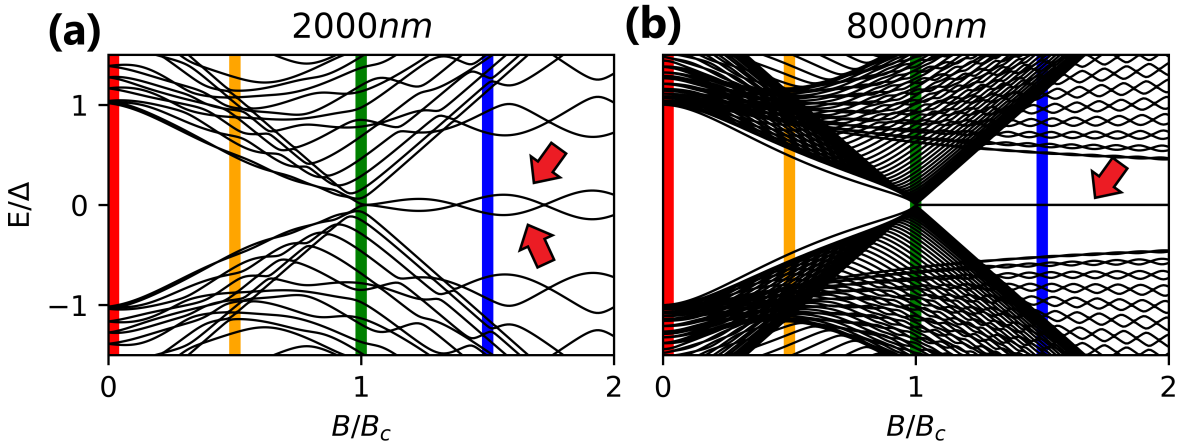

Figure 3.7: The spectrum of finite Rashba nanowires as a function of the Zeeman field. In panel (a) the wire is $2000nm$ long and we notice that a gap is present for low field values. As the field increases this gap decreases, reaching zero at the critical point (which we mark with a green stripe) and then reopening. This is compatible with what we saw in the analysis of the bulk. We also notice the emergence of a pair of low-energy states in the topological regime that oscillate in energy with respect to the field and which we highlight with arrows. If we turn to a longer nanowire, as in panel (b), where $L = 8000nm$, we see that these oscillations disappear as the states become pinned to zero energy. This behaviour points to some non-local property and evidences these states might be MBSs. The parameters used were $\mu = 0.5meV$, $\alpha = 20nm.meV$ and $\Delta = 0.25meV$.

of the main features are still there: a hard gap at low fields, a gap closing and reopening and the emergence of low-energy states after the transition. The main difference we notice, however, is that the energy of the emerging states has been greatly suppressed, to the point where the oscillations cannot be seen anymore at this energy scale. The reason for this, as it turns out, is that these states are localized at the edges of the nanowire and their finite energy comes from an overlap of the peaks from each edge.

One way to check these claims is by finding the energies for systems of different sizes. This is shown in Fig. 3.8, where the energy of the lowest state is calculated as a function of the lattice distance a. One can see that the energy does decrease, as we expected, but not monotonically. This is very similar to what we saw in the Kitaev model, where the energy split due to the finiteness of the chain had a modulated exponential behaviour. Although our system now is much more complicated, one sees that the same expression we used for the Kitaev model in Eq. (2.23) still works as an approximation as we fit that into the data with the black curve.

A more direct way to observe the edge-localization and the variation of overlap with system length is by plotting their wavefunctions. We do so in Fig. 3.9, where the wavefunction amplitude $|\Psi|$ of the least energetic positive state is shown as a function of the position along the nanowire. We show in blue a state in the topological regime, with $B = 1.5Bc$. We see in this case that the state concentrates around the edges of the system and its presence in the middle region is significantly suppressed. This is in stark contrast with what we would expect for a free electron, where the wavefunction is completely delocalized and which is closer to the behaviour of the zero field case, shown in red. We can then compare the cases of a shorter system as of Fig. 3.9(a) with a longer one such as of Fig. 3.9(b). We observe that they are very similar, but the edge-localization of the longer nanowire in the topological regime is even more pronounced, with the presence in the bulk being negligible. Hence, we can conclude that by making a longer nanowire the peaks are placed further apart so that the overlap, and hence the energy, decreases.

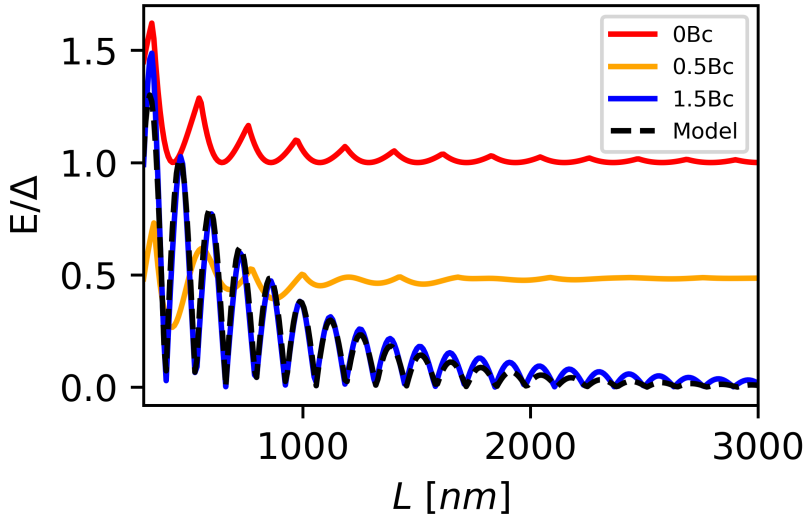

Figure 3.8: The energy of the lowest-lying state for various regimes as a function of the length of the system. We see that for low-fields (red and orange), the least energetic state has a weak dependence on length, specially for nanowires longer than $2000nm$. In the topological regime (blue), on the other hand, the lowest-lying states have an oscillatory and exponential dependence on length, becoming zero energy states in the limit of long systems. This is characteristic of MBSs and is well matched by the expression for the Majorana's energies of the Kitaev model of Eq. 2.23, as shown by the dashed black curve. Parameters used: $\mu = 0.5meV$, $\alpha = 20nm.meV$ and $\Delta = 0.25meV$.

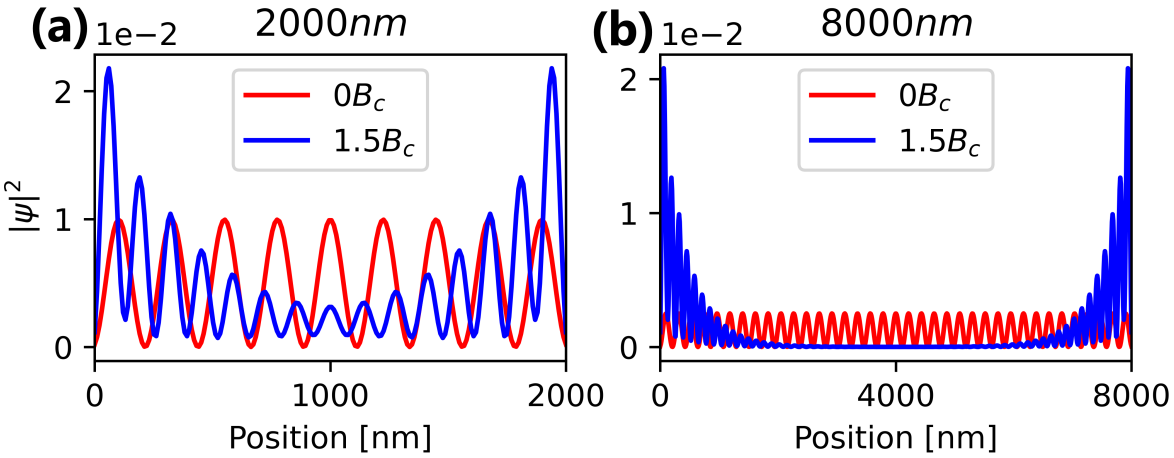

Figure 3.9: The wavefunction amplitudes of least energetic states in the zero-field (red) and topological (blue) regimes. In panel (a) we can see in blue that the non-local property of the MBS is already present for a $2000nm$ long nanowire, as the wavefunction is clearly peaked at both ends of the system, with little presence in the center. As we move to a longer wire in panel (b) we see these peaks become even more prominent and the presence in the center become negligible. For comparison, in both panels we also present, in red, the least-energetic state of the zero field regime, which is seen to be completely delocalized.

This is one of the main properties presented by the MBSs we saw in the Kitaev model and it is no coincidence. At this point we can affirm we have indeed a pair of MBSs in the system, but

some insight is needed in order to find them. Another fundamental characteristic of Majorana states is the fact that they are their own anti-particles. The antiparticles in the context of condensed matter can be understood as the hole counterpart of the state, which in the BdG formalism is simply found by making a particle-hole transformation. Here, this transformation is given by $P = (\tau_x \otimes \sigma_0)\mathcal{K}$ and one can check that our Hamiltonian of Eq. (3.26) anti-commutes with it. By applying the transformation to the energy eigenstates, one sees then that it takes the positive energy states into their counterparts of negative energy and vice-versa. This includes the low-energy states we have been discussing so far and hence we see they cannot be Majorana states as they are.

We point out, however, that in long nanowires they form an approximately degenerate manifold, since their energy is near-zero. Because of this, it makes sense to consider superpositions of those states, and by making symmetric and anti-symmetric combinations we find that we can build eigenstates of the particle-hole symmetry operator, satisfying the Majorana condition. These states are the celebrated Majorana Bound States we have been looking for. These states, of course, are not exact eigenstates of the energy, so we should expect them to evolve non-trivially. However, as long as the nanowire is long enough and we can initialize the system in one of these states, we could remain close to it for arbitrarily amounts of time. For a 8000nm long nanowire with the realistic parameter we have been using so far, for example, we find that the energy for these states stays peaks at around $0.2\mu eV$ for a field close to $2B_c$, while it can be two orders of magnitude smaller at fields just above B_c, which is compatible with literature [44]. This results in a period of around $20nm$ to $2\mu s$ for the time oscillations. The energy can be further decreased by tuning the field to a node, increasing the period even further.

We saw, then, that in much the same way one needs to make a change of basis to go from the Dirac to the Majorana representation in the Dirac equation, we also need to change the basis to find the MBSs in Rashba nanowires. Another interesting result is gained from this if we take a look at the wavefunctions in this new basis. One finds that through symmetric and anti-symmetric combinations the energy eigenstates cancel each other out at one end or another. What this means is that the MBSs of our system are each localized at one end of the wire, just as in the Kitaev model, and in Fig. 3.10 we plot their wavefunctions along the wire, with the symmetric state in orange and the anti-symmetric in green. The localization of those states, as it turns out, can be quantified by approximating them as evanescent waves $\psi(x) \approx e^{-x/xi_M} e^{\pm ik_F x}$ and finding the appropriate values for their coherence length ξ_M and Fermi wavenumber k_F. Since their wavefunctions are real, we actually look for symmetric or anti-symmetric combinations of states with both signs of k_F. The best fitting curve is shown in Fig. 3.10 by the dashed lines and their corresponding values are $\xi_M = 185(3)nm$ and $k_F = 2.427(3)\ 10^{-2} nm^{-1}$.

We have seen in this section first how helical states can arise in Rashba nanowires. We then saw how, with the introduction of conventional superconductivity, the system presents a topological phase transition marked by a gap closing, and we used the helical states we found to make evident the emergence of p-wave superconductivity. Finally, we saw how after this transition the system presents a pair of low-energy states from which we were able to construct MBSs that satisfy the Majorana condition and are localized at the edges of the system. Although all of these results are interesting by themselves and could be more deeply analyzed, we will now change our focus to more complex systems, where the Rashba nanowire will serve as a building block. In the next section we will study hybrid junctions and see the emerging MBSs interact with a different environment.

3.6 A connection to experiments

In the last decade, many reviews have been written not only on the theoretical development of platforms for Majorana Bound States, but also on the experimental implementation of such

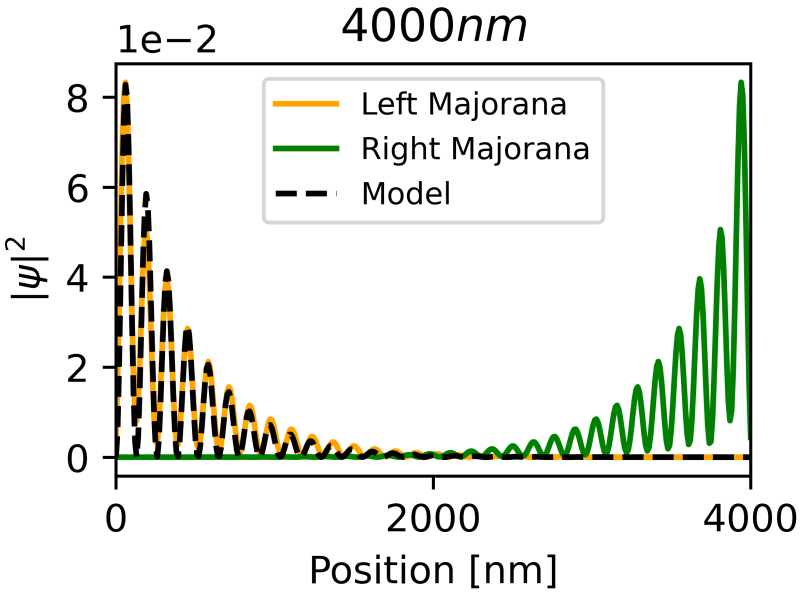

Figure 3.10: The wavefunction of the MBSs in the Majorana basis. We see that the peaks can indeed be separated through this transformation and their wavefunction can be then modeled by and oscillatory exponential, as shown by the dashed black curve.

platforms. An up-to-date example of the later is Ref. [45], where experiments involving spectroscopy and transport measurement of hybrid semiconductor-superconductor structures are discussed. We list here a few examples of such experiments that have relevance to this work.

One of the first publications of experimental results on the detection of signatures of Majorana Bound States on nanowires is that of Mourik *et al* [46]. In this 2012 paper we already see one of the most discussed evidences of these states, that is, the zero-bias conductance peaks. The idea behind the search for these peaks is that the MBSs, having a peculiar zero energy, should generate a distinct increase in conductance for voltage-biased transport experiments when this voltage is close to zero. The peaks, which were measured by the authors and by many other subsequent experiments, generated much excitement in the community. However, this was eventually met with skepticism. Although these are experimental signatures we expect and need to observe in a system with MBSs, it was later shown that they can be reproduced in these types of systems by many non-topological mechanisms.

This has led to much discussion, where experimental results which once had been interpreted as proof for the detection of MBSs were put into question. This is most clearly represented in the recent developments regarding a 2018 Nature paper by Zhang *et al* [47], where the authors had claimed to have detected yet another MBS signature, the quantization of conductance in these zero-bias peaks. After much debate and scrutiny, a replacement to the original paper was released in pre-print form [48] and the authors claim a retraction note is under preparation. The discussion is still lively, but the general consensus seems to be that this episode has made clear the need for the detection of more than only one signature.

In light of these recent developments, we also present here other studies and accomplishments of the last decade. A wide range of systems have been experimentally studied through spectroscopy by several groups, such as ferromagnetic atomic chains [49], hybrid nanowires with quantum dots [50] and pure nanowires with a focus on the splitting of Andreev Bound States [51]. Many other experimental studies have also been made on transport measurements, some of which are as the observation of a magnetically-driven supercurrent enhancement [52], gate tunability [53], multiple Andreev Reflections in highly transparent junctions [54], multiple Andreev

Bound States [55], and quantum dot parity effects [56]. The quality and techniques employed in the making of these platforms have also seen improvement, as exemplified by Ref. [35], where the authors were able to produce and experiment on nanowires fully enclosed in a superconducting shell, in contrast with the primitive idea showed earlier on this chapter, where the semiconducting part is simply deposited on the superconducting one.

Finally, we would also like to make a special mention to recent publications which have focused on the concomitant measurement of different MBS signatures [57], and the measurement of correlation of states at both ends of the nanowire, exploiting the non-local property of the MBSs [58].

Having seen that recent developments have been made not only on the theoretical side of the search for Majorana fermions, we will now end this chapter by taking a look at another point of view on the subject and study a particular application for these systems that has been only recently proposed.

3.7 Applications on Topological Quantum Computation

A very important problem faced today in the field of quantum computation is that of scalability: the capacity to increase a system in size at feasible and reasonable cost. This is a problem that is present in all sorts of platforms and the Rashba nanowire, with its fields, axes alignments and contact surfaces, is no exception. Among the proposed solutions to this problem are the ones by Karzig *et al* in Ref. [59], which we will briefly present and discuss here. In order to deal with these more complex problems where there are many topological nanowires involved we must turn to a minimal model, where we take the presence of the MBSs at the edges for granted and consider its interactions to neighboring structures through tunneling amplitudes. At this level of abstraction we can then study networks of nanowires where braiding can be performed.

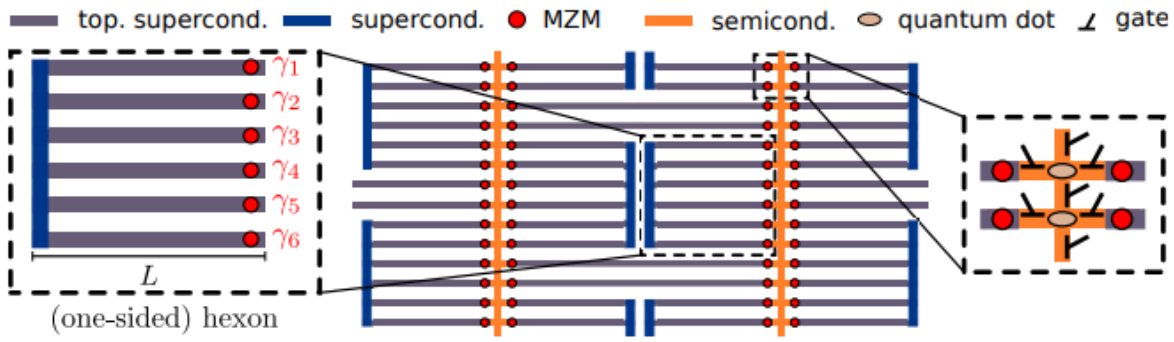

Figure 3.11: An example of a scalable *hexon* architecture. Figure from Ref [59].

An important part for achieving scalability is having building blocks for the system, which can be copied and wired together. The main block proposed in Karzig's work is represented in Fig. 3.11. As we can see, the *hexon*, as it was named by the authors, is comprised of six parallel nanowires (grey) which are joined together by a superconducting *backbone* (blue). Because of the parallel arrangement, a common axis exists for all nanowires along which a magnetic field can be placed and used to drive the system into the topological phase. In this phase it is expected that MBSs will arise at zero energy at the edges away from the backbone, while the ones close to it will hybridize. Only the zero energy modes (red) participate in the braiding protocols of this system and they are connected to each other through semiconductors (orange) while the coupling constants are controlled by gate voltages. The semiconductors are embedded with quantum dots which also take part in braiding. Finally, both the superconducting island and

the quantum dots are Coulomb-blockaded in order to prevent quasi-particle poisoning. Also, the quantum-dots are taken to be spin-polarized, thanks to the dominating magnetic field.

An important difference from this design to other proposed computational architectures is that instead of relying on adiabatic processes to perform braiding, Karzig's proposal makes use of the idea of forced measurements [1]. Closely related to the quantum Zeno effect [60], the idea behind this procedure is that by making repetitive measurements in non-compatible bases one can force the result of a measurement after a random but reasonably short amount of trials and errors. The measurement that is aimed to be forced in this architecture is that of the fermion parity associated with pairs of MBSs, since this could then be used for performing braiding operations. In order to make this measurements the author's proposal is to couple the pair of MBSs together through a quantum dot. This allows the MBSs to hybridize and causes a split in energy that is not compatible with the parity quantum number, meaning energy can serve as a second basis for the procedure. The authors then propose different methods to perform the actual measurement of the quantum numbers, such as spectroscopy, quantum dot occupation and differential capacitance. Whatever method used, the intended result is that at the end of a forced measurement the MBS parity can be set to even or odd, as wished.

A forced measurement procedure for MBSs i and j is mathematically represented by the projector

$$\Pi_0^{(jk)} = \frac{1 - i\gamma_j\gamma_k}{2} \tag{3.27}$$

With these projectors defined, the authors then show how a sequence of such measurements can lead to a braiding of two MBSs on the same island. In particular, they show that the exchange operation between MBSs 1 and 2, which is given by $R^{(12)} = (1+\gamma_1\gamma_2)/\sqrt{2}$, is obtained after performing the sequence $\Pi_0^{(34)}$, $\Pi_0^{(23)}$, $\Pi_0^{(13)}$ and $\Pi_0^{(34)}$. All that is left for interpreting this as a quantum logic gate is to define the computational basis. The authors define the qubit basis states as

$$|0\rangle = |p_{12} = p_{16} = -1\rangle \tag{3.28}$$

$$|1\rangle = |p_{12} = p_{16} = +1\rangle. \tag{3.29}$$

In this basis the operation $R^{(12)}$ described above and a similar exchange $R^{(25)}$ between MBSs 2 and 5 are written as

$$R^{(12)} = \begin{pmatrix} 1 & 0 \\ 0 & -i \end{pmatrix}, \tag{3.30}$$

$$R^{(25)} = \frac{1}{\sqrt{2}} \begin{pmatrix} 1 & i \\ i & 1 \end{pmatrix}. \tag{3.31}$$

The Hadamard gate is then expressed in terms of these two: $H = R^{(12)}R^{(25)}R^{(12)}$. We note here that although MBSs 4 and 5 are involved in the measurements for all these operations, they are disregarded in the computational basis. This is because they are used only as an ancillary pair and encode no information. Thus, although a superconducting island hosts three pairs of MBSs, only two pairs are used to store the qubit information.

By connecting different islands one is able to perform multi-qubit gates, such as the two-bit entangling Clifford gate

$$W = \begin{pmatrix} 1 & 0 & 0 & 0 \\ 0 & i & 0 & 0 \\ 0 & 0 & i & 0 \\ 0 & 0 & 0 & 1 \end{pmatrix}, \tag{3.32}$$

which is performed through the sequence $\Pi_0^{(34)}$, $\Pi_0^{(35)}$, $\Pi_0^{(5678)}$, $\Pi_0^{(45)}$ and $\Pi_0^{(34)}$. Combined, all these gates form a multi-qubit Clifford-complete gate set. The authors finally discuss how this set combined with a single non-Clifford gate would enable the system to perform universal quantum computation, such as a T gate. As stated by the authors, the ability to perform such a gate is equivalent to the ability of creating so-called "magic states"

$$\frac{1}{\sqrt{2}}\left(|0\rangle + e^{i\pi}|1\rangle\right), \tag{3.33}$$

which the authors then claim that these states could be created in their system since they can be distilled using only Clifford operations [61].

With this we conclude our review on this interesting proposal. Many other approaches for the application of MBSs on quantum computation have been proposed and much work remains to be done. An ubiquitous theme among these proposal is that of hybrid structures comprised of both superconducting and semiconducting parts. Motivated by this and by our previous discussions about MBS signature detection we will now turn to relatively more simple systems, but with strong experimental relevance and which can be studied in more detail: junctions with Rashba nanowires.

Chapter 4

Superconductor-semiconductor junctions in Rashba nanowires

So far we have considered homogeneous systems, where the parameters are constant throughout the whole nanowire. Many interesting phenomena involving Rashba nanowires, however, appear when considering hybrid structures [23]. These can be constructed by considering nanowires with spatially dependent parameters. For example, part of the nanowire can have its superconductivity taken away by removing the s-wave superconductor around it. These regions are denominated normal or normal-metal regions and we will use them to construct junctions. From the implementation point of view, this is done by simply setting δ in Eq. (3.26) to zero for the corresponding sites.

In this chapter we will consider two geometries. The first one, depicted in Fig. 4.1(a), is the NS junction, which is comprised of a normal (N) region on one end of the nanowire next to a superconducting (S) region. One interesting new phenomenon that occurs already in this configuration is that an electron traveling in the N region and hitting the NS interface may get reflected as a hole instead of a usual electron. This process is called the Andreev reflection and it transfers a Cooper pair from the N into the S region [62, 63].

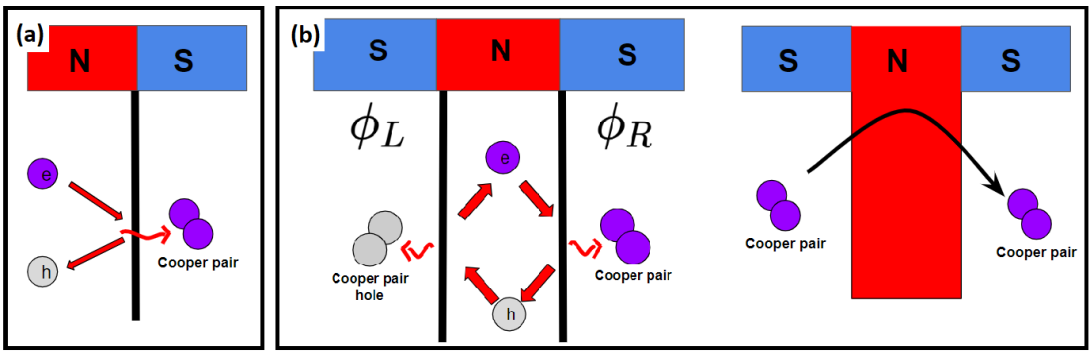

Figure 4.1: A sketch of the junctions considered and the important phenomena supported by them. In (a) is the NS junction and below it the Andreev reflection is depicted. In (b) we show a SNS junction with the cycle of Andreev reflections that generate an Andreev Bound State and a net transfer of Cooper pairs between the S regions, which generates the Josephson current.

In a different case we instead remove the proximitized s-wave superconductor from a middle region of the nanowire, leaving two separate S regions. This forms a SNS junction, Fig. 4.1(b), which also possesses interfaces between N and S regions, thus supporting Andreev reflections. Moreover, the hole generated in one of such reflections can hit the other interface and, with the reverse process, be reflected back as an electron. Multiple Andreev reflections result in

the formation of an Andreev Bound State (ABS) [64, 65]. This cycle of Andreev reflections is modulated by the superconducting phase and can result in a net current of Cooper pairs denominated a supercurrent [66], giving the ABSs an important role in transport dynamics in SNS junctions, as we will discuss in a later section of this chapter. Both these geometries were already studied in literature (see [34]) and most of this chapter is a review of those results, with a small original contribution at the end.

4.1 NS junctions

It is important to understand the interactions between the 1D topological superconductors we have seen and non-superconducting N regions, as shown in Fig. 4.1(a), because these are present in the experimental settings related to the measurement of MBSs, such as the studies of zero bias conductance peaks [23]. That is why we briefly study here the behaviour of the NS junctions. Several studies have been made in the subject in the last decade, including transport-based ones [67, 42, 68, 69] and cases where the N region is treated as a quantum dot [70, 71]

A NS junction can be modeled by putting the superconducting parameter to zero in one outer region of the nanowire while keeping the rest of the parameters constant. As we will see, the size of this region has significant effect on the energy levels of the system. However, as a starting point, let us consider the case of a nanowire with regions of equal proportions. By applying the above mentioned changes to the Hamiltonian of the system and numerically diagonalizing it for a 4000 nm long NS junction of equally sized regions we obtain the results shown in Fig. 4.2.

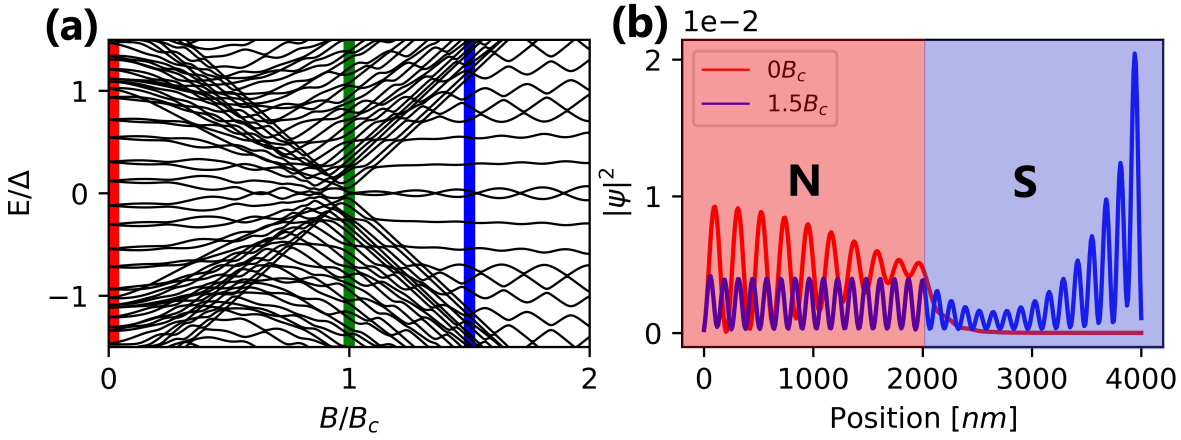

Figure 4.2: Panel (a): spectrum as a function of the Zeeman field, with the critical field marked in green. Panel (b): the wavefunctions of the lowest lying states for zero field (red) and $1.5B_c$ (blue). We have marked with stripes the field values for these states in the spectrum for reference. We point out that the subgap state represented for the zero field case is bound to the N region. Additionally, we see that in the topological phase there is one Majorana peak in the outer edge of the S region, but the other peak is not present, what can be interpreted as the other Majorana leaking into the N region. The parameters used were $\mu = 0.5$ meV and $\alpha_R = 20$ nm.meV for the whole system with $\Delta = 0.25$ meV in the S region and $\Delta = 0$ in the N region.

In Fig. 4.2(a) we show the energy spectrum as a function of the Zeeman field. As in the simple nanowire case we observe a gap closing and reopening at B_c, marked with a green stripe, with the emergence of low energy oscillating states at higher fields. This suggests that there is still a topological phase transition happening in the system. The main differing features from the

previous case are a smaller gap for higher fields and the presence of trivial finite-energy subgap states for low fields. These states originate from the N region, where the lack of superconductivity implies the lack of a gap. This can be checked by looking at the localization of such states, which we do in Fig. 4.2(b). In red we plot the wavefunction amplitude distribution across the system for the least energetic state at zero field. We verify that it is indeed bound to the N region (left half of the structure) being virtually not present inside the S region (right half). A similar profile is found for the other subgap states at low fields. In blue, on the other hand, we have plotted the wavefunction of the MBS at $1.1B_c$. We see that the outermost peak is still present and decaying exponentially towards the bulk, but the other peak, which we expected to find at the other end of the S region, is not there. This can be understood as the Majorana leaking into the N region, as was already observed in Refs. [72, 71], and is a sign that the topological states are significantly influenced by the surroundings of the nanowire. This should be kept in mind when studying transport properties of these systems.

Keeping these newfound properties in mind, we can then study how different proportions of the N and S regions affect the spectrum of NS junctions. It is important, though, to recall that the spectrum of a S region by itself depends on its length L_S, particularly in the topological regime, as we have seen in the previous chapter. In order to factor out these changes, we vary the length of a NS junction while keeping the L_S fixed at a value that allows for the emergence of the MBSs.

From a practical standpoint, this can be done in two ways. One possibility is to add more sites to the N region, increasing the total number of sites n in the tight-binding model. The second one would be to keep the number of sites fixed while converting sites at the interface from the S region to the N region by setting their local order parameter to zero and changing the inter-site distance a such as to keep $L_S = n_S\, a$ constant. We have compared the results of both methods and found no significant difference. The energy spectrum obtained for the first method are shown in Fig. 4.3, where we plot the energy of the lowest lying levels as a function of L_N for two values of the field.

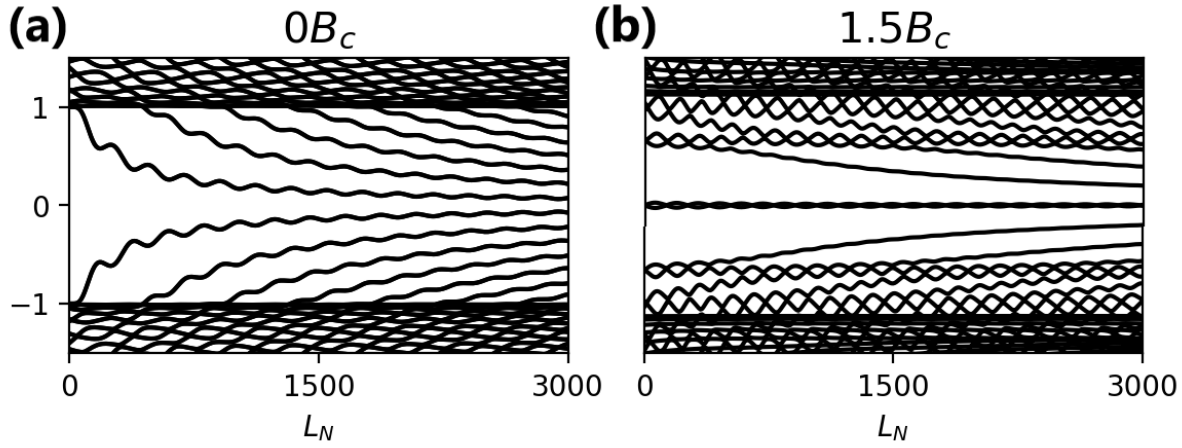

Figure 4.3: Spectrum as a function of the length of the N region for a junction with for zero field (a) and a topological value of $1.5B_c$ (b) values of the field. Here $L_S = 3000nm$. We can see that the trivial subgap states of panel (a) are present even for very small N regions, but the number of states increases as the junction gets longer. In panel (b) we see that the energy distance between the MBSs and the next least-energetic states decreases with L_N.

Fig. 4.3(a) corresponds to the zero field case and in it we see that the number of subgap states increases with the size of the N region, seemingly tending to a continuum of states in the limit $L_S/L_N \to \infty$. This behaviour of the spacing between energy levels is the one expected for

a confined particle and so this is a new indicative that these subgap states are bound to the N region, as we had already pointed out in Fig. 4.2(b). A very similar behaviour is found for the system in the topological regime, as depicted in Fig. 4.3(b). The main difference we see in this other case is the robust presence of the MBSs at near-zero energy and of a set of states forming a pseudo-gap, just as we have seen for a sole superconducting nanowire. These later states do not depend on L_N and are bound to the S region, in contrast to the converging states bound to the N region.

We conclude our analysis of the NS junction by pointing out that although the profile of the MBSs wavefunctions differs from the simple nanowire case on one side of the junction, the transformation to the Majorana basis in order to obtain an isolated peak still works. The symmetric and anti-symmetric combinations of the lowest energy eigenstates are localized on opposite edges of the nanowire, as we can see in Fig. 4.4. We see that the state corresponding to the Majorana far away from the interface has a behaviour equivalent to that of the simple nanowire case. On the other hand, the state located at the interface does have a seemingly exponential decay into the bulk of the superconducting region, but is also spread through the N region. Because energies of the original states are also approximately zero for sufficiently long S regions, our discussions regarding the validity of these linear combinations are also applicable here.

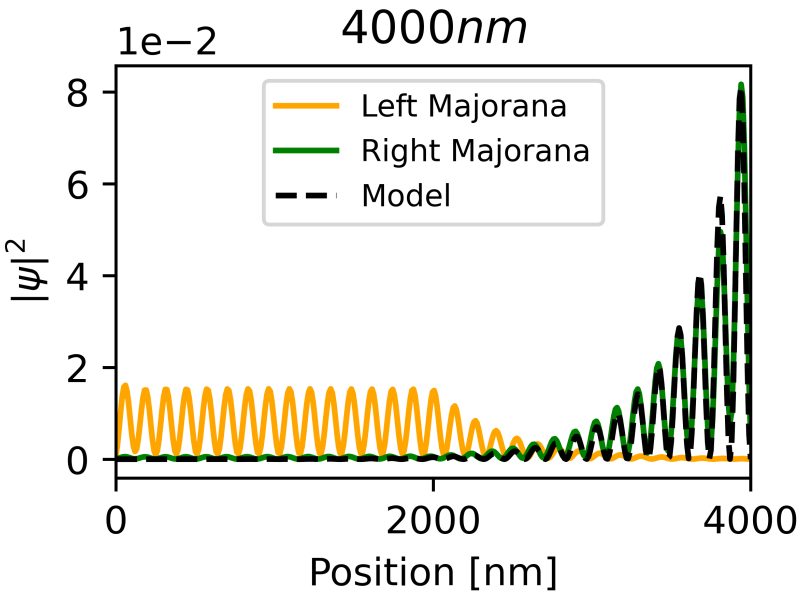

Figure 4.4: Wavefunction amplitude of the MBS of a NS junctions in the Majorana basis. We can see that the Majorana peak that is away from the NS interface behaves as usual and can be modeled by the same curve as before. In contrast, the peak at the interface leaks into the N region, where it becomes completely delocalized.

Having then seen that there is an important interplay between a Rashba nanowire in the topological phase and its neighboring non-superconducting regions, we move on to study a slightly more complex hybrid structure, the SNS junction.

4.2 SNS junctions

Differently from the structures discussed so far, SNS junctions present not only one S region, but two (see Fig. 4.1(b)). This gives importance to a parameter we have been ignoring so far:

the superconducting phase. The superconducting order parameter is in principle a complex quantity and its complex phase can be adjusted experimentally. By defining this phase for a given superconductor region labeled i as $\varphi_i = Arg(\Delta_i)$, the phase difference between the right and left S regions in a SNS junction is

$$\phi = \varphi_R - \varphi_L. \tag{4.1}$$

It is important here to remark that although the superconducting phase is defined up to a global phase, this phase difference is invariant under a change in this global quantity. Having this in mind, we can pick a reference frame and proceed to make the same kind of analysis we have done on our systems so far, which we do in Fig. 4.5. As a starting point, we study the cases of $\varphi = 0, \pi$ in the top and bottom panels, respectively, and plot their energy as a function of the Zeeman field on the left panels and the wavefunction amplitudes of their least energetic states on the right panels.

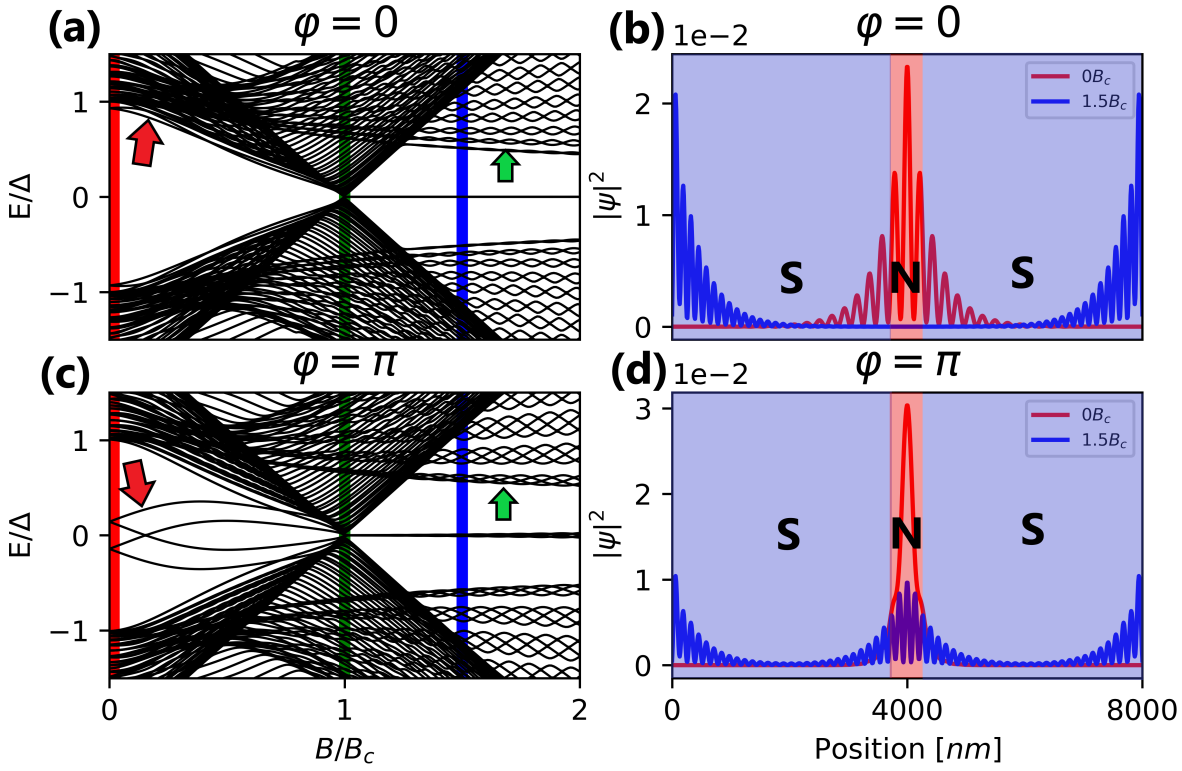

Figure 4.5: The low-energy spectrum and wavefunction amplitude for a SNS junction. (a) and (b): $\varphi = 0$ case. The MBSs appear only at the outer edges of the S regions. (c) and (d): $\varphi = \pi$ case. The MBS peaks appear at both the outer edges and at the interfaces. Closer inspection shows there are two pairs of MBSs at zero energy in this case. For both values of φ we see that the lowest-lying state of the trivial regime is bound to the N region. As we will see later, these are Andreev Bound States.

We have considered very long S regions, 3970nm each, and a comparatively very short N region of 60nm. From the spectrum of Fig. 4.5(a), for zero phase difference, we can see a phase transition present in the same way as the previous cases, with a gap closing and reopening at the critical field followed by the emergence of the near zero energy states. We can check that these states still behave as MBSs by looking at their wavefunctions. In Fig. 4.5(b) we plot in blue the wavefunction amplitude of one of these states and verify that it is indeed located at the outer ends of the nanowire, similarly to the simple nanowire case. Since a topological SNS junction

can be seen as two separate topological wires divided by a N region, one could naively expect to also see MBSs at the interfaces, but this is not the case. As we have seen in the NS junctions, the MBS peaks can leak into the normal region. This can in part explain why we don't see the peaks in the S regions, but since we also don't see a presence of the wavefunction inside the N region, there must be another important mechanism dictating the behaviour of these MBSs. Before we discuss this further, it is useful to point out another similarity to the NS junctions, that is, the presence of subgap states both in the trivial and topological regimes. These states, which we indicate in the spectrum with red and green arrows, respectively, are bound to the N region, as can be seen in the wavefunction plot for the trivial case (red). As we will see, these states can be interpreted as ABSs in the SNS junction and, as it turns out, one of these states is what has become of the missing MBS peaks of the topological regime.

In much the same way a short nanowire leads to the hybridization of the precursors of the MBSs, the proximity between the edges of the S regions, combined to the leaking of their localization into the the other regions, leads to these states acquiring a finite energy. Because of this, an ordinary transformation to the Majorana basis is not meaningful anymore, and the only true MBSs of the system are the ones located at the outer edges. As we will see later, this energy remains finite when the phase is changed to a finite value. Interestingly, the only exception to this observation occurs when we set $\varphi = \pi$. As can be seen in Fig. 4.5(c), in this case these states seem to disappear, but upon closer inspection one finds that they have become degenerate with the outer MBSs. By then looking at their wavefunction amplitude in Fig. 4.5(d), we can see that each of these zero energy states presents a profile with peaks at both the outer ends of the nanowire and around the N region.

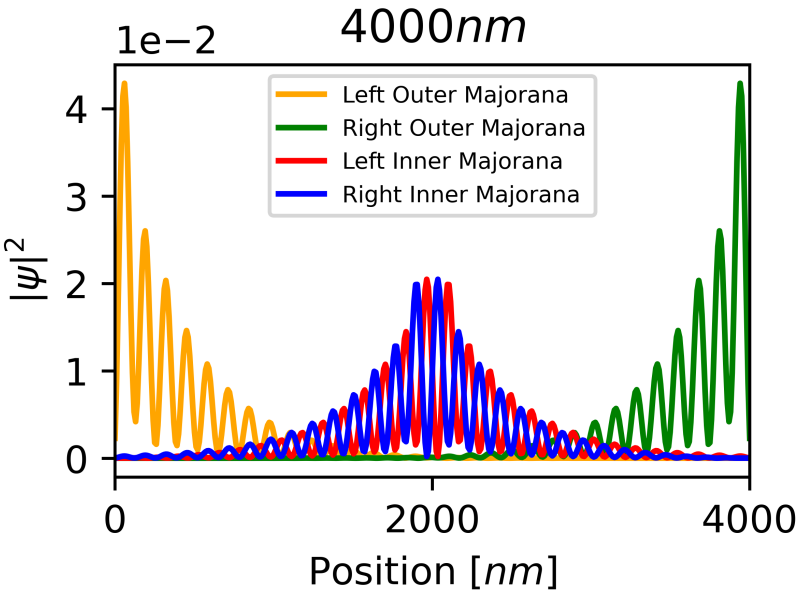

Figure 4.6: The wavefunction amplitude of the MBSs of an SNS junction in the Majorana basis for $\varphi = \pi$. We see peaks at both the outer edges and at the interface. The peaks at the interface have their peaks and troughs aligned, preventing hybridization. They also significantly leak into the opposite S region.

We now point out that the degeneracy allows for a Majorana transformation to be meaningful again and through it we are able to split the wavefunctions into separate peaks, finding well-localized Majorana fermions. This is depicted in Fig. 4.6, where each colored curve corresponds to a different linear combination of the original energy eigenstates. We observe that the inner Majoranas, that is, the ones located near the interfaces, seem to overlap significantly because

of leaking into the N region and the opposite S region. Upon closer inspection, however, one finds that their peaks and troughs are aligned and that the phase difference of π is somehow preventing them from acquiring energy. To understand this, we can turn to the the point of view of the Kitaev model, where the nanowire has been separated into two distinct topological domains, each with MBS peaks at its edges. The phase difference has inverted the coupling order between Majoranas on the right superconductor, so that the two chains cannot be linked together. The neighboring MBSs at the interfaces do not hybridize because they are of equal types. The takeaway message here is that at this value of φ a SNS junction can indeed host two pairs of MBSs, at least for wires with the right dimensions.

In order to understand why this is the case, we now study how the spectrum of a slightly shorter SNS junctions depends on this phase difference. In Fig. 4.7 we present results for a junction with an extremely short N region of 20 nm length by fixing the Zeeman field to different values. For panels (a-d) we use outer S regions 2000 nm long. In Fig. 4.7(a) we see the energy spectrum with respect to the phase difference in the absence of Zeeman field. We observe a gap compatible with the size of the superconducting parameter throughout all the range of ϕ, but also a distinct subgap state. This state is close to the bulk in energy when ϕ is zero, but dips as this parameter increases, reaching a minimum close to zero energy at $\phi = \pi$. The strong energy dependence on φ evidences that these states are indeed the before mentioned ABSs because the phase difference modulates the coherence of multiple Andreev reflections on the interfaces [64, 65]. As we will see in a moment, these states play an important role in the transport dynamics of SNS junctions.

For now, in Fig. 4.7(b) we show the case for a field of $0.5B_c$. Here we observe that the ABS we just discussed was actually degenerate and the presence of a Zeeman field split both curves, the bottom one dipping enough in energy to cross its electron-hole symmetric counterpart. Moreover we point out that there are two different gaps in the system, pointed by the black arrows. If we increase the field further up to its critical value $1B_c$ we obtain the results in Fig. 4.7(c). We see the closing of one of the gaps, just as in the previous systems, but also the presence of a phase-dependent state reaching a minimum at $\phi = \pi$. We also point out that the upper gap never closes and is not related to the topological phase transition. By driving the field up to $1.5B_c$, Fig. 4.7(d), we enter the topological regime and see a gap reopening, with a near zero energy state emerging, the MBS. Moreover, we see another subgap state appearing, with a shape similar to the ABS, and we observe this state pulls the MBS away from zero energy at $\phi = \pi$ and the two bands touch.

The energy splitting in the MBS bands at π is due to the finiteness of the S regions, as we can see by looking at Fig. 4.7(e). Here we see that the spectrum for a junction with 4000 nm long S regions does not present such a splitting, but instead the ABS-like bands cross at zero energy. We are thus again presented with the degeneration of the ABSs with the zero energy states. At $\varphi = \pi$ the only hybridization between the states at the interface is suppressed and the only way a finite energy can be acquired is through hybridization of these states with the outer MBSs. As we just saw this can be prevented by simply considering a longer nanowire.

We have seen here that the presence of ABSs and the phase difference between the S regions change significantly the behaviour of the low energy spectrum of hybrid structures based on Rashba nanowires, and that some experimentally controllable parameters can allow for the existence of two distinct pairs of MBSs. We will now see some consequences of this and, in addition, showcase a method for measuring the presence of these states experimentally through a phenomenon called the Josephson supercurrent.

4.3 Josephson supercurrent

The cycle of Andreev reflections implied in ABSs leads to the transference of Cooper pairs from one S region to another, as is sketched in Fig. 4.1(b). In principle, the mirror symmetry of

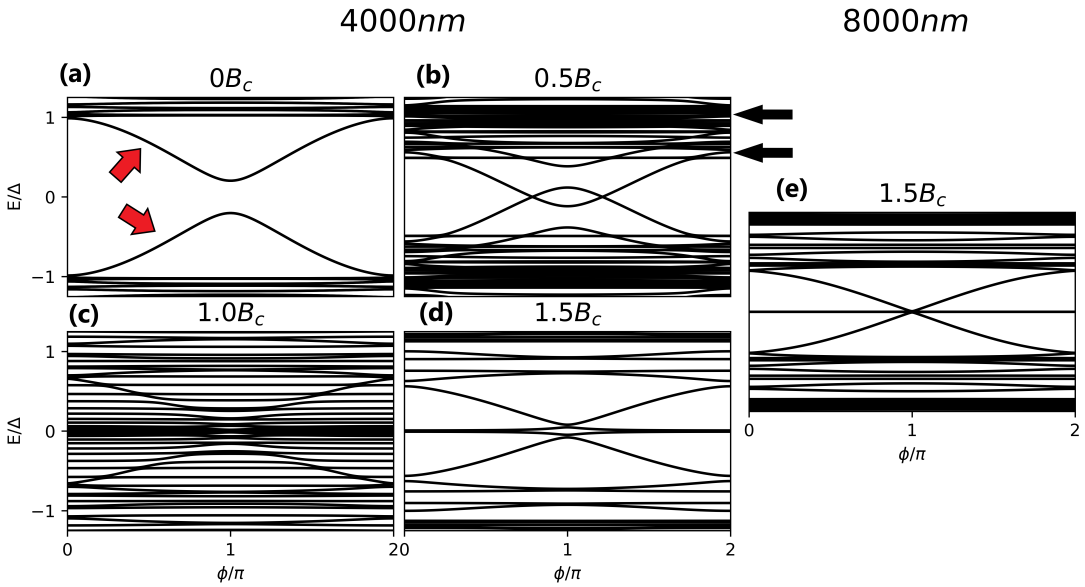

Figure 4.7: The energy spectrum of SNS junctions, in units of the superconducting parameter, as a function of the phase difference, in units of π. For panels (a-d) we consider a system with total length of $4000nm$. (a): zero-field case. We observe the presence of a gap, but also of a pair of strongly phase-dependent subgap states, denoted with arrows. These are ABSs and they are bound to the N region. (b): intermediate field case. We see the ABS split as the spin degeneracy is broken, with the lowest band crossing its hole counterpart. The superconducting gap decreases. (c): critical field case. At this point the gap completely closes, although a phase dependent state can be seen in the background. (d): topological regime. In this case we observe a pair of states pinned to zero energy, which are MBSs located at the outer edges of the nanowire. At $\varphi = \pi$, however, the ABSs come close to zero energy and hybridize with the MBSs. (e): topological regime for a longer nanowire. In this case the S regions are long enough so that hybridization is averted and the system presents 2 pairs of MBSs at $\varphi = \pi$.

a SNS junction would guarantee that this process happens as frequently as its inverse. However, as we have seen in the last section, there is a parameter in the system that breaks this mirror symmetry, the superconducting phase difference. As a consequence, this phase can give preference to the flow of Cooper pairs in a certain direction. This is the well known DC Josephson Effect [66] and leads to a measurable supercurrent across the junction. The AC Josephson effect also exists and has been studied in Rashba nanowire junctions [73]. This supercurrent can, in general, be calculated through [63]

$$I(\phi) = -\frac{e}{h}\sum_{p>0}\frac{dE_p}{d\phi}, \tag{4.2}$$

where E_p represents phase-dependent energy levels and the sum is over positive-valued states only. For a regular SNS junction the Josephson supercurrent has a simple sinusoidal dependence on φ, with nodes when this quantity is equal to a multiple of π. In our case, however, the presence of the Zeeman and spin-orbit terms modifies the profile of the supercurrent significantly. This can be seen by calculating the above expression for the supercurrent using the spectrum obtained in the last section, which we do in Fig. 4.8. We then plot the supercurrent I as a function of the phase difference for fixed values of the Zeeman field in Fig. 4.8(a), where we consider S regions with a length of 2000 nm. For zero field (red) the supercurrent shows a sine-like behaviour characteristic of the Josephson current, with a slight skewness towards the center node. As the

field becomes finite and increases (black, green and blue) we observe a reduction of the current amplitude, which is due to the decrease in effective superconductivity caused by the interplay between Cooper pairs and magnetic fields. The only distinct feature observed is a step-like curve for finite fields in the helical phase (black), which is due to the ABSs crossing observed in the spectrum in Fig. 4.7(b). By recalling the variations with respect to the system lengths we saw in the spectrum, a next natural step is to verify what effect they have in the supercurrent.

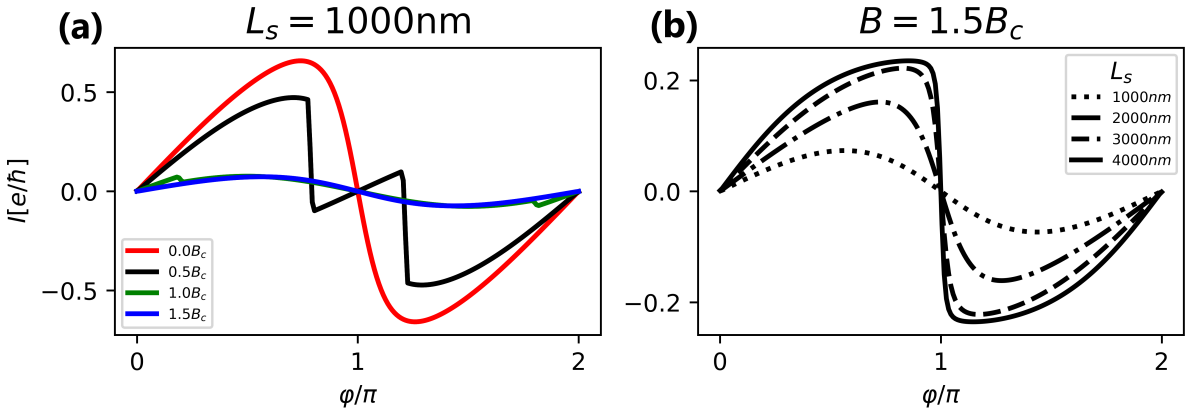

Figure 4.8: The supercurrent profile of SNS junctions with Rashba nanowires. (a): the supercurrent for different fields. Notice how the amplitude decreases with the field, but remains finite even after the phase transition. The sharp peaks of the helical regime is due to the ABS crossings. (b): supercurrent of the topological regime for different lengths of the S region. For short S regions we observe a typical Josephson curve, while for larger ones the curve becomes closer to a saw-tooth profile.

Although we don't show it here, we have seen that the the general profiles for the different cases remain the same independently from the characteristic lengths of the system, including the step-like behaviour of the helical case. The only exception to this is the case of a field in the topological regime (blue). For short S regions this case presents a profile almost identical to the case of a critical field (green), which is essentially the same as the zero field case but with a smaller amplitude. In Fig. 4.8(b) we plot the supercurrent profile in the topological regime for different lengths of the S region. It is clear from these curves that as L_S increases the skewness of the profile also increases, becoming closer to two linear curves joined together by a sharp drop in $\varphi = \pi$. When the S regions are long enough, the curve becomes what is known as a saw-tooth profile [74]. The dependence on length is a sign that this is related to non-local phenomena. Additionally, this transition happens around the same length for which a nanowire becomes capable of hosting MBSs. Together, these hint to the possibility that the MBSs themselves might be responsible for this signature in the supercurrent. We find out that this is indeed the case when we analyze the individual contributions to the supercurrent in Fig. 4.9. First, we see that the the outer MBSs (red) have virtually zero influence on the supercurrent, which is expected, since their origin is unrelated to the ABSs responsible for supercurrent transport across the junction. Next, the bulk, or quasi-continuum, states (green) have a small and negative contribution, although some of them are localized in the N region. Finally, we see that the inner MBSs (blue), that is, the ones localized at the junction, are responsible for the saw-tooth shape and contribute the most to the total supercurrent (black).

What we can conclude from this is that although the supercurrent carries no significant information on the MBSs at the outer edges of a SNS junction, it can signal the presence of MBSs at the inner interfaces, thus serving as a detection tool for these elusive states. This is extremely relevant because, as has been pointed out by recent literature [48], the transport-based detection protocols commonly considered such as the ones involving zero-bias peaks have

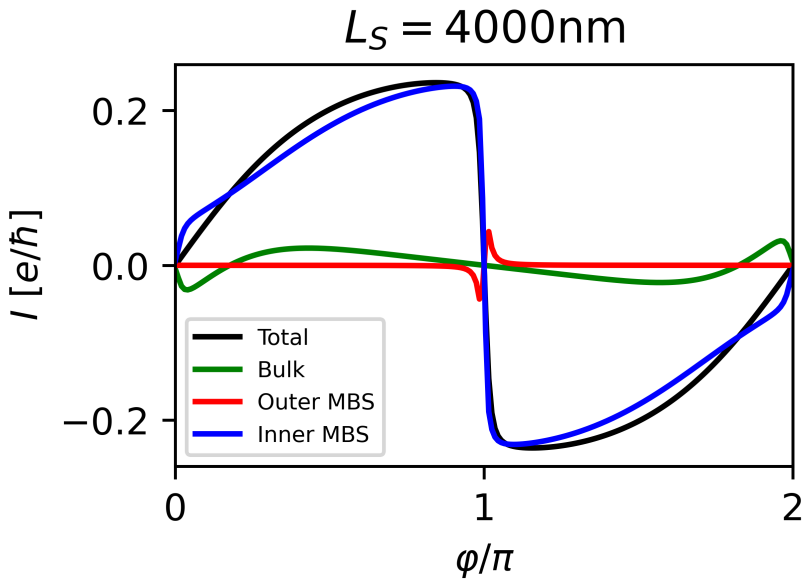

Figure 4.9: The contributions to the supercurrent as a function of phase difference for a SNS junction with 4000 nm long S regions. We observe the contribution from the outer MBS (red) is negligible, while the contributions from the bulk (green) is small and negative. We see that the inner MBS (blue) contributes the most towards the total (black) and is responsible for the saw-tooth shape.

difficulty discerning trivial zero energy states from topological ones. The supercurrent profile, as we have seen, is capable of making this distinction already by qualitatively comparing the curves. It is interesting, however, to have a more quantitative measure for the presence of topological zero energy states. Considering that the main property of a saw-tooth profile is arguably the sharp drop between consecutive linear sections, it is useful to study the derivative of the supercurrent at this transition point. The idea behind it is that a sinusoidal curve with amplitude I_c will yield a derivative of $-I_c$ at this point, whereas a perfect saw-tooth profile would yield a value of minus infinity. Thus, for comparative reasons, we start by calculating the derivative of the supercurrents for different fields and nanowire lengths and plot it in Fig. 4.10. Since we are only interested in the relative magnitude of the derivative at the nodal point with respect to the curve and we have already seen that the Zeeman field and the system lengths can affect the supercurrent amplitude, we have factored out this quantity.

We show how the profile changes for different field values in Fig. 4.10(a) for short S regions and observe that the sharp transitions of the helical regime (black) translate into distinct peaks. We also observe similar peaks appearing further away from $\varphi = \pi$ at the critical field (green), due to some small discontinuities in the profile that were harder to see in the previous plot. We stress that these peaks are due to the crossing of the ABS bands in the spectrum and that this crossing moves away from $\varphi = \pi$ as the field increases, which is compatible with what we see in the figure. We also observe that, interestingly, in the topological regime (blue) the system behaves very closely to an ordinary Josephson junction as the derivative of the current is close to a cosine curve. Lastly, we point out that the zero-field case (red) distances itself from this cosine behaviour by presenting a bump around $\varphi = \pi$, which is due to the skewness we discussed above. This is already a sign that peaks of the supercurrent derivative can appear in at this point even in trivial regimes, a fact we must beware of.

If we now move on to study the dependence of the supercurrent derivative on the S length, we see in Fig. 4.10(b) that as the S regions surpass a threshold of around 2000nm, a bump at the nodal point also appears for the topological regime. As L_S increases this bump gets taller

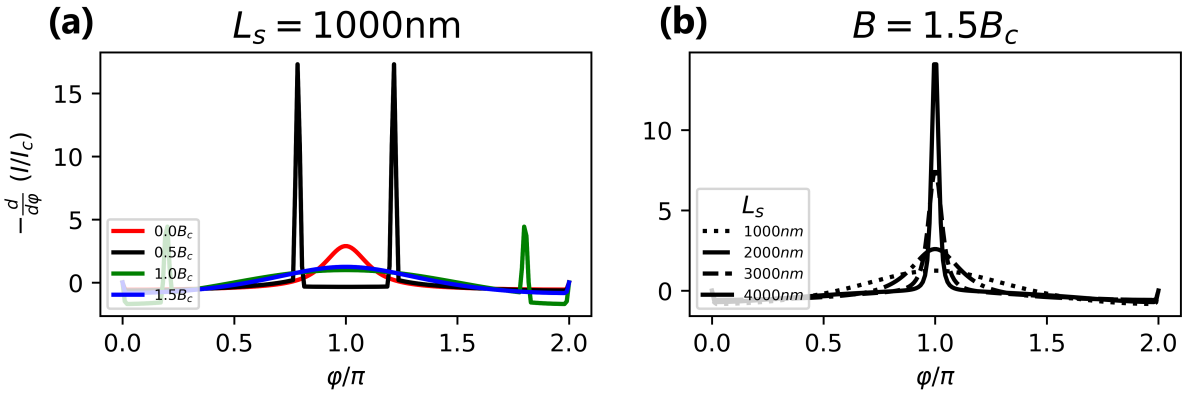

Figure 4.10: The derivative of the supercurrent for SNS junctions. (a): comparing the curves for different fields we see that for a short S region the zero-field regime (red) presents a bump at $\varphi = \pi$, while the topological regime (blue) behaves as an ordinary Josephson junction. (b): comparing the curves for different values of L_S, we see that longer nanowires show peak at $\varphi = \pi$, which gets sharper as the length increases.

and narrower, becoming a distinct peak. This is a consequence of the MBSs' emergence, as we have discussed before, but now put in a way that is more easily quantified. The height of the peaks can be measured and compared, which we'll do in a moment. However, before we do so and in order to get an even clearer view of what changes are relevant and which ones are mere fluctuation, we consider the logarithm of this quantity, defining what we will call the *sharpness* of the junction:

$$\mathcal{S} = \ln \left| \frac{d(I/I_c)}{d\varphi}|_{\varphi=\pi} \right|. \tag{4.3}$$

With this objective and easily obtained measure of whether a SNS junction is closer to hosting MBSs at the interfaces or behaving as an ordinary Josephson junction, we can subsequently study how this quantity depends on the system lengths, which we do in Fig. 4.11.

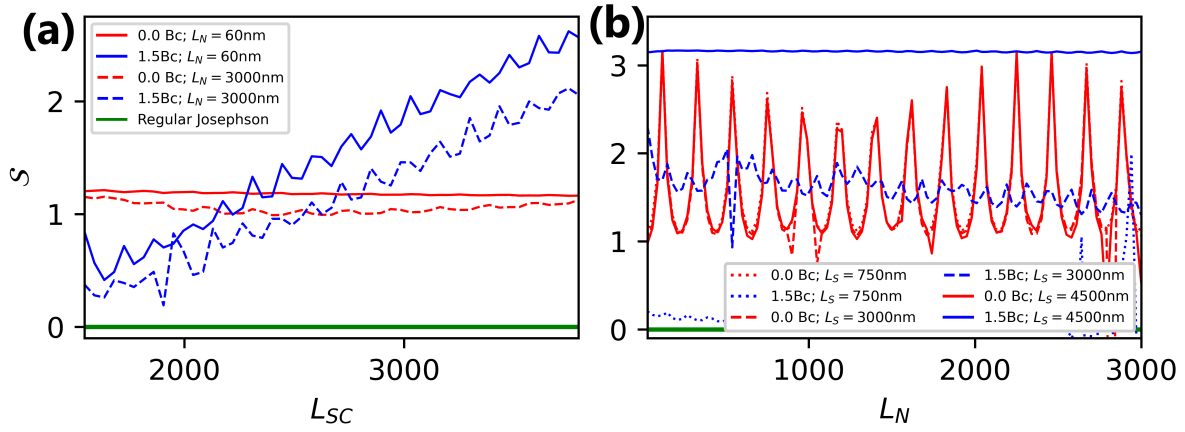

Figure 4.11: The effect of system lengths on the *sharpness* of the junction for the zero-field (red) and topological (blue) regimes. In panel (a) we can see that $\mathcal{S}$ increases linearly with L_N for the topological regime, while it remains constant for the zero-field one. In panel (b) we see that a change in L_N leads to strong oscillations in $\mathcal{S}$ for the zero-field case, but not for the topological one.

In order to vary the system lengths we have opted for adding sites to the corresponding region in our tight-binding approximation. In Fig. 4.11(a) we have fixed the length of the N region and varied the number of sites in the outer S regions, thus varying L_S. We have considered two values for L_N: 60nm, which we plot in solid lines, and 3000nm, in dashed lines. We can see from this data is that the zero field case (red) shows a $\mathcal{S}$ with little to no dependence on L_S. We see that it is distinguished from an ideal Josephson junction (green) only by a constant, which is due to the already mentioned natural skewness of the system. The topological case (blue), on the other hand, shows a distinguished dependence on L_S, with a linear behaviour. We see that for short S regions the junction behaves more like an ordinary Josephson junction, since the wire is not capable of hosting MBSs. At some point around $L_S \approx 2000 \sim 3000$nm, however, the sharpness of the topological regime surpasses that of the trivial one and keeps increasing linearly. Additionally, we also notice that although these observations are valid for both values of L_N considered, the two curves are slightly offset. This instigates an investigation on how the sharpness depends on L_N, which we do in Fig. 4.11(b).

Again, we see that the trivial regime (red), presents no large scale dependence, with fluctuations only. These fluctuations are likely due to the addition of new sites caused by the method chosen pushing around the other states. The dashed, dotted and solid curves represent different values of L_S and we see again that the trivial phase seems to behave the same independently of this value. Interestingly, the curves representing the topological phase (blue) are very well separated between themselves. We see that they have in general a flat behaviour, with a very small S region of 750nm length (line) having a sharpness very similar to the Josephson reference, while a very long S region of 4500nm (solid) stays constant just above $\mathcal{S} = 3$. We found, however, that intermediate values of L_S, such as the 3000nm case we present (dashed), slightly deviate from this by showing some minor oscillations and a slow descent as L_N increases. This last feature is in accordance with the offset we saw between the curves for the topological phase in panel (a) and here we see that this offset should vanish at large enough S regions.

A last very important observation that must be made from this data is that the sharpness of the trivial regime oscillates very strongly and quickly with L_N, reaching values comparable to that of a very long junction. Just observing a saw-tooth-like profile for a given SNS junction is not enough to conclude it is in the topological phase and hosting a pair of MBSs at the interface. In order to distinguish between trivial and topological states using the above defined sharpness we must consider its dependence on L_S. As we saw, the supercurrent profile generated by topological states becomes increasingly sharper as the S regions become longer because the overlap between the inner and outer MBS peaks diminishes, allowing for the ABS at the junction to reach zero energy. This doesn't happen for the trivial regime, on the other hand, because its spectrum doesn't share the same non-locality properties and hence does not depend significantly on L_S.

We here conclude our study of junctions with Rashba nanowires. We have seen that in the topological regime, the presence of a neighboring normal region causes a Majorana peak to leak out of the S region, as in the NS junction. We then saw that when the N region is surrounded by two different topological S regions, such as in an SNS junction, this leads in general to an overlap of the Majorana peaks that form the Andreev Bound State, giving it a finite energy. It is only when the phase difference across the junction equals to π that the overlap cancels out and the state's energy becomes zero. We also saw that still in this case the state can gain a finite energy if the S regions are not long enough.

Next, we have calculated from the spectrum the Josephson supercurrent generated by the phase difference. We saw that in general the profile of such supercurrents are very similar to those of an ordinary Josephson junction, but that a saw-tooth behaviour can emerge in certain situations. We have introduced a quantity we have named the *sharpness* and shown how it can quantify this behaviour and differentiate between trivial and topological states when the length of the S regions is varied. This enables the use of the supercurrent profile as a signature detection

of MBSs. Finally, we stress that the non-locality of the MBSs is an ubiquitous observation among the phenomena we have studied here.

Chapter 5

Conclusions and outlook

In this work we have reviewed studies on the low energy spectrum of Rashba nanowires. In the non-superconducting case we saw how the interplay between the Rashba spin-orbit coupling and an external field generates helical states, where spin and momentum are locked together. We then used this knowledge to study superconducting nanowires, where we reproduced the appearance of p-wave superconductivity in the helical bands. We then reviewed how, similarly to the Kitaev model, this system also presents a topological phase transition characterized by a gap closing and reopening. By moving to a tight-binding approach we were able to verify that for a finite sized system the phase transition is accompanied by the emergence of non-local edge-localized states, a phenomenon well-known in literature. The energy of these states oscillates with respect to the Zeeman field and decrease exponentially with system length. For long enough nanowires these states can be approximated as having zero energy, satisfying the conditions of Majorana Bound States.

In the last Chapter, we have turned towards hybrid systems constructed with these nanowires, namely NS and SNS junctions. We reproduced and discussed the new phenomena that has been shown to arise in these scenarios. In the NS junctions we were able to see how the Majorana peak located next to a normal region leaks into it, losing its exponential localization. In SNS junctions we observed that this leads to a hybridization of the MBSs located near the NS interfaces. We also saw that a superconducting phase of $\varphi = \pi$ can prevent this hybridization, at which point there are two pairs of true MBSs in the system. We have also made a connection to the Andreev Bound State that is expected to arise in such junctions.

We have finally completed the discussion by calculating the Josephson current in these junctions due to a finite phase difference. We saw that in many cases the profile of the supercurrent

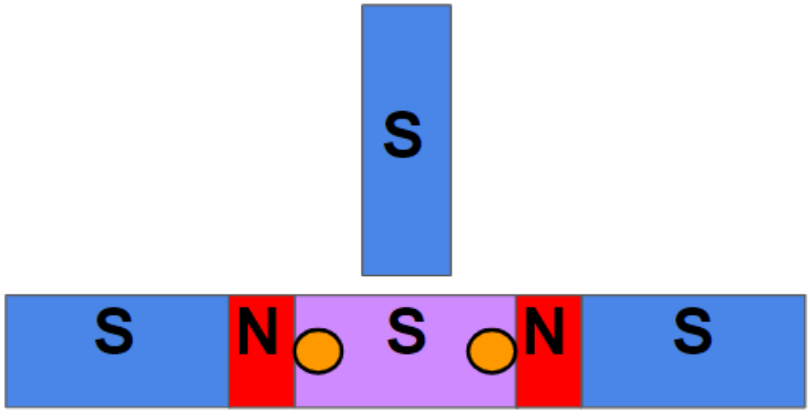

Figure 5.1: Multiterminal geometry.

has a usual sinusoidal behaviour, but that in some regimes new behaviour appears. Particularly, we saw how a saw-tooth profile always arises in the topological regime if the superconducting regions are long enough. We also saw that a similar curve can be reproduced in certain instances of the zero-field regime, which then led us to study the dependence of these with respect to the system lengths. Although all of these results were already observed in literature, we have introduced a new objective quantity to differentiate between the two main profile types, that, to the best of our knowledge, had not been studied yet. We then verified that as we increase the length of S regions, this quantity remains constant for the zero-field regime while it increases linearly for the topological one. We thus propose this method as a valid procedure for distinguishing topological from trivial states in systems with Rashba nanowires.

A next step that makes itself natural in this investigation would be the study of more complex junctions, called multi-terminal junctions, which are comprised of more creative combinations of N and S regions. One such system is the double Josephson junction, or SNSNS junction, depicted in Fig. 5.1, which we are currently studying. These types of junctions have become prominent in recent years due to the possible emergence of topology without intrinsically topological materials [75, 76, 77, 78, 79].

Appendix A

We show the proofs of some calculations regarding the Kitaev model.

A.1 Kitaev Hamiltonian in Majorana basis

Here we show how to derive the Kitaev Hamiltonian in the Majorana basis as in Eq. (2.20) from the usual fermionic form presented in Eq. (2.17). In order to do so we calculate first the inverse relation of Eq. (2.18), so we can express the original fermionic operators as

$$\begin{aligned}\hat{a}_j &= e^{-i\frac{\theta}{2}}\ \frac{(\hat{\gamma}_j^A + i\hat{\gamma}_j^B)}{2},\\ \hat{a}_j^\dagger &= e^{+i\frac{\theta}{2}}\ \frac{(\hat{\gamma}_j^A - i\hat{\gamma}_j^B)}{2}.\end{aligned} \tag{A.1}$$

We now substitute these expressions in the Kitaev Hamiltonian and apply the anti-commutation relations. In order to keep track of the calculations we do one term at a time. Starting with the chemical potential part,

$$\begin{aligned}\hat{H}_\mu &= -\mu\sum_j(\hat{a}_j^\dagger\hat{a}_j - \tfrac{1}{2})\\ &= -\mu\sum_j((e^{+i\frac{\theta}{2}}\ \frac{(\hat{\gamma}_j^A - i\hat{\gamma}_j^B)}{2})(e^{-i\frac{\theta}{2}}\ \frac{(\hat{\gamma}_j^A + i\hat{\gamma}_j^B)}{2}) - \tfrac{1}{2})\\ &= -\frac{\mu}{4}\sum_j\left((\hat{\gamma}_j^A)^2 - i\hat{\gamma}_j^B\hat{\gamma}_j^A + i\hat{\gamma}_j^A\hat{\gamma}_j^B + (\hat{\gamma}_j^B)^2 - 2\right)\\ &= -\frac{\mu}{2}\sum_j i\ \hat{\gamma}_j^A\hat{\gamma}_j^B.\end{aligned} \tag{A.2}$$

The tunneling term evaluates to

$$\begin{aligned}\hat{H}_t &= -t\sum_j(\hat{a}_j^\dagger\hat{a}_{j+1} + \hat{a}_{j+1}^\dagger\hat{a}_j)\\ &= -\frac{t}{4}\sum_j\left((\hat{\gamma}_j^A - i\hat{\gamma}_j^B)(\hat{\gamma}_{j+1}^A + i\hat{\gamma}_{j+1}^B) + (\hat{\gamma}_{j+1}^A - i\hat{\gamma}_{j+1}^B)(\hat{\gamma}_j^A + i\hat{\gamma}_j^B)\right)\\ &= -\frac{t}{4}\sum_j(\hat{\gamma}_j^A\hat{\gamma}_{j+1}^A - i\hat{\gamma}_j^B\hat{\gamma}_{j+1}^A + i\hat{\gamma}_j^A\hat{\gamma}_{j+1}^B + \hat{\gamma}_j^B\hat{\gamma}_{j+1}^B + \hat{\gamma}_{j+1}^A\hat{\gamma}_j^A - i\hat{\gamma}_{j+1}^B\hat{\gamma}_j^A + i\hat{\gamma}_{j+1}^A\hat{\gamma}_j^B + \hat{\gamma}_{j+1}^B\hat{\gamma}_j^B)\\ &= -\frac{t}{4}\sum_j(-i\hat{\gamma}_j^B\hat{\gamma}_{j+1}^A + i\hat{\gamma}_j^A\hat{\gamma}_{j+1}^B - i\hat{\gamma}_{j+1}^B\hat{\gamma}_j^A + i\hat{\gamma}_{j+1}^A\hat{\gamma}_j^B)\\ &= -\frac{t}{2}\sum_j i\ (\hat{\gamma}_j^A\hat{\gamma}_{j+1}^B - \hat{\gamma}_j^B\hat{\gamma}_{j+1}^A).\end{aligned} \tag{A.3}$$

We then compute the first part of the superconducting term,

$$\begin{aligned}\hat{H}_\Delta &= \Delta \sum_j \hat{a}_j \hat{a}_{j+1} \\ &= \frac{\Delta}{4} \sum_j e^{-i\theta} (\hat{\gamma}_j^A + i\hat{\gamma}_j^B)(\hat{\gamma}_{j+1}^A + i\hat{\gamma}_{j+1}^B) \\ &= \frac{|\Delta|}{4} \sum_j (\hat{\gamma}_j^A \hat{\gamma}_{j+1}^A + i\hat{\gamma}_j^B \hat{\gamma}_{j+1}^A + i\hat{\gamma}_j^A \hat{\gamma}_{j+1}^B - \hat{\gamma}_j^B \hat{\gamma}_{j+1}^B), \end{aligned} \tag{A.4}$$

and then add it to its Hermitian conjugate in order to obtain

$$\begin{aligned}\hat{H}_{SC} &= \hat{H}_\Delta + \hat{H}_\Delta^\dagger \\ &= \frac{|\Delta|}{4} \sum_j (\hat{\gamma}_j^A \hat{\gamma}_{j+1}^A + i\hat{\gamma}_j^B \hat{\gamma}_{j+1}^A + i\hat{\gamma}_j^A \hat{\gamma}_{j+1}^B - \hat{\gamma}_j^B \hat{\gamma}_{j+1}^B + \hat{\gamma}_{j+1}^A \hat{\gamma}_j^A - i\hat{\gamma}_{j+1}^A \hat{\gamma}_j^B - i\hat{\gamma}_{j+1}^B \hat{\gamma}_j^A - \hat{\gamma}_{j+1}^B \hat{\gamma}_j^B) \\ &= \frac{|\Delta|}{2} \sum_j i(\hat{\gamma}_j^A \hat{\gamma}_{j+1}^B + \hat{\gamma}_j^B \hat{\gamma}_{j+1}^A). \end{aligned} \tag{A.5}$$

Putting everything together, we finally obtain the desired expression:

$$\begin{aligned}\hat{H} &= \hat{H}_\mu + \hat{H}_t + \hat{H}_{SC} \\ &= \sum_j \left[-\frac{i\mu}{2} (\hat{\gamma}_j^A \hat{\gamma}_j^B) - \frac{it}{2} (\hat{\gamma}_j^A \hat{\gamma}_{j+1}^B - \hat{\gamma}_j^B \hat{\gamma}_{j+1}^A) + \frac{i|\Delta|}{2} (\hat{\gamma}_j^A \hat{\gamma}_{j+1}^B + \hat{\gamma}_j^B \hat{\gamma}_{j+1}^A) \right] \\ &= \frac{i}{2} \sum_j \left[-\mu(\hat{\gamma}_j^A \hat{\gamma}_j^B) + (|\Delta| + t)(\hat{\gamma}_j^B \hat{\gamma}_{j+1}^A) + (|\Delta| - t)(\hat{\gamma}_j^A \hat{\gamma}_{j+1}^B) \right]. \end{aligned} \tag{A.6}$$

A.2 Expression for topological limit of the Kitaev Hamiltonian

We show that the expression for the topological limit case of the Kitaev Hamiltonian in Eq. (2.21) holds. We first invert the expression for $\hat{b}_j$ in order to obtain

$$\begin{aligned}\hat{\gamma}_{j+1}^A &= -i(\hat{b}_j - \hat{b}_j^\dagger), \\ \hat{\gamma}_j^B &= \hat{b}_j^\dagger + \hat{b}_j, \end{aligned} \tag{A.7}$$

so that, together with the anti-commutation relations of Eq. (2.19), the Hamiltonian of Eq. (2.21) can be rewritten as

$$\begin{aligned}\hat{H}\big|_{\mu=0, t=|\Delta|} &= i \sum_{j=1}^{N-1} t\ (\hat{\gamma}_j^B \hat{\gamma}_{j+1}^A) \\ &= it \sum_{j=1}^{N-1} (\hat{b}_j + \hat{b}_j^\dagger)(i\hat{b}_j^\dagger - i\hat{b}_j) \\ &= t \sum_{j=1}^{N-1} (\hat{b}_j^2 + \hat{b}_j^\dagger \hat{b}_j - \hat{b}_j \hat{b}_j^\dagger - (\hat{b}_j^\dagger)^2) \\ &= 2t \sum_{j=1}^{N-1} \left(\hat{b}_j^\dagger \hat{b}_j - \tfrac{1}{2} \right). \end{aligned} \tag{A.8}$$

A.3 Expression for Majorana finite size energy splitting

Here we outline a derivation of Eq. (2.23). We follow the route used in Ref. [80], where a more thorough discussion is also found.

We start from the continuous form of the Bogoliubov-de Gennes Hamiltonian in momentum space. We focus on the $a \ll 1$ regime, so that $\sin(ka) \approx ka$ and $\cos(ka) \approx 1-(ka)^2/2$, and from it we transition to the position representation by making the transformation $k \to -i\partial_x$, which yields

$$H_{BdG}(x) = (2t - ta^2\partial_x^2 - \mu)\tau_z + 2a\Delta(i\partial_x)\tau_y. \tag{A.9}$$

We then assume that the spatial and spinor degrees of freedom are decoupled in the general solution, so that we can write it as $\phi(x) = \tilde{\phi}(x)(\tilde{u}, \tilde{v})^T$. Moreover, we assume the particular solutions have the form $\tilde{\phi}(x) \propto e^{i\lambda x}$, where λ is a complex constant. By inserting this guess into the eigenvalue equation we get

$$E^2 - (ta^2\lambda^2 + 2t - \mu)^2 - 4a^2\Delta^2\lambda^2 = 0, \quad \tilde{v} = i\frac{ta^2\lambda^2 + 2t - \mu - E}{2a\Delta\lambda}\tilde{u}. \tag{A.10}$$

For short-hand notation, we shall now conveniently hide some terms by defining the variables $\tilde{\mu} = \mu - 2t$ and $\tilde{\Delta} = 2\Delta/\sqrt{t}$. It turns out that this pair of equations yields low-energy solutions only when both the real and imaginary parts of $\lambda = k + iq$ are finite [80]. One of the possible values they can have is

$$k = \frac{1}{a\sqrt{2t}}(\sqrt{\tilde{\mu}^2 - E^2} + \tilde{\mu} - \tilde{\Delta}^2/2)^{\frac{1}{2}}, \quad q = \frac{1}{a\sqrt{2t}}(\sqrt{\tilde{\mu}^2 - E^2} - \tilde{\mu} + \tilde{\Delta}^2/2)^{\frac{1}{2}}. \tag{A.11}$$

Since the characteristic polynomial has real coefficients and only even power terms, if λ is a solution of it, then $-\lambda$, λ^* and $-\lambda^*$ are solutions as well. Also, note that k and q defined as above are not real for some ranges of parameters, such as $\tilde{\mu} < 0$. It is assumed that $\tilde{\mu}$ is positive and greater than $|E|$. In the following calculations we are going to assume we are outside those ranges. The general solution can then be expressed as a linear combination of the particular solutions

$$\phi_1(x) = e^{i\lambda x}\begin{pmatrix} 1 \\ -q\alpha + ik\beta \end{pmatrix}\tilde{u}, \quad \phi_2(x) = e^{-i\lambda x}\begin{pmatrix} 1 \\ q\alpha - ik\beta \end{pmatrix}\tilde{u}, \tag{A.12}$$

together with $\phi_3(x) = \phi_1^*(x)$ and $\phi_4(x) = \phi_2^*(x)$, and where

$$\alpha = \frac{1}{\tilde{\Delta}}\left(1 + \sqrt{\frac{\tilde{\mu} + E}{\tilde{\mu} - E}}\right), \quad \beta = \frac{1}{\tilde{\Delta}}\left(1 - \sqrt{\frac{\tilde{\mu} + E}{\tilde{\mu} - E}}\right). \tag{A.13}$$

We then construct a matrix

$$\mathcal{A} = \begin{pmatrix} [\phi_1(0)]_1 & [\phi_2(0)]_1 & [\phi_3(0)]_1 & [\phi_4(0)]_1 \\ [\phi_1(0)]_2 & [\phi_2(0)]_2 & [\phi_3(0)]_2 & [\phi_4(0)]_2 \\ [\phi_1(L)]_1 & [\phi_2(L)]_1 & [\phi_3(L)]_1 & [\phi_4(L)]_1 \\ [\phi_1(L)]_2 & [\phi_2(L)]_2 & [\phi_3(L)]_2 & [\phi_4(L)]_2 \end{pmatrix} \tag{A.14}$$

so that, by also defining $X = (c_1, c_2, c_3, c_4)^T$ and enforcing the boundary conditions $\phi(0) = \phi(L) = (0,0)^T$, we arrive at the eigenvalue equation

$$\mathcal{A}X = 0. \tag{A.15}$$

In order for $\mathcal{A}$ to have zero as an eigenvalue, we must have that $\det(\mathcal{A}) = 0$. After some tedious but straightforward calculations, we find that

$$\det(\mathcal{A}) = 8\left[(q\alpha\sin(kL))^2 + (k\beta\sinh(qL))^2\right]|\tilde{u}|^4. \tag{A.16}$$

Since $k, q, \alpha, |\tilde{u}| > 0$, this leads to the transcendental equation

$$q\alpha|\sin(kL)| = k|\beta|\sinh(qL). \tag{A.17}$$

Since we are interested only in the low-energy spectrum we can expand the variables k and q in terms of $E/\mu \ll 1$. It turns out the first order terms are zero, so that we can approximate $k \approx k_0$ and $q \approx q_0$, where

$$k_0 = \frac{1}{a\sqrt{2t}}\sqrt{\tilde{\mu} - \tilde{\Delta}^2/4}, \quad q_0 = \frac{\tilde{\Delta}}{2(a\sqrt{2t})} \tag{A.18}$$

We also expand the expressions for α and β such that

$$|\beta| \approx \frac{E}{2\tilde{\mu}}|\alpha|, \tag{A.19}$$

and by plugging this in our transcendental equation we finally get

$$\begin{aligned} E &\approx \frac{2\tilde{\mu}q_0}{k_0}\frac{|\sin(k_0L)|}{\sinh(q_0L)} \\ &\approx \frac{4\tilde{\mu}q_0}{k_0}e^{-q_0L}|\sin(k_0L)| + \mathcal{O}(e^{-3q_0L}), \end{aligned} \tag{A.20}$$

where we have used the approximation $\sinh(x)^{-1} \approx 2e^{-x} + \mathcal{O}(e^{-3x})$ for $x \gg 1$.

Appendix B

A very brief introduction to the Bogoliubov-De Gennes formalism.

B.1 Bogoliubov-De Gennes formalism

A superconducting system can be described by a Hamiltonian with a quadratic part and a quartic part [81]. The latter can be turned into a quadratic term through a mean-field approximation, resulting in couplings that do not preserve fermion number, but preserve fermion parity. These terms are products of two creation or two annihilation operators. In real-space basis, the system Hamiltonian is then

$$\mathcal{H} = \int d\mathbf{r} \left[\sum_{\sigma,\sigma'} H_0^{\sigma,\sigma'}(\mathbf{r}) \hat{c}^\dagger_{\sigma\mathbf{r}} \hat{c}_{\sigma'\mathbf{r}} + (\Delta(\mathbf{r}) \hat{c}^\dagger_{\uparrow\mathbf{r}} \hat{c}^\dagger_{\downarrow\mathbf{r}} + \text{H.c.}) \right]. \tag{B.1}$$

The so-called Bogoliubov-De Gennes formalism consists in defining a convenient spinor of fermions [23]

$$\hat{\mathbf{\Psi}}^T(\mathbf{r}) = \left(\hat{c}_{\uparrow\mathbf{r}}, \quad \hat{c}_{\downarrow\mathbf{r}}, \quad \hat{c}^\dagger_{\uparrow\mathbf{r}}, \quad \hat{c}^\dagger_{\downarrow\mathbf{r}} \right), \tag{B.2}$$

and a convenient matrix

$$H_{BdG} = \begin{pmatrix} H_0(\mathbf{r}) & \Delta(\mathbf{r}) \\ \Delta^*(\mathbf{r}) & -H_0^*(\mathbf{r}) \end{pmatrix} \tag{B.3}$$

such that Eq. (B.1) can be rewritten as

$$\mathcal{H} = \frac{1}{2} \int d\mathbf{r} \ \hat{\mathbf{\Psi}}^\dagger(\mathbf{r}) H_{BdG}(\mathbf{r}) \hat{\mathbf{\Psi}}(\mathbf{r}). \tag{B.4}$$

By doing this, we reduce the problem of diagonalizing a system in Fock space to diagonalizing a single-particle Hamiltonian. One can also at any point change the description to the basis of momentum, using the appropriate spinor basis as well. The BdG formalism is very useful in the study of superconducting systems. In this work we use it to describe a 1D semiconductor with proximitized superconductivity where *p-wave* superconductivity and Majorana Bound States can emerge.

Bibliography

[1] Chetan Nayak, Steven H. Simon, Ady Stern, Michael Freedman, and Sankar Das Sarma. Non-abelian anyons and topological quantum computation. *Reviews of Modern Physics*, 80(3):1083–1159, 2008.

[2] Yuval Oreg, Gil Refael, and Felix von Oppen. Helical Liquids and Majorana Bound States in Quantum Wires. *Phys. Rev. Lett.*, 105:177002, 2010.

[3] Roman M. Lutchyn, Jay D. Sau, and S. Das Sarma. Majorana Fermions and a Topological Phase Transition in Semiconductor-Superconductor Heterostructures. *Phys. Rev. Lett.*, 105:077001, 2010.

[4] Lucas Baldo Mesa Casa. Majorana bound states in Rashba nanowire junctions, 2020.

[5] Bose. Plancks Gesetz und Lichtquantenhypothese. *Zeitschrift für Physik*, 26(1):178–181, Dec 1924.

[6] Albert Einstein. Quantentheorie des einatomigen idealen Gases. *SB Preuss. Akad. Wiss. phys.-math. Klasse*, 1924.

[7] Albert Einstein. Quantentheorie des einatomigen idealen Gases. Zweite Abhandlung. *SB Preuss. Akad. Wiss. phys.-math. Klasse*, 1925.

[8] E. FERMI. Sulla quantizzazione del gas perfetto monoatomico. *Rendiconti Lincei*, 145, 1926.

[9] Paul A. M. Dirac. On the Theory of quantum mechanics. *Proc. Roy. Soc. Lond. A*, 112:661–677, 1926.

[10] Yingkai Liu. https://yk-liu.github.io/2019/Introduction-to-QC-and-TQC-Anyon-Model/.

[11] J. M. Leinaas and J. Myrheim. On the theory of identical particles. *Il Nuovo Cimento B (1971-1996)*, 37(1):1–23, Jan 1977.

[12] Frank Wilczek. Magnetic flux, angular momentum, and statistics. *Phys. Rev. Lett.*, 48:1144–1146, Apr 1982.

[13] G. A. Goldin, R. Menikoff, and D. H. Sharp. Representations of a local current algebra in nonsimply connected space and the Aharonov–Bohm effect. *Journal of Mathematical Physics*, 22(8):1664–1668, 1981.

[14] Yong-Shi Wu. General Theory for Quantum Statistics in Two Dimensions. *Phys. Rev. Lett.*, 52:2103–2106, 1984.

[15] Frank Wilczek. *Fractional statistics and anyon superconductivity.* World Scientific, Singapore, 1990.

[16] J. Frohlich, F. Gabbiani, and P.-A. Marchetti. *Braid Statistics in Three-Dimensional Local Quantum Theory*. Springer, Boston, MA, 1989.

[17] Sumathi Rao. Introduction to abelian and non-abelian anyons, 2016, [arxiv:1610. 09260].

[18] R. B. Laughlin. Anomalous Quantum Hall Effect: An Incompressible Quantum Fluid with Fractionally Charged Excitations. *Phys. Rev. Lett.*, 50:1395–1398, May 1983.

[19] Gregory Moore and Nicholas Read. Nonabelions in the fractional quantum hall effect. *Nuclear Physics B*, 360(2):362 – 396, 1991.

[20] Ady Stern. Anyons and the quantum Hall effect — A pedagogical review. *Annals of Physics*, 323(1):204–249, Jan 2008.

[21] Jiho Noh, Thomas Schuster, Thomas Iadecola, Sheng Huang, Mohan Wang, Kevin P. Chen, Claudio Chamon, and Mikael C. Rechtsman. Braiding photonic topological zero modes. *Nature Physics*, 16(9):989–993, 2020.

[22] Sankar Das Sarma, Michael Freedman, and Chetan Nayak. Majorana zero modes and topological quantum computation. *npj Quantum Information*, 1(1):15001, Oct 2015.

[23] Ramón Aguado. Majorana quasiparticles in condensed matter. *Nuovo Cimento*, 40:523–593, 2017.

[24] Paul A.M. Dirac. The quantum theory of the electron. *Proc. Roy. Soc. Lond. A*, 117:610–624, 1928.

[25] E. Majorana. Symmetrical theory of the electron and the positron. *Nuovo Cimento*, 5:171–184, 1937.

[26] A Yu Kitaev. Unpaired majorana fermions in quantum wires. *Physics-Uspekhi*, 44:131–136, 2001.

[27] Jesus David Cifuentes Pardo. *Acoplamento Kondo-Majorana em pontos quânticos duplos*. PhD thesis, Instituto de Física, Universidade de São Paulo, 2019. Master's Dissertation.

[28] Nicholas Sedlmayr, Vardan Kaladzhyan, Clément Dutreix, and Cristina Bena. Bulk boundary correspondence and the existence of Majorana bound states on the edges of 2D topological superconductors. *Physical Review B*, 96(18), 2017.

[29] Shinsei Ryu and Yasuhiro Hatsugai. Topological Origin of Zero-Energy Edge States in Particle-Hole Symmetric Systems. *Phys. Rev. Lett.*, 89:077002, Jul 2002.

[30] Topology in condensed matter. topocondmat.org/w2_majorana. Online course; accessed April-2021.

[31] Jason Alicea, Yuval Oreg, Gil Refael, Felix von Oppen, and Matthew P. A. Fisher. Non-abelian statistics and topological quantum information processing in 1d wire networks. *Nature Physics*, 7(5):412–417, 2011.

[32] B van Heck, A R Akhmerov, F Hassler, M Burrello, and C W J Beenakker. Coulomb-assisted braiding of Majorana fermions in a Josephson junction array. *New Journal of Physics*, 14(3):035019, 2012.

[33] Marcel Franz. Majorana's wires. *Nature Nanotechnology*, 8(3):149–152, 2013.

[34] Jorge Cayao. *Hybrid superconductor-semiconductor nanowire junctions as useful platforms to study Majorana bound states*. PhD thesis, Universidad Autónoma de Madrid, 2017. [arXiv:1703.07630].

[35] S. Vaitiekenas, G. W. Winkler, B. van Heck, T. Karzig, M.-T. Deng, K. Flensberg, L. I. Glazman, C. Nayak, P. Krogstrup, R. M. Lutchyn, and C. M. Marcus. Flux-induced topological superconductivity in full-shell nanowires. *Science*, 367(6485), 2020.

[36] Bernhard Mandl, Julian Stangl, Thomas Mårtensson, Anders Mikkelsen, Jessica Eriksson, Lisa S. Karlsson, Günther Bauer, Lars Samuelson, and Werner Seifert. Au-Free Epitaxial Growth of InAs Nanowires. *Nano Letters*, 6(8):1817–1821, 2006.

[37] R. Holm and W. Meissner. Messungen mit Hilfe von flüssigem Helium. XIII. *Zeitschrift für Physik*, 74(11):715–735, 1932.

[38] Hans Meissner. Superconductivity of Contacts with Interposed Barriers. *Phys. Rev.*, 117:672–680, 1960.

[39] Tudor D. Stanescu and Sankar Das Sarma. Proximity-induced low-energy renormalization in hybrid semiconductor-superconductor Majorana structures. *Phys. Rev. B*, 96:014510, 2017.

[40] A. P. Higginbotham, S. M. Albrecht, G. Kiršanskas, W. Chang, F. Kuemmeth, P. Krogstrup, T. S. Jespersen, J. Nygård, K. Flensberg, and C. M. Marcus. Parity lifetime of bound states in a proximitized semiconductor nanowire. *Nature Physics*, 11(12):1017–1021, 2015.

[41] Christian Jünger, Andreas Baumgartner, Raphaëlle Delagrange, Denis Chevallier, Sebastian Lehmann, Malin Nilsson, Kimberly A. Dick, Claes Thelander, and Christian Schönenberger. Spectroscopy of the superconducting proximity effect in nanowires using integrated quantum dots. *Communications Physics*, 2(1):76, 2019.

[42] Elsa Prada, Pablo San-Jose, and Ramón Aguado. Transport spectroscopy of NS nanowire junctions with Majorana fermions. *Phys. Rev. B*, 86:180503, 2012.

[43] VL Ginzburg. On the destruction and the onset of superconductivity in a magnetic field. *Soviet Phys. JETP*, 34:78–87, 1958.

[44] Hai-Feng Lü, Zhen Guo, Sha-Sha Ke, Yong Guo, and Huai-Wu Zhang. Shot noise as a measure of the lifetime and energy splitting of Majorana bound states. *Journal of Applied Physics*, 117(16):164312, 2015.

[45] Bin Li, Ji-Bang Fu, Guang-Yao Huang, and Ming-Tang Deng. Transport experiments in semiconductor-superconductor hybrid Majorana devices, 2020, 2009.10985.

[46] V. Mourik, K. Zuo, S. M. Frolov, S. R. Plissard, E. P. A. M. Bakkers, and L. P. Kouwenhoven. Signatures of Majorana Fermions in Hybrid Superconductor-Semiconductor Nanowire Devices. *Science*, 336(6084):1003–1007, 2012.

[47] Hao Zhang, Chun-Xiao Liu, Sasa Gazibegovic, Di Xu, John A. Logan, Guanzhong Wang, Nick van Loo, Jouri D. S. Bommer, Michiel W. A. de Moor, Diana Car, Roy L. M. Op het Veld, Petrus J. van Veldhoven, Sebastian Koelling, Marcel A. Verheijen, Mihir Pendharkar, Daniel J. Pennachio, Borzoyeh Shojaei, Joon Sue Lee, Chris J. Palmstrøm, Erik P. A. M. Bakkers, S. Das Sarma, and Leo P. Kouwenhoven. Quantized majorana conductance. *Nature*, 556(7699):74–79, 2018.

[48] Hao Zhang, Michiel W. A. de Moor, Jouri D. S. Bommer, Di Xu, Guanzhong Wang, Nick van Loo, Chun-Xiao Liu, Sasa Gazibegovic, John A. Logan, Diana Car, Roy L. M. Op het Veld, Petrus J. van Veldhoven, Sebastian Koelling, Marcel A. Verheijen, Mihir Pendharkar, Daniel J. Pennachio, Borzoyeh Shojaei, Joon Sue Lee, Chris J. Palmstrøm, Erik P. A. M.

Bakkers, S. Das Sarma, and Leo P. Kouwenhoven. Large zero-bias peaks in InSb-Al hybrid semiconductor-superconductor nanowire devices, 2021, 2101.11456.

[49] Stevan Nadj-Perge, Ilya K. Drozdov, Jian Li, Hua Chen, Sangjun Jeon, Jungpil Seo, Allan H. MacDonald, B. Andrei Bernevig, and Ali Yazdani. Observation of Majorana fermions in ferromagnetic atomic chains on a superconductor. *Science*, 346(6209):602–607, 2014.

[50] M. T. Deng, S. Vaitiekenas, E. B. Hansen, J. Danon, M. Leijnse, K. Flensberg, J. Nygård, P. Krogstrup, and C. M. Marcus. Majorana bound state in a coupled quantum-dot hybrid-nanowire system. *Science*, 354(6319):1557–1562, 2016.

[51] L. Tosi, C. Metzger, M. F. Goffman, C. Urbina, H. Pothier, Sunghun Park, A. Levy Yeyati, J. Nygård, and P. Krogstrup. Spin-Orbit Splitting of Andreev States Revealed by Microwave Spectroscopy. *Phys. Rev. X*, 9:011010, 2019.

[52] J. Tiira, E. Strambini, M. Amado, S. Roddaro, P. San-Jose, R. Aguado, F. S. Bergeret, D. Ercolani, L. Sorba, and F. Giazotto. Magnetically-driven colossal supercurrent enhancement in InAs nanowire Josephson junctions. *Nature Communications*, 8(1):14984, 2017.

[53] Kun Zuo, Vincent Mourik, Daniel B. Szombati, Bas Nijholt, David J. van Woerkom, Attila Geresdi, Jun Chen, Viacheslav P. Ostroukh, Anton R. Akhmerov, Sebastién R. Plissard, Diana Car, Erik P. A. M. Bakkers, Dmitry I. Pikulin, Leo P. Kouwenhoven, and Sergey M. Frolov. Supercurrent Interference in Few-Mode Nanowire Josephson Junctions. *Phys. Rev. Lett.*, 119:187704, 2017.

[54] M. Kjaergaard, H. J. Suominen, M. P. Nowak, A. R. Akhmerov, J. Shabani, C. J. Palmstrøm, F. Nichele, and C. M. Marcus. Transparent Semiconductor-Superconductor Interface and Induced Gap in an Epitaxial Heterostructure Josephson Junction. *Phys. Rev. Applied*, 7:034029, 2017.

[55] F. Nichele, E. Portolés, A. Fornieri, A. M. Whiticar, A. C. C. Drachmann, S. Gronin, T. Wang, G. C. Gardner, C. Thomas, A. T. Hatke, M. J. Manfra, and C. M. Marcus. Relating Andreev Bound States and Supercurrents in Hybrid Josephson Junctions. *Phys. Rev. Lett.*, 124:226801, 2020.

[56] D. Razmadze, E. C. T. O'Farrell, P. Krogstrup, and C. M. Marcus. Quantum Dot Parity Effects in Trivial and Topological Josephson Junctions. *Phys. Rev. Lett.*, 125:116803, 2020.

[57] Anna Grivnin, Ella Bor, Moty Heiblum, Yuval Oreg, and Hadas Shtrikman. Concomitant opening of a bulk-gap with an emerging possible Majorana zero mode. *Nature Communications*, 10(1):1940, 2019.

[58] G. L. R. Anselmetti, E. A. Martinez, G. C. Ménard, D. Puglia, F. K. Malinowski, J. S. Lee, S. Choi, M. Pendharkar, C. J. Palmstrøm, C. M. Marcus, L. Casparis, and A. P. Higginbotham. End-to-end correlated subgap states in hybrid nanowires. *Phys. Rev. B*, 100:205412, 2019.

[59] Torsten Karzig, Christina Knapp, Roman M. Lutchyn, Parsa Bonderson, Matthew B. Hastings, Chetan Nayak, Jason Alicea, Karsten Flensberg, Stephan Plugge, Yuval Oreg, and et al. Scalable designs for quasiparticle-poisoning-protected topological quantum computation with Majorana zero modes. *Physical Review B*, 95(23), 2017.

[60] B. Misra and E. C. G. Sudarshan. The Zeno's paradox in quantum theory. *Journal of Mathematical Physics*, 18(4):756–763, 1977, https://doi.org/10.1063/1.523304.

[61] Sergey Bravyi and Alexei Kitaev. Universal quantum computation with ideal Clifford gates and noisy ancillas. *Physical Review A*, 71(2), 2005.

[62] A.F. Andreev. The Thermal Conductivity of the Intermediate State in Superconductors. *JETP*, 19:1228, 1964.

[63] C. W. J. Beenakker. Three "Universal" Mesoscopic Josephson Effects. In *Transport Phenomena in Mesoscopic Systems*, pages 235–253, Berlin, Heidelberg, 1992.

[64] A.F. Andreev. Electron Spectrum of the Intermediate State of Superconductors. *JETP*, 22:455–458, 1966.

[65] J. A. Sauls. Andreev bound states and their signatures. *Philosophical Transactions of the Royal Society A: Mathematical, Physical and Engineering Sciences*, 376(2125):20180140, 2018.

[66] B.D. Josephson. The discovery of tunnelling supercurrents. *Rev. Mod. Phys.*, 46:251–254, 1974.

[67] Dong E. Liu and Harold U. Baranger. Detecting a Majorana-fermion zero mode using a quantum dot. *Physical Review B*, 84(20), 2011.

[68] S. Das Sarma, Jay D. Sau, and Tudor D. Stanescu. Splitting of the zero-bias conductance peak as smoking gun evidence for the existence of the Majorana mode in a superconductor-semiconductor nanowire. *Physical Review B*, 86, 2012.

[69] Diego Rainis and Daniel Loss. Conductance behavior in nanowires with spin-orbit interaction: A numerical study. *Physical Review B*, 90(23), Dec 2014.

[70] E. Vernek, P. H. Penteado, A. C. Seridonio, and J. C. Egues. Subtle leakage of a Majorana mode into a quantum dot. *Phys. Rev. B*, 89:165314, 2014.

[71] Silas Hoffman, Denis Chevallier, Daniel Loss, and Jelena Klinovaja. Spin-dependent coupling between quantum dots and topological quantum wires. *Phys. Rev. B*, 96:045440, 2017.

[72] Diego Rainis, Arijit Saha, Jelena Klinovaja, Luka Trifunovic, and Daniel Loss. Transport Signatures of Fractional Fermions in Rashba Nanowires. *Physical Review Letters*, 112(19), 2014.

[73] Pablo San-Jose, Elsa Prada, and Ramón Aguado. ac Josephson Effect in Finite-Length Nanowire Junctions with Majorana Modes. *Phys. Rev. Lett.*, 108:257001, 2012.

[74] Jorge Cayao, Annica M Black-Schaffer, Elsa Prada, and Ramón Aguado. Andreev spectrum and supercurrents in nanowire-based SNS junctions containing Majorana bound states. *Beilstein Journal of Nanotechnology*, 9:1339–1357, 2018.

[75] Roman-Pascal Riwar, Manuel Houzet, Julia S. Meyer, and Yuli V. Nazarov. Multi-terminal Josephson junctions as topological matter. *Nature Communications*, 7(1), 2016.

[76] Natalia Pankratova, Hanho Lee, Roman Kuzmin, Kaushini Wickramasinghe, William Mayer, Joseph Yuan, Maxim G. Vavilov, Javad Shabani, and Vladimir E. Manucharyan. Multiterminal Josephson Effect. *Physical Review X*, 10(3), 2020.

[77] Tomohiro Yokoyama and Yuli V. Nazarov. Singularities in the Andreev spectrum of a multiterminal Josephson junction. *Physical Review B*, 92(15), 2015.

[78] Manuel Houzet and Julia S. Meyer. Majorana-Weyl crossings in topological multiterminal junctions. *Physical Review B*, 100(1), 2019.

[79] Panagiotis Kotetes, Maria Teresa Mercaldo, and Mario Cuoco. Synthetic Weyl Points and Chiral Anomaly in Majorana Devices with Nonstandard Andreev-Bound-State Spectra. *Physical Review Letters*, 123(12), 2019.

[80] Chuanchang Zeng, Christopher Moore, Apparao M. Rao, Tudor D. Stanescu, and Sumanta Tewari. Analytical solution of the finite-length Kitaev chain coupled to a quantum dot. *Phys. Rev. B*, 99:094523, 2019.

[81] J. Bardeen, L. N. Cooper, and J. R. Schrieffer. Theory of Superconductivity. *Phys. Rev.*, 108:1175–1204, 1957.